Università degli Studi di Ferrara

DOCTORAL COURSE IN PHYSICS

CYCLE XXXII

COORDINATOR Prof. Luppi Eleonora

Exploring lower atmosphere and topsoil with gamma-ray spectroscopy

Scientific/Disciplinary Sector (SDS) FIS/07

Candidate
Dott. Bottardi Carlo

Supervisor
Prof. Mantovani Fabio

Year 2016/2019

Overview

Radioactivity is a physical phenomenon occurring spontaneously when an unstable nucleus of an atom transforms itself, often through a radioactive decay, by reaching a new condition of stability with the emission of one or more particles. This natural phenomenon can be found everywhere around us: we receive radiation coming from the far-away Universe, from the atmosphere, from the rain, from soils and rocks and even our body is radioactive, implying that radioactivity has partially influenced life evolution on Earth. Recently the improvement of our comprehension of this phenomenon made possible handling, managing and producing radioactivity, opening the way to significant progresses in many disciplines such as medicine, with its exploitation in radiology and radiation oncology, and nuclear engineering for the development of nuclear power plants and, regrettably, of nuclear weapons.

The use of radioactive sources has found useful applications in our daily lives. The high penetration power of gamma radiation is perfect to investigate what is hidden under the surface of the most various bodies. This ability can be exploited for many industrial processes such gauging the thickness of metals, films, paper and plastic or determining the moisture of the soil. The same penetration power is useful for investigate what is hidden under the surface of works of art and ancient artefacts for instance discovering the deeper layers of a painting. Comparing the abundances of an appropriate radionuclide and its decay product in a rock or in an ancient object is possible to determine its age, for instance for items up to about 60.000 years old, such as Neanderthals and ice age animals, the ratio ^{14}C to ^{12}C is exploited while the age of the Earth has been determined to be 4.6 billion using $^{238}U/^{206}Pb$ dating.

The radioactivity coming from the space originates from cosmic rays particles, with energies extending up to few 10^{20} eV, produced outside the Solar System and constituted by a nucleonic component (98%) and electrons (2%). The nucleonic component is primarily made up by protons (∼85% of the flux) and alpha particles (∼12%), with a remaining fraction comprising heavier nuclei. These primary cosmic rays interact with the atoms present in the atmosphere producing air showers, i.e. extensive (many kilometres wide) cascade of ionized particles and electromagnetic radiation. Indeed, the unstable hadrons produced in these collisions decay in the air speedily into other particles and electromagnetic radiation, producing a secondary radiation that includes photons, muons, protons, antiprotons, alpha particles, pions, electrons, positrons, neutrons and neutrinos.

Terrestrial radioactivity is mainly due to three radioisotopes: ^{238}U ($4.5 \cdot 10^9$ years half-life), ^{232}Th ($1.4 \cdot 10^{10}$ years half-life) and ^{40}K ($1.3 \cdot 10^9$ years half-life). These radionuclides were produced in the supernovae explosion preceding the formation of our planet and a significant fraction of them have survived up to now thanks to the long half-life, comparable with the Earth's age.

^{40}K can undergo beta decay to ^{40}Ca (89.3% branching fraction) or electron capture to $^{40}Ar^*$ (10.3% branching fraction), with the consequent emission of a monoenergetic gamma radiation with 1.46 MeV energy. ^{238}U and ^{232}Th give rise to radioactive decay chains respectively ending with the stable isotopes ^{206}Pb and ^{208}Pb, which involve alpha and beta decays accompanied by numerous gamma emissions extending up to 2.61 MeV energy. Important intermediate products of ^{238}U and ^{232}Th decay chains are ^{222}Rn (3.8 days half-life) and ^{220}Rn (55.6 seconds half-life), respectively. Being the only gaseous elements of the respective decay chains, they can exhale from the Earth's crust to the atmosphere, giving birth to an additional contribution to environmental radioactivity. In particular, ^{222}Rn is a noble gas with poor chemical reactivity. This characteristic together with its 3.8 days half-life permits the diffusion in the atmosphere and make it perfect as tracer of air transport processes.

A gamma decay occurs when a nucleus emits a photon in order to reach a more stable configuration (i.e. a lower energy level), which energy can range from tens of keV to few MeV.

Among the electromagnetic waves, the most energetic ones are called gammas and have higher penetration power respect to other common radiations as alpha and beta, characteristics that make gammas ideal to perform proximal and remote sensing and investigating cosmic, atmospheric and terrestrial sources of radioactivity.

This work presents airborne and in situ gamma-ray spectroscopy measurement campaigns performed with respectively with a 16L and a 1L thallium-doped sodium iodide scintillator (NaI(Tl)), one of the most common and efficient inorganic scintillators. When a gamma photon interacts with the detector material it deposits energy inside the scintillator which in turn converts this energy into visible light. The latter is in turn converted and amplified by a photomultiplier tube into a measurable electric current, proportional to the primary energy deposition. A multichannel analyser finally allows for building a gamma energy spectrum, i.e. a histogram of the detected events classified according to their energy depositions. The most notable characteristics of an energy spectrum are the photopeaks: peaks formed by photons depositing all their energy inside the detector via photoelectric effect. Since each radionuclide has a different emission spectrum, it's possible to identifying the radioactive source from its energy spectrum.

Gamma-ray spectroscopy is a powerful and versatile tool which can be used for multiple scientific purposes, like landslide monitoring, peat thickness estimation, prediction models for trees' growth, radioelement distribution in weathered materials and precision agriculture.

The contents of this thesis are included in 6 publications, 5 already published and 1 submitted to a peer-reviewed scientific journal. Each of the three chapters of the thesis presents a different topic that is explored in detail.

Chapter 1 presents the AGRS offshore measurement campaign and data analysis performed for calibrating the 16L NaI(Tl) spectrometer for background radiation. Background radiation sources are: radioactivity inside the detector and aircraft materials, cosmic rays and atmospheric ^{222}Rn. The latter is a background source since estimates of the ^{238}U content via gamma spectroscopy measurements rely on the evaluation of the background subtracted count rates in the ^{214}Bi photopeak energy window and the component associated to the decay of atmospheric ^{214}Bi, coming from the decay of atmospheric ^{222}Rn, has to be removed.

Four calibration flights above the sea in the (77-3066) m height range were carried out. A specific χ^2 statistical analysis has been developed aimed at separately determining the background contribution in the ^{40}K, ^{214}Bi (from the ^{238}U chain) and ^{208}Tl (from the ^{232}Tl chain) photopeaks of interest. This task required an integration of the measured count rates in the [3-7] MeV energy window, the so called cosmic energy window, which allowed also for calibrating the AGRS detector for the cosmic effective dose to the human population. Secondarily the atmospheric ^{222}Rn background contribution is treated by applying to the experimental data a model that predicts the count rate in the ^{214}Bi photopeak as the result of a two-layers ^{222}Rn vertical distribution.

Chapter 2 presents the results of a 7-months proximal gamma-ray spectroscopy experiment performed by installing a 1L NaI(Tl) detector and a meteorological station in an agricultural test field, which allowed for continuously and simultaneously acquiring the environmental gamma activity and the rain amount time series. The observed rain-induced gamma activity enhancement is a phenomenon due to the attachment of the atmospheric ^{214}Pb and ^{214}Bi gamma emitters to aerosols, in turn attaching to raindrops falling to ground. I developed a model describing the temporal evolution of the ^{214}Pb gamma activity in correspondence with rainfalls which demonstrates the capability of gamma-ray spectroscopy to discriminate irrigated from precipitated water.

Chapter 3 discusses the results obtained during the above-mentioned proximal gamma-ray spectroscopy experiment in the field of precision agriculture. A 1L NaI(Tl) detector has been placed at a height of 2.25 m and measured the gamma signal coming from an area having a radius of about 25 m and from a depth of approximately 30 cm. Since water is much more effective in attenuating gamma rays with respect to minerals typically present in the soil, the goal was to analyse radiometric data for inferring the soil water content. By exploiting the inverse proportionality between soil moisture and the ^{40}K gamma signal and by accounting for a non-constant correction due to the presence of growing vegetation, soil water content was effectively estimated over the entire data-taking period with an average absolute discrepancy of about 2% with gravimetric validation measurements on soil samples.

Chapter 1

Studying cosmic radiation and radon in lower atmosphere with airborne gamma-ray spectroscopy

During my PhD course my research lead me to Airborne Gamma-Ray Spectroscopy (AGRS).

AGRS is widely considered as a powerful tool in measuring the concentration of natural and artificial radionuclides in topsoil of large areas. During the last few decades Airborne Gamma-Ray Spectroscopy has been demonstrated to be an extraordinarily useful method for environmental monitoring, mineral exploration and geological mapping (Appleton et al., 2011; Smethurst et al., 2017). Although far from being a novel technique, the frontiers of AGRS and its applications are continuously pushed forward thanks to advances in multichannel processing, statistical methods for spatial resolution enhancement and data analysis procedures (Beamish, 2016; de Figueiredo Iza et al., 2016; Minty and Brodie, 2016). The potentialities of the AGRS technique in the sector of homeland security have been widely explored in terms of feasibility of real-time identification of anthropogenic radionuclides on top of the natural background and of merging and comparing results from multi-regional AGRS campaigns performed in the framework of intercomparison exercises.

In the light of environmental contamination assessment, the detection of anthropogenic radionuclides emitting low energy gamma rays (e.g., ^{137}Cs and ^{131}I) together with the employment of new unmanned aerial vehicle (UAV) devices, characterized by different detection performances compared with standard acquisition systems, are reawakening the effort in estimating detectors efficiencies and minimum detectable activities (MDA) (Cao et al., 2015; Gong et al., 2014).

In order to address the AGRS new challenges, an adequate understanding and knowledge of the background spectral components is mandatory for processing airborne gamma-ray spectrometric data. Sources of background during an AGRS survey are air showers due to cosmic rays, the radionuclides included in the aircraft materials and the gamma emitting daughters of atmospheric ^{222}Rn. In this chapter are presented the results of about 5 hours AGRS survey over the sea dedicated to the measurements of the gamma radiation coming from these background sources in a wide range of elevations (77-3066 m).

In section 1.1 is presented a study dedicated to the measurement of the gamma radiation originating from the aircraft materials and cosmic rays (Baldoncini et al., 2018b). Section 1.2 presents a two-layer model describing the concentration of ^{222}Rn in the atmosphere (Baldoncini et al., 2017).

1.1 Airborne gamma-ray spectroscopy for modelling cosmic radiation and effective dose in the lower atmosphere

In this section we present the results of a ~5 hour airborne gamma-ray survey carried out over the Tyrrhenian sea in which the height range (77-3066) m has been investigated. Gamma-ray spectroscopy measurements have been performed by using the AGRS_16L detector, a module of four 4L NaI(Tl) crystals. The experimental setup was mounted on the Radgyro, a prototype aircraft designed for multisensorial acquisitions in the field of proximal remote sensing. By acquiring high-statistics spectra over the sea (i.e. in the absence of signals having geological origin) and by spanning a wide spectrum of altitudes it has been possible to split the measured count rate into a constant aircraft component and a cosmic component exponentially increasing with increasing height. At ground level the secondary cosmic radiation includes a ~15% of effective dose coming from gamma-rays. The monitoring of the count rate having pure cosmic origin in the >3 MeV energy region allowed to infer the background count rates in the ^{40}K, ^{214}Bi and ^{208}Tl photopeaks, which need to be subtracted in processing airborne gamma-ray data in order to estimate the potassium, uranium and thorium abundances in the ground. Moreover, I carried out a calibration procedure by implementing the CARI-6P and EXPACS dosimetry tools, according to which the annual cosmic effective dose to human population has been linearly related to the measured cosmic count rates.

1.1.1 Instruments and methods

Airborne gamma-ray surveys over the sea were carried out with the Radgyro (Figure 1.1), a prototype aircraft dedicated to multispectral airborne measurements. The Radgyro is an autogyro specifically designed to host a large network of sensors which are able to investigate simultaneously and independently the electromagnetic spectrum in a variety of spectral ranges, from thermal infrared (13000-7500 nm) to gamma radiation ($3 \cdot 10^{-3} - 4 \cdot 10^{-4}$ nm). The high autonomy and payload (3 hours for a 120 kg equipment weight), the modularity of the acquisition system, together with the possibility of time correlating the information coming from the different sensors, make the Radgyro a unique aircraft in the field of proximal remote sensing.

Figure 1.1. Picture of the Radgyro, the autogyro dedicated to multispectral airborne acquisitions, used for the AGRS surveys over the sea

During the surveys the Radgyro position is recorded every second by a GPS system composed of 2 u-blox EVK-6T antennas (Alberi et al., 2017). Gamma radiation is measured with the AGRS_16L system, a modular scintillation detector hosted in the central region of the aircraft hull and composed of four 10 cm × 10 cm × 40 cm NaI(Tl) crystals, for a total detection volume of 16L. Each detector has a 1 mm thick stainless steel shielding and is coupled with a PMT base which receives the voltage supply from a power unit shared among all the sensors mounted on the aircraft. The signals are acquired in list mode (event by event) by a CAEN DT5740 module, a 32 channel 12 bit 62.5 MS/s waveform digitizer.

AGRS raw data are acquired event by event separately for each of the four NaI(Tl) detectors: each list mode file contains the time stamp of a given energy deposition (in units of digitizer clock) together with the corresponding acquisition channel. The list mode files are cut offline for each detector in order to produce 1 second acquisition spectra which subsequently undergo an energy calibration procedure. The latter is performed by determining with a Gaussian fit the positions of the prominent ^{40}K and ^{208}Tl photopeaks in 600 seconds spectra acquired on the ground before the take off. A linear function is then fitted to the photopeaks' positions for estimating the energy corresponding to the first acquisition channel (keV) and the gain (keV/channel). Summing up the four calibrated spectra it is possible to obtain the gamma-ray 1 second spectrum acquired by the entire 16L detection volume, which has an energy end point of 7 MeV.

For what concerns the Radgyro positioning, each GPS antenna produces two separate files, one containing the temporal information in terms of PC and GPS acquisition times, the second is a binary file which is processed with the goGPS software (Herrera et al., 2016) for the extraction of the standard NMEA sentence. The mean 1 second position and altitude above sea level of the Radgyro is computed as the average of the coordinates obtained from the single GPS receivers. As both the radiometric and positioning data are acquired with the same PC, the computer time stamp is used for the synchronization of the different devices (Alberi et al., 2017).

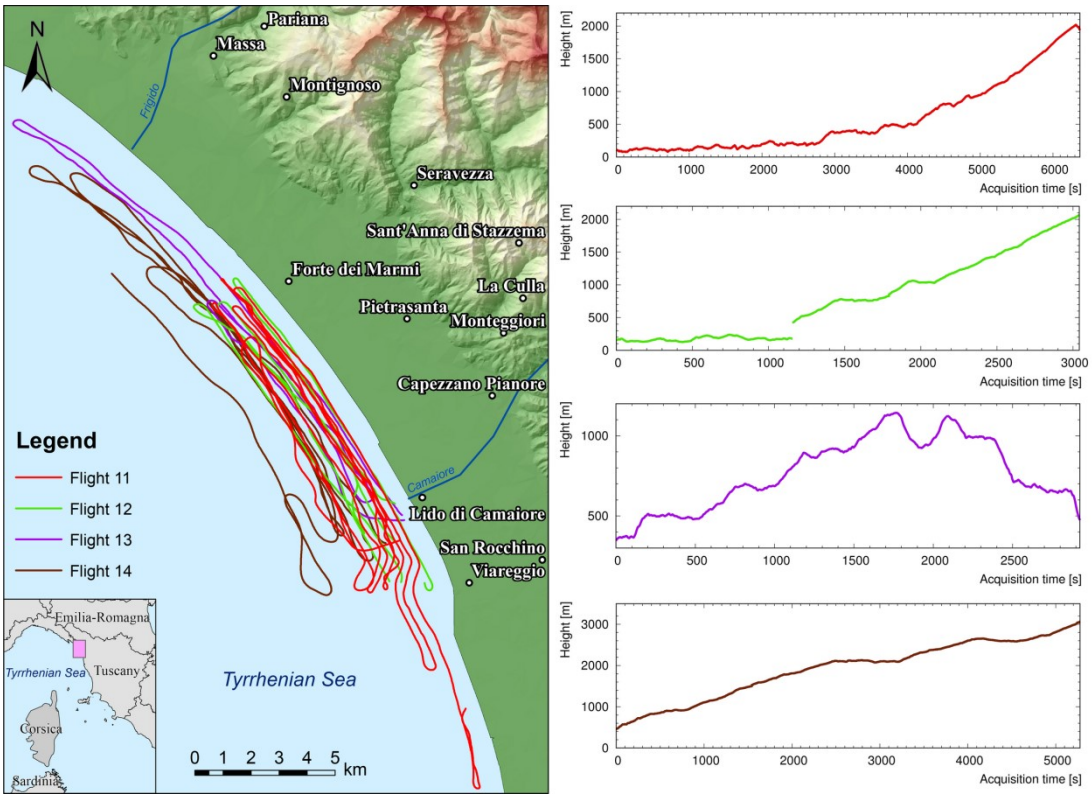

Figure 1.2. The left panel shows a map of the effective flight lines of the surveys over the sea performed near Viareggio (Tuscany, Italy). The acquisition tracks are the ones corresponding to data points acquired at a minimum distance from the coast of 300 m. The

four panels on the right show the altitude profiles for the different flights. On the x axis the effective acquisition time for each individual flight is reported (see Table 1.1).

Airborne gamma-ray background calibration surveys were performed in a series of 4 flights over the Tyrrhenian Sea close to Viareggio (Tuscany, Italy) with typical horizontal and vertical velocities of ~20 m/s and ~0.8 m/s, respectively. In order to avoid taking into account gamma-ray signals potentially spoiled by ground radiation, gamma-ray measurements acquired at a distance from the coast less than 300 m have been excluded from the analysis. In Figure 1.2 the effective paths of the different flights are shown, which correspond to a total acquisition time of 17612 seconds and an explored range of altitudes going from 77 m to 3066 m. In Table 1.1 a summary of the main parameters related to each of the 4 flights is shown.

According to the purpose of the experiment, the flight paths have been planned with the aim of investigating the entire reported range of heights with enough statistics for well constraining the analysis of the altitude dependent gamma-ray cosmic component. This strategy, together with the flight conditions and the non feasibility for the Radgyro to hover at a given elevation, allowed us to collect the elevation flight statistics shown in Figure 1.3.

Table 1.1. Summary of the main parameters for each of the 4 surveys over the sea. For each flight the ID, date, time, minimum and maximum altitude and acquisition time are reported, respectively. In the case of flights 11 and 14, 83 seconds and 30 seconds have been cut due to some radiofrequency interference between the PMT and the aircraft transponder. The long interruption of the data taking of flight 12 (2531 seconds) has been imposed by civil traffic of the Pisa airport.

Flight ID	Date	Time	z min [m]	z max [m]	Acquisition time [s]
11	30/03/2016	17:42:10 19:29:43	77	2019	6370
12	31/03/2016	18:13:55 19:46:47	126	2070	3041
13	05/04/2016	11:39:53 12:28:36	348	1144	2924
14	05/04/2016	16:37:16 18:05:43	461	3066	5377
Global			77	3066	17612

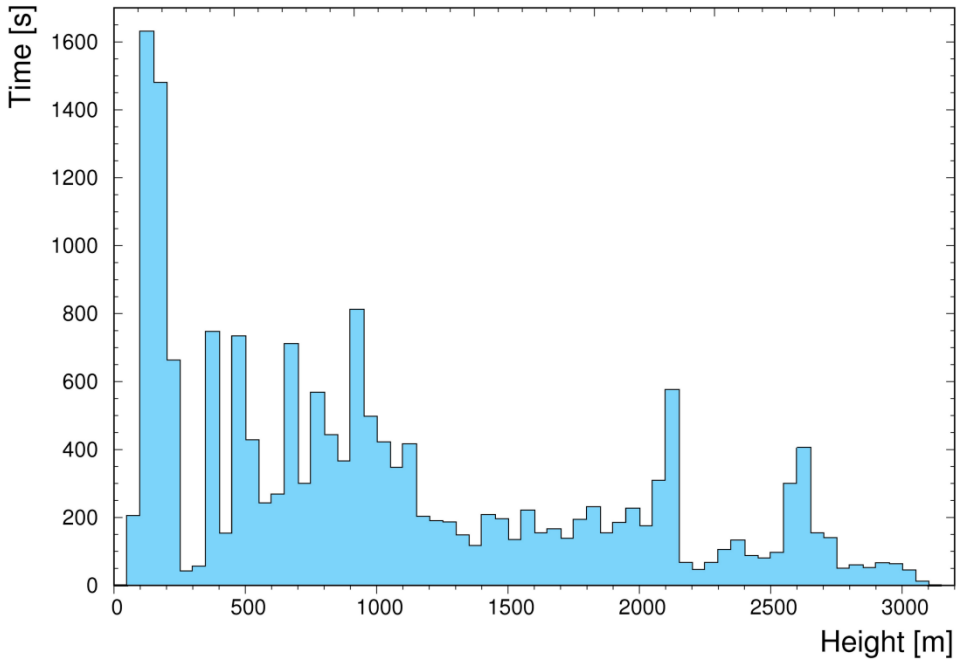

Figure 1.3. Histogram describing the effective overall temporal statistics: the data taking time at a given survey altitude is shown, with an altitude binning of 50 m.

1.1.2 Theoretical modelling and data analysis

Airborne gamma-ray spectroscopy measurements are affected by background radiation, which can be considered as radiation not originating from the Earth's surface and which has to be removed during data processing. The three major sources of background radiation are cosmic background, instrumental plus aircraft background and atmospheric radon (^{222}Rn).

The cosmic gamma background resulting from the interaction of cosmic secondary radiation interaction with the air, the aircraft and the detector materials is foreseen to monotonically increase with increasing altitude. Concerning the energy dependence, the cosmic-induced gamma-ray energy spectrum is expected to have a polynomial dependence with respect to gamma-ray energy (Sandness et al., 2009). The count rate (CR) energy dependence of the cosmic component is reconstructed according to a polynomial function having the following expression:

$$CR(E) = aE^b + c \tag{1.1}$$

where E is the gamma-energy in MeV and a, b and c are constants for a spectrum measured at a given altitude. The energy dependence of the CR has been estimated by fitting the measured spectrum with the above model function both in the 0.8-7 MeV energy range and in the 3-7 MeV energy range, called respectively the Full Energy Window (FEW) and the Cosmic Energy Window (CEW). A third fit has been performed using as input data points the measured CRs in the CEW, plus the three points corresponding to the estimated CRs due to cosmic radiation in the ^{40}K, ^{214}Bi and ^{208}Tl photopeak energy windows (see Table 1.3, which have been determined on the base of the linear regression parameters reported in Table 1.5.

In Table 1.2 the results of this analysis in two different ranges of altitudes is reported. In both cases radiometric data have been acquired above 2000 m, where the presence of atmospheric radon is negligible (see Section 1.1.3). Figure 1.4 shows an example of background airborne gamma-ray spectrum measured with the AGRS_16L together with the three curves resulting from the different fitting procedures. From this exercise it is possible to evince that the fitting of the measured spectrum is dependent on the energy range

chosen, as the spectral shape under reconstruction contains different pieces of information in the CEW and in the FEW. Using only the CEW for constraining the cosmic spectral shape from one side assures the pure cosmic nature of the counting statistics, but on the other side the sole reconstruction of the spectral high energy tail prevents a correct estimation of the curve slope in the low energy range as emphasized by the large uncertainties on the best fit parameters. By fitting in the FEW the steep behavior at low energies is reproduced: however in this case the measurement under reconstruction contains not only the cosmic contribution to the signal, but also the signal coming from the equipment radioactivity and in particular from the ^{40}K, ^{214}Bi and ^{208}Tl decay series. On the other hand, the idea behind the third fitting approach is to reinforce the fit performed by using the sole count rates in the CEW with the addition of three relatively well separated points corresponding to the cosmic CRs in the ^{40}K, ^{214}Bi and ^{208}Tl photopeak energy windows. Among the above mentioned three strategies this is the one providing the most reliable estimation of the cosmic spectral shape in the FEW.

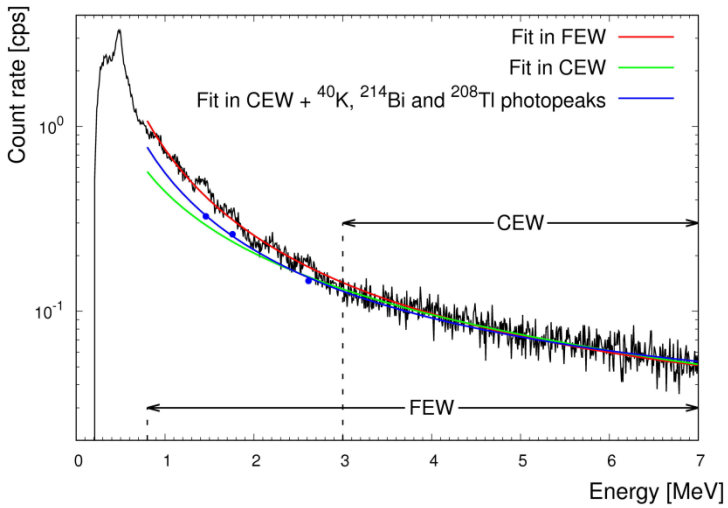

Figure 1.4. Gamma-ray spectrum composed of 870 1 second spectra acquired in the elevation range 2050-2150 m (black solid line). The red solid line shows the fitting curve obtained using as model function Eq. (1.1) and as energy fitting range the FEW, the green solid line shows the curve obtained by fitting the measured spectrum in the CEW. The blue points correspond to the CRs in the KEW, BEW and TEW associated with the cosmic induced background and obtained on the base of the linear relation having as parameters the ones reported in Table 1.5. The blue solid line is the result of the fit of the measured spectrum in the CEW and of the blue points.

Table 1.2. Fit parameters of the CR energy dependence modeled with Eq. (1.1) for two spectra measured at 2100 m and 2650 m for respectively 870 seconds and 550 seconds. For each measured spectrum the fit has been performed in the FEW, in the CEW and in the CEW plus the ^{40}K, ^{214}Bi and ^{208}Tl photopeaks.

z range [m]	Fit energy range	(a ± δa) [cps]	(b ± δb) [cps]	(c ± δc) [cps]
2050-2150	FEW	0.73 ± 0.10	-1.62 ± 0.40	0.02 ± 0.03
	CEW	0.44 ± 0.42	-1.11 ± 1.60	0.00 ± 1.40
	CEW + ^{40}K, ^{214}Bi and ^{208}Tl photopeaks	0.54 ± 0.04	-1.49 ± 0.05	0.02 ± 0.01
2600-2700	FEW	0.90 ± 0.11	-1.53 ± 0.33	0.02 ± 0.04
	CEW	0.62 ± 0.61	-1.14 ± 1.66	0.00 ± 1.87
	CEW + ^{40}K, ^{214}Bi and ^{208}Tl photopeaks	0.71 ± 0.05	-1.45 ± 0.03	0.02 ± 0.01

Table 1.3. Energy windows for natural and cosmic radiation used for the background calibration of the AGRS_16L system. The last two columns report for each energy window the measured CR for gamma-ray spectra acquired at the altitude range 2050-2150 m and 2600-2700 m, respectively.

Energy Window	Emission line [keV]	Energy range [keV]	Measured CR [cps] (2050-2150) m	Measured CR [cps] (2600-2700) m
KEW	1460	1370-1570	12.2	15.0
BEW	1765	1660-1860	8.7	11.1
TEW	2614	2410-2810	8.8	11.9
CEW	/	3000-7000	41.9	54.8

Instrumental and aircraft background correspond to the constant gamma signal generated by trace amounts of K, U and Th contained in the detector materials and ancillary equipment, together with the aircraft material itself. ^{222}Rn, the only gaseous daughter product of the ^{238}U decay chain, can escape from rocks and soils and, considering its 3.8 days half-life, can accumulate in the lower atmosphere. Its gamma-emitting daughter nuclei ^{214}Bi and ^{214}Pb can attach to airborne aerosols and dust particles, giving rise to the atmospheric radon background gamma signal. The determination of the K, U and Th ground concentrations during an airborne gamma-ray survey relies on the estimation of the background corrected CRs recorded in the ^{40}K, ^{214}Bi (eU) and ^{208}Tl (eTh) photopeak energy windows, called KEW, BEW and TEW, respectively (see Table 1.3).

Aircraft and cosmic background calibration flights are usually performed offshore for a typical altitudes range of (1500 - 3000) m above the ground level in order to avoid the contamination from terrestrial radiation and radon decay products (IAEA, 1991). In this scenario, as the instrumental background is supposed to be constant and the gamma cosmic background is expected to exponentially increase with increasing height, the measured CRs in the i'th energy window during a calibration flight over the sea is predicted to follow the subsequent equation:

$$N^i(z) = A^i e^{\mu^i z} + B^i \tag{1.2}$$

where n^i is the CR in the i'th energy window (with i = KEW, BEW, TEW and CEW) A^i, μ^i and B^i are constants (IAEA, 1991; Minty, 1997).

The CR in the natural radionuclides energy windows are expected to be linearly related to the count rate in the CEW, as stated in the following equation:

$$n^i = a^i + b^i n^{CEW} \tag{1.3}$$

where n^i is the CR in the i'th energy window (with i = KEW, BEW, TEW), a^i is the aircraft background CR in the i'th energy window, b^i is the cosmic stripping ratio (i.e. the cosmic background CR in the i'th energy window normalized to unit counts in the CEW) and n^{CEW} is the CR in the CEW. The parameter a^i is the expected CR for null cosmic CR and therefore represents the constant background component generated by the Radgyro and by the detectors materials. Determining these linear functions for the natural radionuclides energy windows allows to correct the CRs measured at a given height during regional AGRS surveys for the aircraft and height dependent cosmic ray backgrounds, provided the monitoring of the CR in the CEW.

Eq. (1.2), as well as Eq. (1.3), holds in the absence of any terrestrial and atmospheric radon radiation component. A potential radon contamination in any case would act on the CRs in the KEW and BEW but not on the CRs in the TEW and CEW as they are not affected by the lower energy gamma emissions of radon daughter nuclei. The presence of a radon background component in the measured CRs can be generally

identified as a breakdown of the linear relationship between the cosmic and the ^{214}Bi CRs at low elevations (Baldoncini et al., 2017). The estimated CRs in the energy windows of interest have been clustered according to an altitude binning of 15 m, which is conservative with respect to the estimated accuracy on the vertical position resulting from the combination of all the altimeters present on board of the Radgyro (Alberi et al., 2017). The CRs used as input for the background modeling are therefore estimated summing all the input CRs acquired in the same elevation bin and dividing by the number of 1 second spectra entering the summation.

The parameters of the exponential curves A^i, μ^i and B^i have been determined via the minimization of the χ^2 function:

$$\chi^2_{exp} = \sum_{j=1}^{nbin} \left[\frac{n_j^i - \left(A^i e^{\mu^i z} + B^i \right)}{\sigma_{n_j^i}} \right]^2 \tag{1.4}$$

where nbin is equal to the number of elevation bins entering the χ^2 minimization, n_j^i is the average CR obtained for the j'th elevation bin in the i'th energy window, z_j is the average elevation obtained for the j'th elevation bin and $\sigma_{n_j^i}$ is the 1 sigma uncertainty associated to the counting statistics, corresponding to the square root of the total counts recorded at z_j in the i'th energy window divided by the acquisition time at z_j.

The objective χ^2 function to be minimized for determining the linear curve parameters has instead to be built taking into account not only the statistical error associated to the quantity z_i but also the uncertainty on the "independent variable" n^{CEW}. Therefore, the adopted definition for the χ^2 function is:

$$\chi^2_{lin} = \sum_{j=1}^{nbin} \frac{\left[n_j^i - \left(a^i + b^i n_j^{CEW} \right) \right]^2}{\left(\sigma_{n_j^i} \right)^2 + \left(b^i \sigma_{n_2^{CEW}} \right)} \tag{1.5}$$

Monitoring the CEW in principle can be used for estimating the CED to human population. Gamma-ray spectrometers for dosimetric measurements are generally calibrated by exposing them to certified radiation fields, which can be collimated beams at irradiation facilities, calibrated radioactive point sources with known activities covering both high and low energy ranges or calibration pads generally made of concrete and doped with radionuclides of known gamma dose-rates (Grasty et al., 2001; Mercier and Falguères, 2007).

In the last decades various codes devoted to the calculation of the aircraft crew's exposure to cosmic radiation have been developed on the base of Monte Carlo techniques, analytical solutions and empirical data fitting (Kleinschmidt and Watson, 2016; Spurný and Daschev, 2002). Since most of them are user friendly and well tested, their adoption for the calibration of an AGRS detector for cosmic dose estimation can be a valid option with respect to traditional characterization procedures. The popular software CARI-6P allows to calculate the different components of the cosmic effective dose received by an individual at typical cruise altitudes by relying on analytic calculations of particle transport through the atmosphere. The EXcel-based Program for Calculating Atmospheric Cosmic ray Spectrum (EXPACS) dosimetry tool permits to model the fluxes of different cosmic particles in the lower atmosphere thanks to air shower simulation performed by Particle and Heavy Ion Transport code System (PHITS) (Sato, 2015).

Both codes require information on the altitude, the geographic location and the time period, the latter related to changes in the Earth's magnetic field and in solar activity. Since the count rate in the CEW measured by a gamma spectrometer during a calibration flight is related to the electromagnetic shower

CED^{EMS}, knowing the temporal and spatial coordinates of the survey it is possible to characterize a calibration curve, which depends on the detector and on the dosimetry software tool. Once the calibration parameters have been calculated, subsequent AGRS acquisitions can provide a direct experimental measurement of the CED^{EMS}, which can be checked a posteriori with the estimation given by the dosimetry code.

1.1.3 Results and Discussion

In this section we report the results regarding the background calibration of the AGRS_16L spectrometer performed via the analysis of 1 second gamma ray spectra acquired during a 17612 seconds airborne survey over the sea. For ^{40}K and ^{214}Bi the relation between n^i and the altitude above the sea level is not guaranteed to be purely exponential down to low elevations, as the CRs in the ^{40}K and ^{214}Bi photopeaks may be contaminated by the presence of atmospheric radon. As already mentioned, this potential contamination also translates in a deviation from a purely linear relation between n^i and n^{CEW} at low elevations. The concentration of ^{222}Rn in the atmosphere can change considerably according to the different diffusion conditions. Nevertheless, above 1000-1500 m, mean ^{222}Rn concentrations of the daytime atmosphere drop sharply to values compatible with zero (around 2 ± 2 Bq/m^3) and then slowly reduce further with height until they reach 0.3 ± 0.4 Bq/m^3 above 3000 m (Williams et al., 2011). In our analysis the CRs in the KEW and in the BEW is conservatively studied only for altitudes greater than 2000 m.

Figure 1.5a shows the experimental CRs in the CEW, distinguished by colour according to the different flight IDs: the homogeneity of this partial datasets assures that there are no systematic effects related to the different acquisition times. Figure 1.5b shows the experimental data for the CRs in the CEW obtained from the entire dataset, with the superimposed curve resulting from the minimization of the χ^2 function described by Eq. (1.4). The values of the fitting curve parameters are reported in Table 1.4.

The 1.12 reduced chi-square value denotes a good agreement between the model function and the experimental data. Although the parameters A and B in the CEW (Table 1.4) are affected by uncertainties having different order of magnitudes, at the nominal 100 m survey height of an airborne survey the two uncertainties separately produce approximately the same variation on the estimated CRs, which is below 3%. Thanks to the high acquisition statistics and to the wide range of investigated altitudes, the fit well constraints the value of the μ parameter entering the exponential dependency, which is estimated with an uncertainty of 2%. Figure 1.6 shows the experimental CRs in the TEW evaluated on the entire dataset, together with the best fit exponential curve, whose parameters values are listed in Table 1.4. Also in this case the reduced chi-square value reflects the high data quality as well as the goodness of the model function in interpreting the measured CRs. The impact of the fitting parameter uncertainties on the estimated CR is negligible for what concerns μ while the uncertainties on A and B in the TEW individually give rise to a 5% variation of the predicted CR at 100 m.

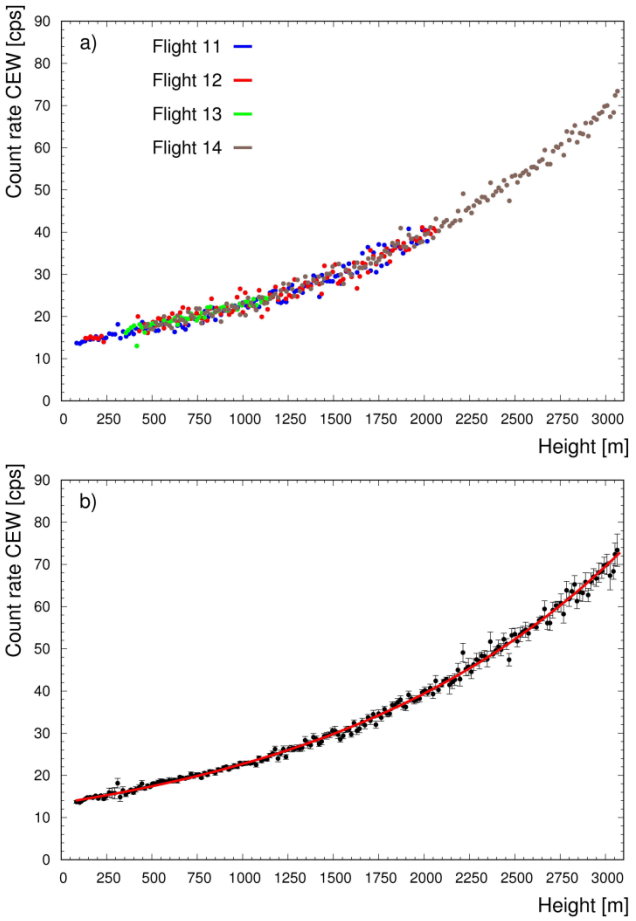

Figure 1.5. Panel a) displays the CR in the CEW as function of the altitude for the four different flights carried out during the background calibration survey over the sea. Data from different flights sit on top of each other, excluding systematic effects associated to the different acquisition times. Panel b) shows the CR in the CEW obtained from the entire dataset (black points) as function of the altitude with the superimposed exponential fit function (red solid line). Each point populating the global dataset has been obtained by clustering with an altitude binning of 15 m the spectra measured in that specific height range, disregarding any flight ID classification.

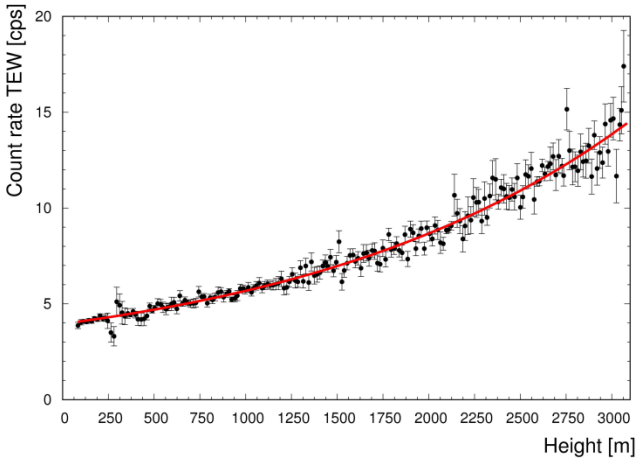

Figure 1.6. Plot of the experimental CR in the TEW as function of the altitude (black points) together with the corresponding fitting curve (solid red line).

For both the CEW and the TEW, the minimization of the χ^2 functions defined by Eq. (1.4) has been performed over the whole altitude range, corresponding to 200 height bins having a 15 m width. In both cases it is possible to recognize the presence of high statistics experimental points for height values below 200 m and around approximately 900, 2100 and 2650 m, which reflect the time flight statistics illustrated in

Figure 1.3. As a result of the definition of the objective χ^2 function, the discrepancy between the fitting function and the data is minimum in correspondence of the experimental points having the smallest statistical uncertainty.

In (IAEA, 1991) an analogous study of the CR in the TEW as function of altitude is shown: this kind of reconstruction is carried out in both cases with a NaI spectrometer having 33.6 L volume, which precludes the possibility of a direct comparison with the results of this study. However, from a qualitative point of view, it emerges that the μ coefficient entering the exponential dependence (and essentially quantifying the rate of increase of the counting statistics) is for the three cases in the range $(4 - 6) \times 10^4$ m^{-1}. Previous studies focused on a different altitude range, from around 1500 m to 4500 m: in this framework, this work demonstrates that the CR both in the CEW and in the TEW maintains its exponential behavior down to tens of meters above sea level.

The analysis of the exponential trend of the CRs with respect to the altitude could have been done in principle also for the CRs in the KEW and in the BEW, restricting the fitting domain to the range of altitudes greater than 2000 m. However, as the slope of the CR increase with respect to the altitude is small in the 2000 m to 3000 m height domain, fitting in the 2000 - 3000 m height domain would suffer the lack of the low altitude tail, producing incorrect extrapolations down to sea level. This point can be a trigger for a deeper investigation, as it can potentially be a way for exploring the content of ^{222}Rn in the lower atmosphere (Baldoncini et al., 2017).

Table 1.4. Fit parameters of the model curve formulated by Eq. (1.2) describing the CR dependence with respect to the elevation for the CRs measured in the TEW and in the CEW. The last column reports the value of the reduced χ^2 obtained at the end of the minimization procedure.

Energy Window	(A ± δA) [cps]	(μ ± δμ) [m^{-1}]	(B ± δB) [cps]	Reduced χ^2
TEW	2.4 ± 0.2	$(5.5 \pm 0.2)\times10^{-4}$	1.6 ± 0.2	0.94
CEW	11.4 ± 0.3	$(5.9 \pm 0.1)\times10^{-4}$	2.0 ± 0.4	1.12

Table 1.5. Fit parameters of the model curve formulated by Eq. (1.3) describing the dependence of the count rates in the KEW, BEW and TEW with respect to the CR in the CEW. The last column reports the value of the reduced χ^2 obtained at the end of the minimization procedure.

Energy Window	(a ± δa) [cps]	(b ± δb) [cps/cps in CEW]	Reduced χ^2
KEW	3.7 ± 0.4	0.20 ± 0.01	1.00
BEW	2.0 ± 0.4	0.16 ± 0.01	1.02
TEW	1.58 ± 0.04	0.179 ± 0.002	1.02

Figure 1.7 shows the experimental data with the superimposed linear curve resulting from the minimization of the χ^2 function described by Eq. (1.5), where the number of bins is equal to 200 for the TEW and is equal to 72 for the KEW and the BEW. Table 1.5 lists the fitting parameters together with the associated uncertainties and the reduced χ^2 value, which is almost 1 for all the three energy windows. In the perspective of using the linear relations for applying the Window Analysis Method (IAEA, 2003) to airborne gamma-ray spectra, the uncertainties estimated in Table 1.5 are relevant for attempting an evaluation of systematics associated with aircraft and cosmic background corrections. With the hypothesis of flying at 100 m height, the mentioned background CR is (6.5 ± 0.5) cps in the KEW, (4.3 ± 0.6) cps in the BEW and (4.1 ± 0.1) cps in the TEW.

For the CR in the TEW, as both the exponential and linear curve reconstructions have been performed, it is possible to check the consistency of the obtained results according to the existing relations among the fit parameters. On the base of the expected value of the CRs in the CEW and in the TEW at zero altitude, it is also possible to establish the following relationship among fit parameters:

$$A^{TEW} + B^{TEW} = a^{TEW} + b^{TEW}(A^{CEW} + B^{CEW}) \quad (1.6)$$

Adopting the parameters reported in Table 1.4 one can calculate the left hand side of Eq. (1.6), which corresponds to (4.0 ± 0.4) cps. The right hand side of the equation can be estimated using the parameters listed in Table 1.4 and in Table 1.5, which provide a count rate of (4.0 ± 0.2) cps. The perfect agreement gathered from this analysis is an important internal consistency check of the goodness of both the exponential and linear model function in interpreting the experimental data.

Eq. (1.6) describes the sum of the constant aircraft CR plus the minimum cosmic CR component, corresponding to the one determined at zero altitude. As the right hand side of Eq. (1.6) can be calculated not only for the TEW, but also for the KEW and for the BEW, it is possible to estimate the minimum detectable CRs for the three energy windows of interest. These counting statistics can be naively converted to equivalent K, U and Th abundances homogeneously distributed across an infinite flat earth by means of sensitivity coefficients obtained from a dedicated ground calibration campaign on natural sites. According to this approach it is possible to estimate that the AGRS_16L detector cannot measure K, U and Th concentrations lower than 0.05×10^{-2} g/g (15.7 Bq/kg), 0.4 µg/g (4.9 Bq/kg), 0.8 µg/g (3.2 Bq/kg), respectively.

In Figure 1.8 the CED^{EMS} calculated with the CARI-6P and EXPACS dosimetry tools shows an evident linear relation with the measured n^{CEW} values. By fitting the scatter plots with:

$$CED^{EMS} = a_{CED^{EMS}} + b_{CED^{EMS}} n^{CEW} \quad (1.7)$$

an excellent (more than 0.99) r^2 coefficient of determination has been obtained in both cases. On the base of the $a_{CED^{EMS}}$ and $b_{CED^{EMS}}$ parameters reported in Figure 1.8 caption, the AGRS_16L detector is calibrated for future measurements of CED^{EMS}. Although the described calibration method is clearly model dependent, the average discrepancy among CED^{EMS} estimations is ~10%, which is not so far from the typical uncertainties obtained with traditional methods.

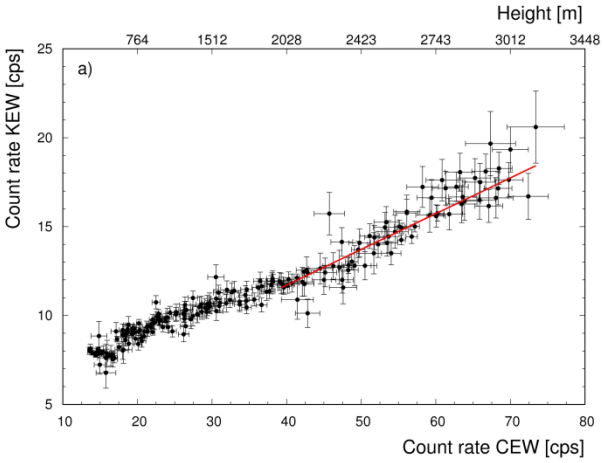

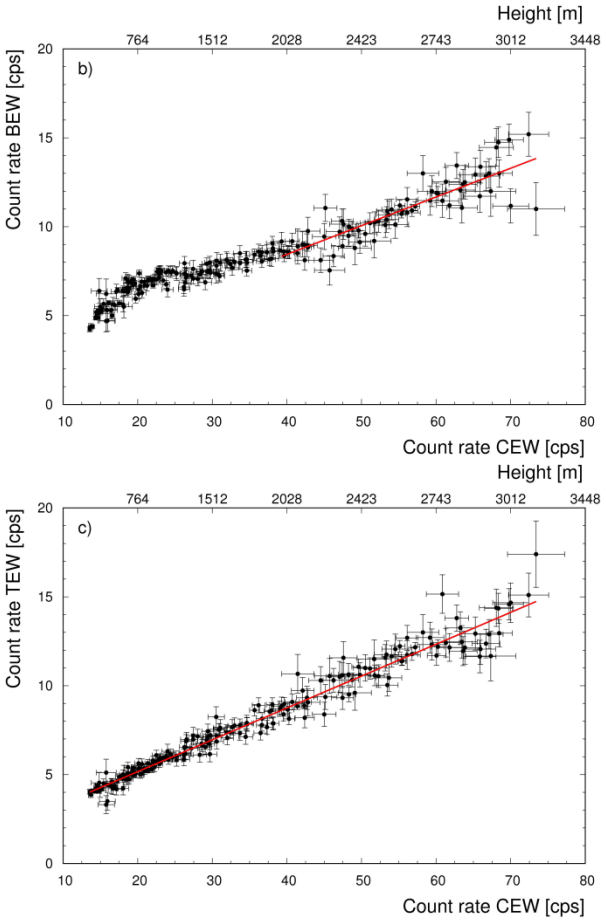

Figure 1.7. Panels a), b) and c) report respectively the experimental CRs (black points) in the KEW, in the BEW and in the TEW as function of the CR in the CEW, together with the corresponding fitting curve (solid red line).

For fixed detector and dosimetry tool, the slope and intercept parameters of Eq. (1.7) are not expected to vary significantly for different geomagnetic latitude and solar activity. On the other hand, the total CED comprises also a muon and a neutron component (respectively dominant at sea level and at high altitudes), together with additional minor contributions due to protons and He and heavy ions. In Appendix we study the relation between CED and n^{CEW} (see Figure A. 1): in the temporal and spatial domain of our data taking, a linear relation between these two quantities is clearly observed for both CARI-6P and EXPACS calculations. Since the CED varies with geomagnetic latitudes and solar activities, the obtained linear curve parameters change for different data taking conditions. However, in the typical altitude range of AGRS surveys ($z < 200$ m), the maximum variation of the CED due to solar activity rarely exceeds 5%. In Figure A. 2 of Appendix the ratio CED^{EMS}/CED is shown as function of the geographic latitude for four different altitudes, for a medium solar activity. As expected, the CED^{EMS}/CED ratio increases with increasing altitude, going from ~14% at 0 m to ~17% at 3000 m. A rule of thumb that can be formulated is that the ratio $CED^{EMS}/CED \sim 0.15$, where it has to be kept in mind that changing location, solar activity and dosimetry tool could bother this estimation.

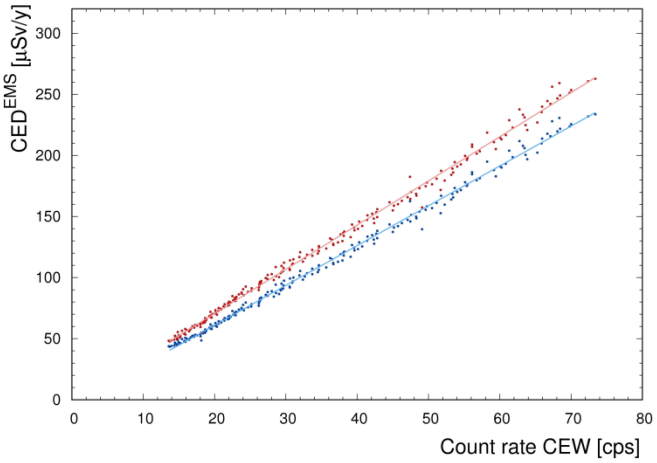

Figure 1.8. CED^{EMS} obtained by running the CARI-6P (blue points) and the EXPACS (red points) softwares with fixed location (Viareggio, 43°56'N – 10°14'E) and fixed date (31 March 2016) corresponding to the data taking conditions versus the experimental CR in the CEW. The linear fitting curves (see Eq. (1.7)) have best fit parameters equal to $a_{CED^{EMS}}$ = (-4.16 ± 0.59) µSv/y and $b_{CED^{EMS}}$ = (3.26 ± 0.02) µSv/(y·$cps) for CARI-6P (light blue solid line) and $a_{CED^{EMS}}$ = (-1.67 ± 0.67) µSv/y and $b_{CED^{EMS}}$ = (3.62 ± 0.02) µSv/(y·cps) for EXPACS (light red solid line).

1.1.4 Conclusions

This work illustrates the results of a ~5 hours airborne offshore survey dedicated to the AGRS_16L detector calibration for the gamma background signal originating from cosmic radiation and equipment radioactivity and for the assessment of cosmic effective dose to human population. This airborne campaign has been conducted with the Radgyro, an ultra-light aircraft dedicated to multispectral airborne surveys, and has the peculiarity of having investigated a wide range of altitudes above sea level (77-3066 m). The acquisition of 17612 1 second spectra over the sea at different altitudes allowed to separate the background count rate into a constant aircraft component and a cosmic component exponentially increasing with increasing height.

A statistical analysis has been performed to determine the parameters that linearly relate the count rate (CR) in the energy windows associated to the K, U and Th photopeaks and the counting statistics recorded in the cosmic energy window (CEW) in which no event coming from terrestrial radioactivity is expected. By monitoring the CR in the CEW and by applying the obtained linear relations it is possible to calculate for every airborne gamma-ray spectrum the background CRs in the photopeaks of interest that need to be subtracted prior the implementation of the height and stripping corrections before finally convert corrected elemental CRs to ground abundances. Minimum detectable K, U and Th abundances have been inferred from the minimum detectable CRs in the KEW, BEW and TEW, which correspond to the overall background CRs at zero altitude. On the basis of ground sensitivity coefficients, it is possible to assess that the minimum detectable abundances of the AGRS_16L detector are 0.05×10^{-2} g/g, 0.4 µg/g, 0.8 µg/g, for K, U and Th respectively.

For the CRs in the CEW and in the TEW the exponential increase of counting statistics with respect to the altitude has been reconstructed, providing as argument for the exponential function a µ coefficient of 6×10^{-4} m^{-1} which is comparable with the values published in (IAEA, 1991) and (Grasty and Minty, 1995). Moreover, the analysis of the CRs in the TEW highlighted a perfect internal consistency among linear fit and exponential fit parameters. The exponential analysis for the CRs in the KEW and in the BEW was unfeasible due to the application of a low altitude cut to the dataset (z>2000 m), which allowed to exclude potential contamination caused by atmospheric ^{222}Rn. This point, however, deserves a deeper investigation as deviations from purely exponential/linear behaviors could in principle be used to quantify the atmospheric ^{222}Rn abundance at different elevations (Baldoncini et al., 2017).

1.2 Exploring atmospheric radon with airborne gamma-ray spectroscopy

^{222}Rn is a naturally occurring noble gas produced via alpha decay of ^{226}Ra and it is the only gaseous daughter product of the decay chain of ^{238}U, which is present in the majority of soil and rock types and which has a half-life of $\sim 4.5 \cdot 10^9$ yr, comparable to the Earth's age. As ^{222}Rn is inert and hardly soluble in water, it exhales from soils and rocks into the atmosphere and migrates by diffusion and convection almost without being subject to atmospheric removal processes, therefore running out mainly through radioactive decay (Jacobi and Andre, 1963). ^{222}Rn atmospheric abundance is strictly connected with its exhalation rate from soils, which is typically on the order of 0.8 - 1.2 atoms/(cm^2·s) and which is in turn affected by soil type, granulometry and moisture content, as well as by porosity and permeability (Manohar et al., 2013; Szegvary et al., 2009; Turekian et al., 1977).

The poor chemical reactivity, together with the 3.82 days half-life, makes ^{222}Rn a conventional and widespread atmospheric tracer. Indeed, ^{222}Rn has a relatively long half-life for being connotative of events related to turbulence (having a typical 1 hour time scale), but it also lasts shortly enough to have a high concentration gradient through the lower troposphere that can give insights into air vertical mixing mechanisms and help in tracing air transport processes.

Variations in the vertical radon concentration profiles produce changes in the natural background gamma-ray flux which, in turn, can be responsible for perturbations and contaminations in aerial monitoring results (Beck, 1974). ^{214}Pb, having a half-life of 26.8 minutes, and ^{214}Bi, having a half-life of 19.8 minutes, are the two principal gamma-emitting daughters of ^{222}Rn, which, thanks to their short decay time, are usually in equilibrium with each other (i.e., their activities are about the same at all elevations). When the vertical mixing conditions are not characterized by quick variations (as instead happens close to sunrise and sunset), the steady state is generally reached which means that the concentration profiles of radon and its daughters tend to be near secular equilibrium, except near ground (h < 25 m) (Gogolak, 1977).

Airborne gamma-ray spectroscopy always treated ^{222}Rn as a source of background since it affects the indirect estimate of equivalent ^{238}U concentration. In this work the AGRS method is used for the first time for quantifying the presence of ^{222}Rn in the atmosphere and assessing its vertical profile.

High statistics radiometric data acquired during an offshore survey are fitted as a superposition of a constant component due to the experimental setup radioactivity plus a height dependent contribution due to cosmic radiation and atmospheric ^{222}Rn. I contributed to the refined statistical analysis which provides not only a conclusive evidence of AGRS ^{222}Rn detection but also a (0.96 ± 0.07) Bq/m^3 ^{222}Rn concentration and a (1318 ± 22) m atmospheric layer depth fully compatible with literature data.

1.2.1 Experimental setup, survey and data

Three AGRS surveys have been performed over the Tyrrhenian Sea in proximity of Viareggio (Tuscany, Italy). The aircraft used to carry out the surveys is a prototype autogyro called Radgyro (see Figure 1.9), whose engineering has been expressly devised in order to accommodate for a set of sensors able to detect at the same time electromagnetic waves belonging to the infrared, thermal, visible and gamma spectral ranges. The modularity of the experimental setup, the high autonomy and the payload (3 hours for a 120 kg equipment

weight) make the Radgyro a flying multisensorial platform which can be potentially employed in a wide family of applications in the field of proximal remote sensing.

Figure 1.9. Picture of the Radgyro taken during the airborne gamma-ray survey over the sea.

Along with electromagnetic wave detectors, the Radgyro is equipped with a couple of u-blox EVK-6T GPS antennas. Each antenna has as output an ASCII file listing for each second the absolute PC and GPS times and a binary file which is processed with the goGPS software (Herrera et al., 2016) for the extraction of the geographic latitude and longitude, together with the orthometric altitude at 1Hz. From this set of outputs it is possible to determine with a 1Hz frequency the altitude, latitude and longitude of the aircraft by averaging the individual readouts of the two antennas referred to the computer acquisition time, which is necessary in order to synchronize position with radiometric data. Gamma-ray measurements are performed with a modular NaI(Tl) scintillation detector arranged in the middle of the Radgyro hull, the AGRS_16L, which is made up of 4 4L crystals having dimensions equal to 10 cm × 10 cm × 40 cm (Guastaldi et al., 2013; Strati et al., 2015). Scintillation light is amplified by means of a 14 pin PMT base whose output signal is processed by a CAEN DT5740 digital pulse charge integrator, a 12 bit 62.5 MS/s waveform digitizer able to provide for 32 separate channels the list mode readout, i.e. an ASCII file for each channel reporting, for each energy deposition inside the specific crystal, the time stamp in units of digitizer clock and the acquisition ADC channel. The PMT high voltage and the gain of the electronics are set in order to acquire gamma-ray spectra for the 4 NaI(Tl) crystals having comparable dynamics and reaching an energy of 7 MeV. The output list mode files are offline processed in order to generate for each detector energy calibrated gamma spectra corresponding to 1 second acquisition time which are summed up to obtain the gamma-ray spectrum resulting from the whole 16L detection volume. Radiometric data entering this analysis have been selected on the base of a 300 m minimum distance of the aircraft from the coast, which is meant to exclude gamma-ray signals potentially spoiled by ground radiation. According to this selection cut, the overall effective acquisition statistics for the three flights is 14688 seconds, as reported in Table 1.6 along with the main features referred to the single surveys.

Table 1.6. Summary of the main parameters for each of the 3 surveys over the sea. For each flight the ID, date, time, minimum and maximum altitude and acquisition time are reported, respectively. In the case of flights 11 and 14, 83 seconds and 30 seconds have been cut due to some radiofrequency interference between the PMT and the aircraft transponder. The long interruption in the data taking of flight 12 (2531 seconds) has been imposed by civil traffic of the Pisa airport.

Flight ID	Date	Time	z min [m]	z max [m]	Acquisition time [s]	T [°C]	P [hPa]	W [km/h]	Sky conditions

11	30/03/2016	17:42:10 19:29:43	77	2019	6370	18.6 14.9	1016.8 1015.3	17 15	Mostly clear
12	31/03/2016	18:13:55 19:46:47	126	2070	3041	22.2 19.7	1010.3 1009.9	17 11	Mostly clear
14	05/04/2016	16:37:16 18:05:43	461	3066	5277	24.6 20.7	1007.2 1015.7	17 2	Clear
Global			77	3066	14688				

The estimated count rates in the energy windows of interest have been clustered according to an altitude binning of 15 m, which is conservative with respect to the estimated accuracy on the vertical position resulting from the combination of the altimetric data acquired by the instrumental setup mounted on board of the Radgyro. The count rates are estimated summing all the input count rates acquired in the same elevation bin and dividing by the number of 1 second spectra entering the summation. Figure 1.10 shows the count rates measured respectively in the ^{214}Bi Energy Window (BEW, 1.66 -1.86 MeV), ^{208}Tl Energy Window (TEW, 2.41 - 2.81 MeV) and Cosmic Energy Window (CEW, 3.0 - 7.0 MeV) as function of the altitude above sea level, distinguished according to the different flights. In the TEW and CEW the variation of the count rates in different flights is compatible with the statistical fluctuation of the count rates: there is no systematic effect related to the different flight times and the exponential behavior is maintained down to low elevations. For the count rates in the BEW there is some evidence of data clustering for different flights, in particular at low elevations, which is a hint of the presence of ^{222}Rn gas in the atmosphere.

1.2.2 Theoretical model

^{222}Rn daughter products ^{214}Pb and ^{214}Bi are the main gamma-emitters in the ^{238}U decay chain and, since they bind to airborne aerosols, they are responsible of the measured radon background. Estimates of the ^{238}U content via AGRS measurements rely on the evaluation of background subtracted count rates in the ^{214}Bi photopeak energy window (BEW), which corresponds to the (1660-1860) keV energy range centered on the 1765 keV ^{214}Bi gamma emission line. Background correction involves the removal of gamma signal of non-geologic nature, which consists of three components resulting respectively from the decay of ^{214}Bi in the atmosphere, the radioactivity of the aircraft and its equipment due to presence of trace amounts of ^{238}U and ^{232}Th, and the interaction of secondary cosmic radiation with the air, the aircraft and the detector (Minty, 1998). AGRS detectors are generally calibrated for the aircraft and cosmic background by performing high-altitude offshore flights in an area where atmospheric radon is at minimum. Spectra are measured in a range of heights, typically from 1.0 - 1.5 km up to 3.0 - 3.5 km over water with a 300 - 500 m step, for generally 10 - 15 minutes accumulation time at each height (IAEA, 2003).

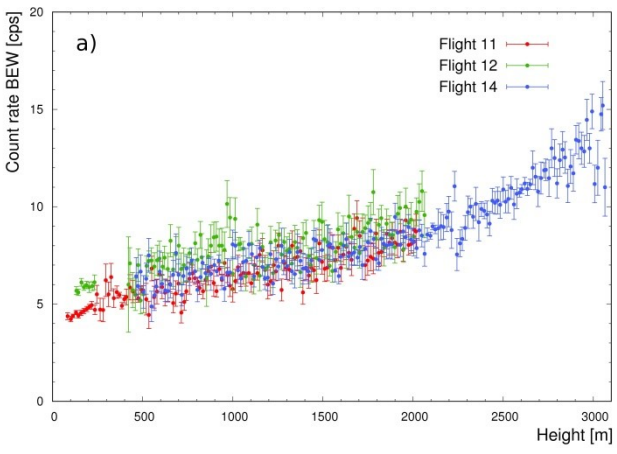

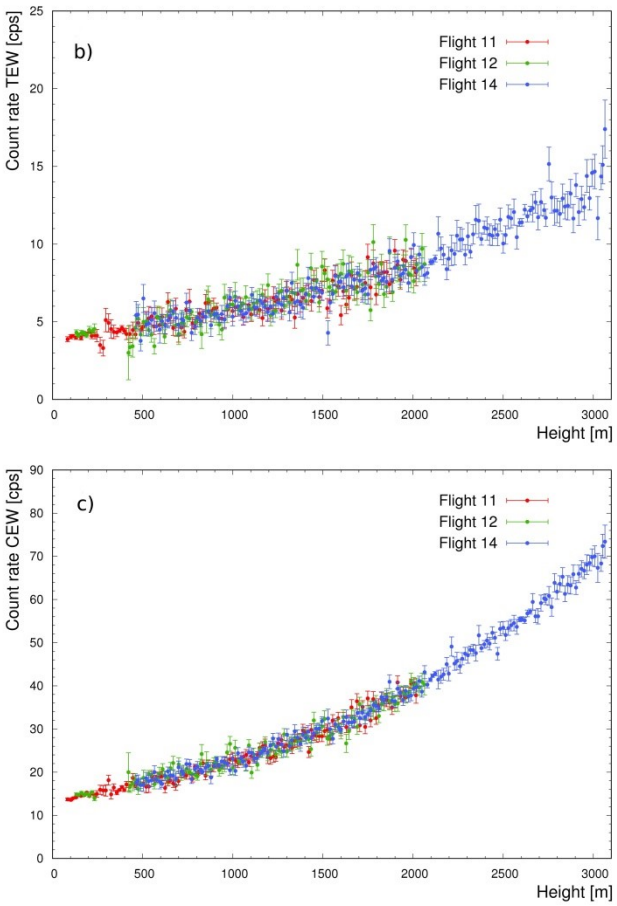

Figure 1.10. Panels a), b) and c) show the count rate respectively in the BEW, TEW and CEW as function of the altitude for the 3 different flights carried out during the survey over the sea. In the TEW and CEW experimental data from different flights sit on top of each other, excluding systematic effects associated to the different acquisition times. In the BEW it is possible to recognize the effect of atmospheric radon contamination for the 3 different flights.

In the absence of radon gas, the count rate in the BEW can be described as a superposition of a constant aircraft component and a cosmic component which is expected to exponentially increase with increasing height above sea level as stated by the following equation:

$$n_{BEW}^{aircraft+cosmic}(z) = A_{BEW}e^{\mu_{BEW}z} + B_{BEW} \tag{1.8}$$

where $n_{BEW}^{aircraft+cosmic}(z)$ is the count rate in the BEW and A_{BEW}, μ_{BEW} and B_{BEW} are constants (Grasty and Minty, 1995; IAEA, 1991). This radon free model is expected to accommodate experimental measurements, generally at altitudes greater than 2000 m. Indeed, although the atmospheric concentration of ^{222}Rn and of its daughter products can vary significantly with different diffusion conditions, mean ^{222}Rn concentrations are (4 ± 3) Bq/m^3 in the lowest 30 - 1000 m, while above 1000 - 1500 m mean ^{222}Rn concentrations generally show a steep decrease to values compatible with zero (around (2 ± 2) Bq/m^3, dropping even further to (0.3 ± 0.4) Bq/m^3 above 3000 m (Williams et al., 2011). When looking to experimental data acquired at low altitudes, a deviation from the mentioned exponential behavior can be observed due to radon accumulation in the atmosphere. Traditionally, the presence of atmospheric radon is identified as a breakdown of the linear relation that is supposed to hold between the count rates in the BEW and the count rates measured in the CEW, the latter having exclusively cosmic origin since the maximum terrestrial gamma energy corresponds to the 2614 keV ^{208}Tl emission (Grasty and Minty, 1995).

An alternative model can be developed with the aim of covering the entire altitude range and of recognizing and possibly quantifying the presence of the radon gas in the atmosphere via the detection of the gamma-signal generated by the ^{214}Bi decay. In presence of atmospheric radon, the overall count rate recorded in the BEW $n_{BEW}(z)$ comprises not only the aircraft plus cosmic component $n_{BEW}^{aircraft+cosmic}(z)$ (see Eq (1.8)) but also an altitude dependent component arising from atmospheric ^{214}Bi $\left(n_{BEW}^{Rn}(z)\right)$ whose modeling requires a radon vertical profile, which is in turn directly connected with the dynamics of the atmospheric boundary layer.

The diurnal evolution of the atmospheric boundary layer, i.e. the ~1-2 km thick layer where the atmosphere feels the contact with the ground surface, is governed by the mechanical and thermal surface-air interactions which are respectively driven by wind and solar radiation. Under clear sky conditions, after sunrise the warmed ground heats the air touching the ground, creating thermals that rise and cause intense motions which gradually create a convective boundary layer (or mixed layer), generally characterized by high homogeneity. As time passes, the growing convective region reaches higher altitudes till at sunset thermals cease and convection terminates, leading to the formation of a residual layer containing near zero turbulence and the residual moisture, heat, and pollutants that were mixed during the day. As long as the weather remains fair the cycle repeats on a daily timescale, with a mixing efficiency that partially depends on the amount of cover due to clouds which can intercept portions of the sunlight and reduce the amount of heat delivered to ground level (Stull, 2012).

In cases of fair weather, for convective boundary layers a very marked drop in radon concentrations is generally observed in crossing the separation between the mixed layer and the free troposphere, where radon abundances reach typically near-zero values (Williams et al., 2011). In the case of mixed layers topped with residual layers radon exhibits a fairly constant profile in the mixed layer and tends to reduce linearly with height in the residual layers.

As the airborne campaign was conducted under clear sky conditions in a narrow range of days and always in the late afternoon, the simplified radon vertical profile adopted in this study is a discrete model according to which the radon concentration is uniform up to a cutoff altitude s, basically corresponding to the depth of the mixed layer, and null above the cutoff height. Figure 1.11 shows a schematic example of the behavior of the field of view of the gamma-ray detector to ^{214}Bi gamma signal as it moves to increasing altitude, starting from sea level up to the separation height between the two radon gas layers, till it reaches the radon free zone.

In the lower layer where the radon activity is uniform, the contribution to the count rate in the BEW originated by the atmospheric ^{214}Bi has a monotonic increase with increasing altitude. Indeed, at altitude zero the detector field of view can be approximated by a half-sphere as the gamma photon flux has only a downward incoming direction; when the detector starts lifting from sea level an upward incoming photon flux will start being visible enhancing the detected gamma signal. At an altitude equal to half the separation height $n_{BEW}^{Rn}(z)$ will reach its maximum. If the cutoff altitude s is high enough (for s > 400 m, corresponding to ~2.3 photon mean free paths, the count rate gradient will be < 0.01%), the maximum count rate will reach a saturation value almost equal to double the count rate recorded at sea level, corresponding to the full-sphere field of view. Approaching the separation height s, the $n_{BEW}^{Rn}(z)$ count rate will start monotonically decreasing till it vanishes when the detector is far enough from the lower radon layer.

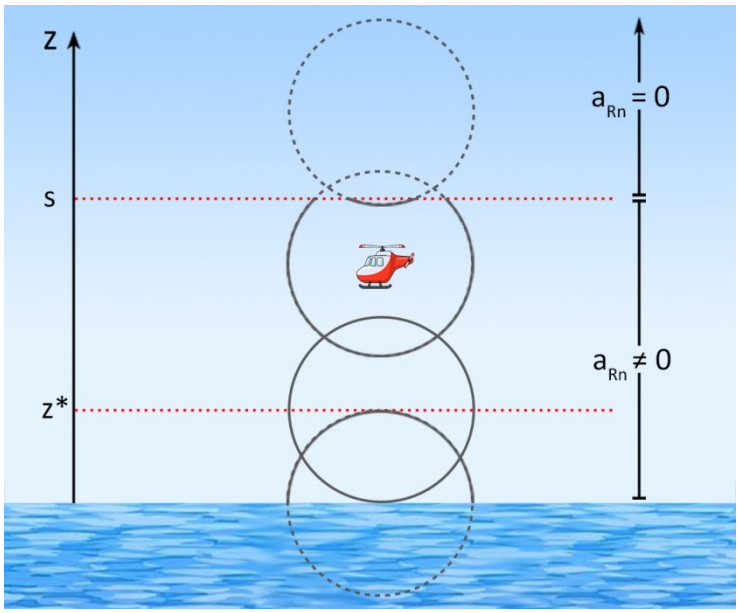

Figure 1.11. Schematic illustration of the variation of the detector field of view to the atmospheric ^{214}Bi gamma signal with respect to the height. When the detector is at sea level, the field of view will be that of a half-sphere. With increasing height the detector starts seeing the upward photon flux till the field of view reaches saturation at the altitude z*, corresponding to the full-sphere case. Approaching the separation altitude s between the two radon layers the field of view starts shrinking and finally vanishes when the detector is completely immersed in the radon free layer.

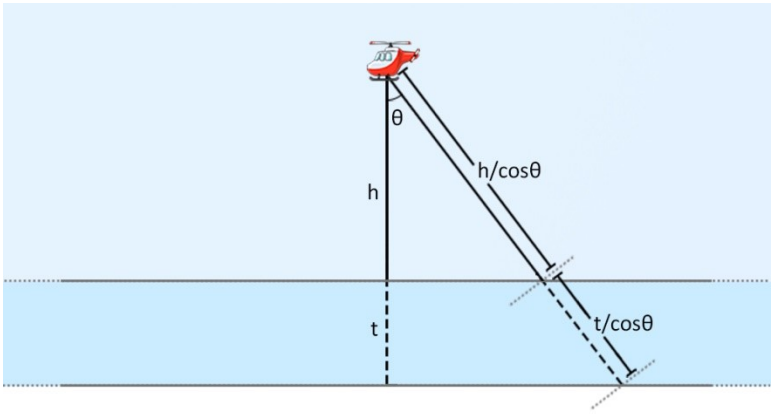

Figure 1.12. Schematic diagram of the geometrical model adopted for estimating the unscattered photon flux reaching a detector situated at a vertical distance h from a source having infinite lateral extension and thickness t. In this context the source of thickness t corresponds to an air layer in which a homogeneous radon concentration is present.

From the theoretical point of view it is necessary to model the propagation of unscattered photons from the source to the detector position (Figure 1.12). The flux of unscattered 1765 keV photons emitted by atmospheric ^{214}Bi is given by the following equation:

$$\Phi = \frac{A_t P_\gamma}{2\mu_a} \int_0^1 dcos\theta e^{\frac{-\mu_a h}{cos\theta}} \left[1 - e^{\frac{-\mu_a t}{cos\theta}}\right] \qquad (1.9)$$

where A_t is the volumetric gamma activity in [γ/m^3] of the uniformly distributed ^{214}Bi, μ_a is the air linear attenuation coefficient referred to 1765 keV photons, t is the thickness of the air layer in which gamma photons are homogeneously and isotropically emitted, h is the vertical distance of the detector from the source layer. By scaling for the detector cross sectional area and by some efficiency factor, Eq. (1.9) directly translates into the expression describing the variation of the count rate as function of altitude.

The $n_{BEW}^{Rn}(z)$ vertical profile can be modeled by distinguishing the case in which the detector vertical position z is below or above the cutoff altitude s. In both scenarios the air layer at an altitude greater than s does not give any contribution to the signal as it has zero activity volume concentration. As illustrated in Figure 1.13a, when the detector position z is below the cutoff altitude s, two air source layers having thickness respectively equal to z and s-z contribute to the radon count rate with $n_1(z)$ and $n_2(z)$ as stated by the following equation:

$$n_{BEW}^{Rn}(z) = n_1(z) + n_2(z) = C\int_0^1 dcos\theta\left[1 - e^{\frac{-\mu_a z}{cos\theta}}\right] + C\int_0^1 dcos\theta\left[1 - e^{\frac{-\mu_a (s-z)}{cos\theta}}\right] \quad (z < s) \tag{1.10}$$

where C is the count rate in cps measured at zero distance from a semi-infinite homogeneous air volume source, i.e. the count rate obtained for h = 0 and t → ∞ (see Eq. (1.9)). If the detector position is above the cutoff altitude (z>s), the count rate arises only from layer number 3 (see Figure 1.13b), where the air source layer thickness is s and the detector vertical distance from the source is z-s, corresponding to:

$$n_{BEW}^{Rn}(z) = n_3(z) = C\int_0^1 dcos\theta e^{\frac{-\mu_a (z-s)}{cos\theta}}\left[1 - e^{\frac{-\mu_a s}{cos\theta}}\right] \tag{1.11}$$

Therefore, the theoretical expression for the count rate in the BEW $n_{BEW}^{Rn}(z)$ can be summarized according to the following equation:

$$n_{BEW}^{Rn}(z) = \Theta(s-z)[n_1(z) + n_2(z)] + \Theta(z-s)n_3(z) \tag{1.12}$$

where Θ(x) represents the Heaviside step function.

Figure 1.14 shows a representative example of the $n_{BEW}^{Rn}(z)$ curve. As expected, the curve is symmetrical with respect to an altitude value equal to half the separation height s. The separation altitude s corresponds to ~8.7 photon mean free paths, which is a long enough distance for the count rate at sea level $n_{BEW}^{Rn}(0)$ to reach the C value, corresponding to the count rate associated to a semi-infinite volume source. Similarly, $n_{BEW}^{Rn}(z)$ gets to reach and maintain the saturation value equal to 2C before starting to decrease when the altitude approaches s.

The overall count rate in the BEW can be therefore expressed according to the following equation:

$$n_{BEW}(z) = A_{BEW}e^{\mu_{BEW}z} + B_{BEW} + \Theta(s-z)[n_1(z) + n_2(z)] + \Theta(z-s)n_3(z) \tag{1.13}$$

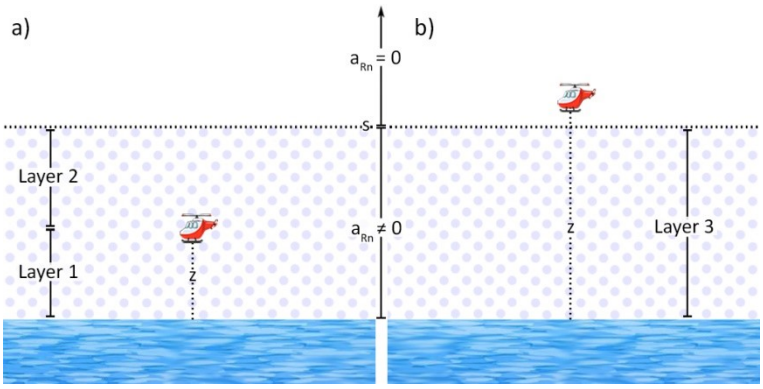

Figure 1.13. Schematic illustration of the air layers generating the radon contribution to the count rate in the BEW. When the detector vertical position z is below the cutoff altitude s (which separates the lower atmospheric portion having uniform radon concentration

from the upper one which has null radon abundance), there are two layers generating the ^{214}Bi gamma signal (a). When the detector vertical position z is above the cutoff altitude s, there is only one layer generating the ^{214}Bi gamma signal (b).

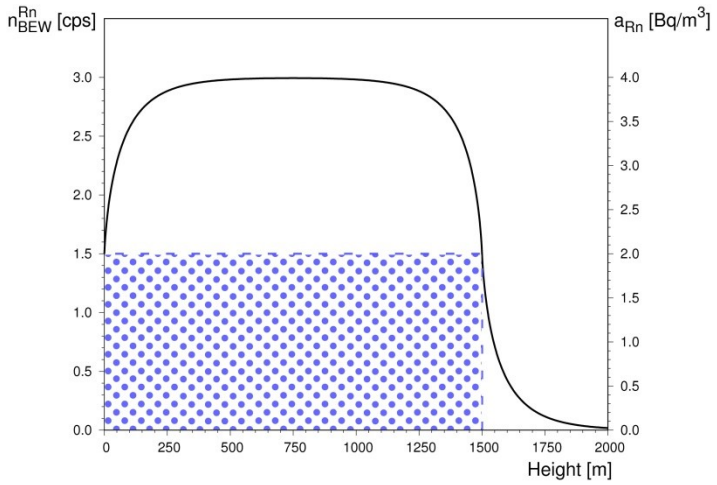

Figure 1.14. The black solid line illustrates the $n_{BEW}^{Rn}(z)$ count rate (left y axis) as function of the altitude for a C count rate value equal to 1.5 cps, a gamma linear attenuation coefficient μ_a equal to 0.005829 m^{-1} and a cutoff altitude s equal to 1500 m (see Eq. (1.12)). The blue polka-dotted pattern represents the 2 Bq/m^3 homogeneous radon concentration (right y axis) in the atmospheric layer below 1500 m. In the air layer at altitude larger than 1500 m the radon concentration vanishes.

Figure 1.15 shows the global behavior of $n_{BEW}(z)$, together with the separate components associated with the aircraft plus cosmic background and with the radon background. The radon contribution produces a curvature in the model function which is evident in the low altitude range (z<200 m) where the initial half-spherical field of view approaches a full-spherical field of view. After the radon component has reached the plateau, the model curve grows in parallel to the radon free curve just shifted upward by the radon saturation count rate. In approaching the separation altitude between the two radon layers the model curve exhibits a kink, whose vertical extent depends on the values of the exponential function parameters and of the radon concentration gradient between the two layers. This kink translates into a local count rate decrease till the model curve matches the curve obtained in the radon free scenario at an altitude which is ~400 m higher than the cutoff altitude.

1.2.3 Determination of the count rate vertical profile parameters

The two theoretical models described in the previous section have been used in order to reconstruct the observed count rate in the BEW as function of altitude. The parameters of the theoretical curves have been determined via the minimization of a χ^2 function. For the radon free model the χ^2 minimization has been performed for the count rates measured at elevations greater than 2000 m, where the condition of absence of radon is supposed to hold. On the base of Eq. (1.8), the following definition of the χ^2 function has been used:

$$\chi^2 = \sum_{j=1}^{N} \left[\frac{n_{BEW}^j - (A_{BEW} e^{\mu_{BEW} z_j} + B_{BEW})}{\sigma_{n_{BEW}^j}} \right]^2 \qquad (1.14)$$

where N is 79, equal to the number of experimental data measured at z_j>2000 m, n_{BEW}^j is the count rate in the BEW measured at z_j, z_j is the average elevation obtained for the j-th elevation bin and $\sigma_{n_{BEW}^j}$ is the 1 sigma uncertainty associated to the counting statistics, corresponding to the square root of the total counts

recorded at z_j in the BEW divided by the acquisition time. For the model containing the radon contribution, the χ^2 minimization has been performed over the entire altitude range corresponding to the 14688 seconds of data taking. On the basis of Eq. (1.8), the following definition of the χ^2 function has been used:

$$\chi^2 = \sum_{j=1}^{N} \left[\frac{n_{BEW}^j - \left(A_{BEW} e^{\mu_{BEW} z_j} + B_{BEW} + \Theta(s - z_j)[n_1(z_j) + n_2(z_j)] + \Theta(z_j - s) n_3(z_j) \right)}{\sigma_{n_{BEW}^j}} \right]^2 \quad (1.15)$$

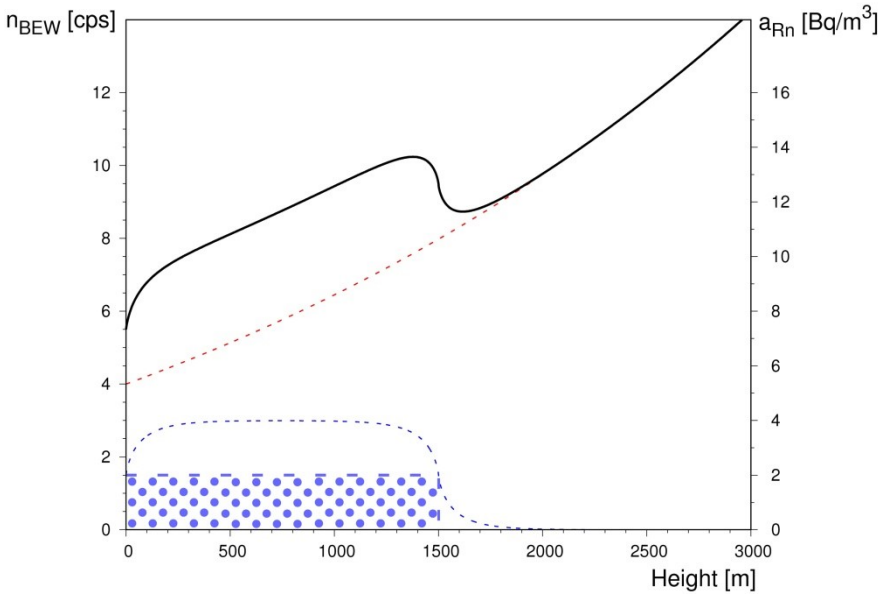

Figure 1.15: The blue dashed line shows the curve for the count rate in the BEW (left y axis) due to the presence of atmospheric radon $n_{BEW}^{Rn}(z)$ obtained for a cutoff altitude s equal to 1500 m and a C value of 1.5 cps (see Eq. (1.12)). The blue polka-dotted pattern represents the 2 Bq/m^3 homogeneous radon concentration (right y axis) in the atmospheric layer below 1500 m. In the air layer at altitude larger than 1500 m the radon concentration vanishes. The red dashed line shows the aircraft plus cosmic contribution obtained with A_{BEW} = 7 cps, μ_{BEW} = 3·10^{-4} m^{-1} and B_{BEW} = -3 cps (see Eq. (1.8)). The black solid line represents the overall count rate in the BEW, determined as the sum of the aircraft plus cosmic contribution and the atmospheric radon contribution (see Eq. (1.13)).

where N is 423, equal to the number of experimental data measured in the entire altitude range, and n_{BEW}^j, z_j, $\sigma_{n_{BEW}^j}$ defined as previously described. The best fit solutions have been found using a fixed value for the 1765 keV gamma linear attenuation coefficient μ_a equal to 0.005829 m^{-1}.

1.2.4 Results and discussion

Figure 1.16 shows the results of both χ^2 minimization procedure; the parameters obtained at the end of the fitting procedures are reported in Table 1.7.

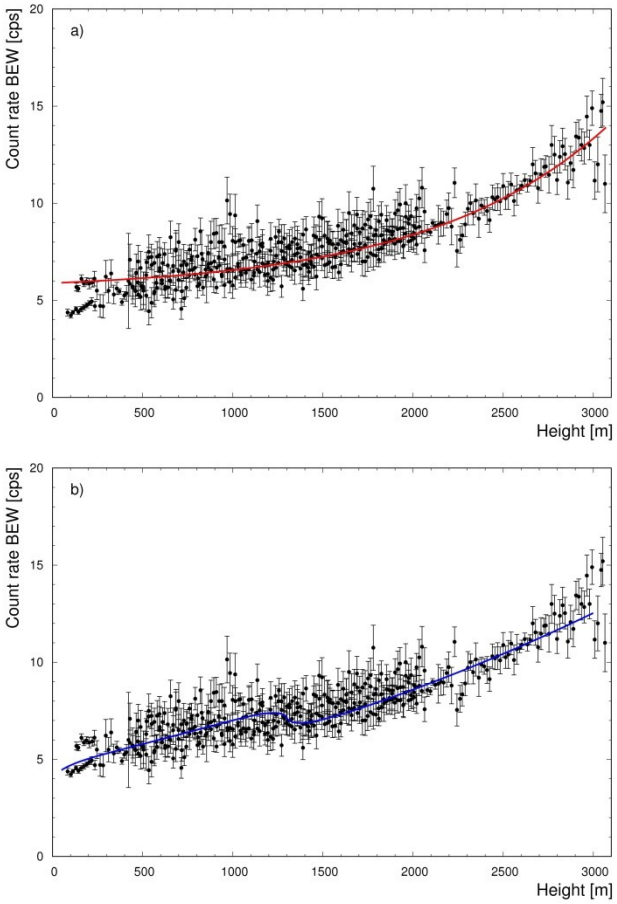

Figure 1.16. Panel a) shows the count rate recorded in the BEW during the entire survey (black points) together with the curve (red solid line) obtained by fitting the data acquired at z>2000 m with a theoretical model that includes only the aircraft and cosmic components of the gamma signal (see Eq. (1.8)). Panel b) shows the same dataset (black points) with the model curve (blue solid line) obtained by fitting the data acquired in the entire elevation range with the theoretical model that accounts also for the presence of radon in the atmosphere (see Eq. (1.13)).

Table 1.7. Fit parameters of the model curves defined by Eq. (1.8) and by Eq. (1.13) describing the dependence with the altitude of the count rate in the BEW respectively in the absence or presence of atmospheric radon. The last column reports the value of the reduced χ^2 referred to the entire range of investigated altitudes.

Theoretical model	$A_{BEW} \pm \delta A_{BEW}$ [cps]	$\mu_{BEW} \pm \delta\mu_{BEW}$ [cps]	$B_{BEW} \pm \delta B_{BEW}$ [cps]	$s \pm \delta s$ [m]	$C \pm \delta C$ [cps]	Reduced χ^2
Without Rn (Eq. (1.8))	0.39 ± 0.07	$(1.0 \pm 0.1)\cdot 10^{-3}$	5.5 ± 0.3	/	/	5.0
With Rn (Eq. (1.13))	8.2 ± 0.2	$(2.54 \pm 0.06)\cdot 10^{-4}$	-4.9 ± 0.2	1318 ± 22	0.68 ± 0.05	2.1

A theoretical model accounting only for the cosmic and aircraft component is not satisfactory in describing the data distribution, especially at low elevations. Indeed, the model allowing for the presence of radon in the atmosphere provides a better fit to the data, as proved by the reduction of the reduced χ^2 value from 5.0 for the radon free model to 2.1 for the model accounting for radon in the atmosphere. Moreover, the goodness of the A_{BEW} and B_{BEW} fit parameters can be checked according to their relation with the parameters of the linear function describing the relation between the count rates in the BEW and the count rates in the CEW:

$$A_{BEW} + B_{BEW} = a_{BEW} + b_{BEW}(A_{CEW} + B_{CEW}) \quad (1.16)$$

On the base of the values obtained from an independent aircraft plus cosmic background calibration survey the right hand side of Eq. (1.16) is estimated to be (4.1 ± 0.7) cps. The value obtained for the left hand side of Eq. (1.16) according to the radon free model is (5.9 ± 0.4) cps, while the model accounting for atmospheric radon provides (3.3 ± 0.4) cps, which are respectively incompatible and compatible at 1σ level with the right hand side value. The fit value for the s parameter is equal to (1318 ± 22) m, comparable with atmospheric radon ranges reported in (Williams et al., 2011).

The fit value for the C parameter corresponds to the sea level count rate associated to the presence of radon (and its gamma emitting daughter nuclei) in the atmosphere, which can be converted into radon abundance, provided a sensitivity calibration factor. From an independent ground calibration campaign, the sensitivity matrix necessary for the estimation of the natural radionuclide concentrations via the Window Analysis Method has been determined (IAEA, 1991). The S_{UU} = 0.71 cps/(Bq/m^3) element of the sensitivity matrix, corresponding to the count rate in cps in the BEW for unitary concentration of eU in ppm, has been adopted for having a crude estimate of a (0.96 ± 0.07) Bq/m^3 mean radon concentration in the atmospheric (mixed) layer having (1318 ± 22) m depth. The obtained values for the mean radon abundance and for the mixed layer height are comparable with data published by (Williams et al., 2011) and (Chen et al., 2016). In Figure 6 of (Chen et al., 2016) it is shown that radon concentration is inversely related to the mixing layer height, corresponding typically to about 1 Bq/m^3 for a mixing layer height of 1500 m. Moreover, the diurnal variations of radon abundance and mixing layer height in different season (Figure 5 of (Chen et al., 2016)) show that typical values of radon abundance in the spring late afternoon are about 1.2 Bq/m^3 for a mixing layer height of ~1000 m.

A further generalization of the 1 layer model having radon contribution described by Eq. (1.12) led to the theoretical description of a 2 layers model built by introducing the s_1, s_2, C_1 and C_2 model parameters in the mathematical description of the count rate. s_1 and s_2 correspond to the separation altitudes of a lower and a higher atmospheric layer characterized respectively by a C_1 and C_2 count rate. The best fit with the 2 layers model provided a χ^2=2.0 and s_1 = (1166 ± 12) m, Rn_1 = (1.24 ± 0.09) Bq/m^3, s^2 = (1562 ± 28) m and Rn_2 = (0.6 ± 0.1) Bq/m^3, where Rn_1 and Rn_2 have been obtained by dividing the C_1 and C_2 cps values by the S_{UU} constant. The 2 layers and 1 layer models fit the experimental data with essentially the same statistical significance, providing almost equal χ^2 values. According to the quality of our dataset, is not feasible to have a clear discrimination between a 1 layer model and a 2 layers model: indeed, the 1 layer model having best fit parameters s=(1318 ± 22) m and Rn=(0.96 ± 0.07) Bq/m^3 basically represent the same scenario of a 2 layers model characterized by the above mentioned best fit parameters s_1, s_2, C_1 and C_2, where the average separation altitude and the average radon content essentially reproduce the s and Rn values provided by the 1 layer model.

1.2.5 Conclusions and perspectives

Radon measurements are typically performed by counting experiments of alpha-particles or beta-particles emitted in the decay of radon progeny, requiring the collection and filtering of air mass samples which is a time consuming and laboratory intense procedure. In this work we proved the feasibility of performing atmospheric ^{214}Bi AGRS measurements and of assessing its abundance and vertical distribution. However, the discrimination of ^{214}Bi gamma emissions from other sources of radiation is far from being trivial: long acquisitions in a wide range of altitudes are a key ingredient for splitting the different contributions to the measured count rates. Indeed, according to the quality of the experimental dataset it has not been possible to statistically discriminate a simplified one layer radon vertical distribution from a more refined two layers radon vertical profile. In perspective, AGRS measurements carried out with large detectors (e.g. the typical 33 L NaI(Tl) systems) mounted on helicopters, which differently from autogyros are able to hover,

could provide high statistics experimental data at well separated altitudes potentially increasing the resolution on different ^{222}Rn vertical strata.

Chapter 2

From the atmosphere to the soil: ^{214}Pb rain-induced gamma activity

The transient enhancement of gamma activity occurring during and after a precipitation event has been observed worldwide in the last decades and plays an important role in variations of the environmental gamma radiation background (Minato, 1980; Yakovleva et al., 2016). The main sources of rain-induced gamma activity at ground level are ^{214}Pb and ^{214}Bi which are collected by rain droplets and brought to the ground after being produced in the decay of atmospheric ^{222}Rn.

Although ^{222}Rn is a widespread atmospheric tracer in climate, air quality and pollution studies, continuous ^{222}Rn monitoring at low concentrations, as found in the atmosphere, is more challenging than monitoring its gamma emitting daughters ^{214}Pb and ^{214}Bi (Barbosa et al., 2017). Since scavenging processes responsible for the attachment of ^{222}Rn daughters to rain droplets are much more efficient in-cloud instead of below-cloud (Greenfield et al., 2008), measuring gamma radiation from ^{222}Rn progeny can be a simple alternative to the direct measurement of ^{222}Rn concentration in the clouds. Meteorology can highly benefit from continuous and spatially distributed measurements of ^{214}Pb and ^{214}Bi gamma activity. Enhanced gamma-ray dose rates due to wet deposited ^{222}Rn progeny can provide powerful insights into air mass origin and regional characteristics of precipitations. Indeed, it has been shown that a cloud with marine or continental origin is usually characterized by a ^{222}Rn concentration respectively lower and higher than the average concentration (Inomata et al., 2007; Mercier et al., 2009; Paatero, 2000). Furthermore, since in precipitation water the ^{214}Pb/^{214}Bi activity ratio evolves in time according only to the half-lives of the two radionuclides, its measurement enables the determination of rain and snow age (Greenfield et al., 2008) and can shed light into advection and diffusion processes (Shapiro and Forbes-Resha, 1975).

In this work I present the results of a proximal gamma-ray spectroscopy experiment aimed at studying the ^{214}Pb gamma activity temporal profile in relation to rainfall events. The experiment was performed by installing in an agricultural test field an agrometerological station, equipped with a traditional bucket rain gauge, and a custom gamma spectroscopy station, constituted by a 1L sodium iodide (NaI) scintillator, which simultaneously detected gamma radiation emitted in the ground and in the atmosphere.

Meteorological and radiometric data were continuously acquired for 7 months and temporally aligned. I performed the data analysis in order to develop a theoretical model able to reproduce the observed plateau, peak and exponential decay phases of the rain-induced ^{214}Pb gamma activity temporal profile. The effectiveness of the model is demonstrated by the good agreement observed between measured and estimated ^{214}Pb count rates (with χ^2 always < 2.9 for every rain episode) (Bottardi et al., 2020).

2.1 Materials and Methods

2.1.1 Experimental site and setup

The experiment was performed in the period 4 April - 2 November 2017 in a 40 × 108 m^2 agricultural test field of the research centre of the Emiliano-Romagnolo Canal (CER) irrigation district in the Emilia Romagna region, Italy.

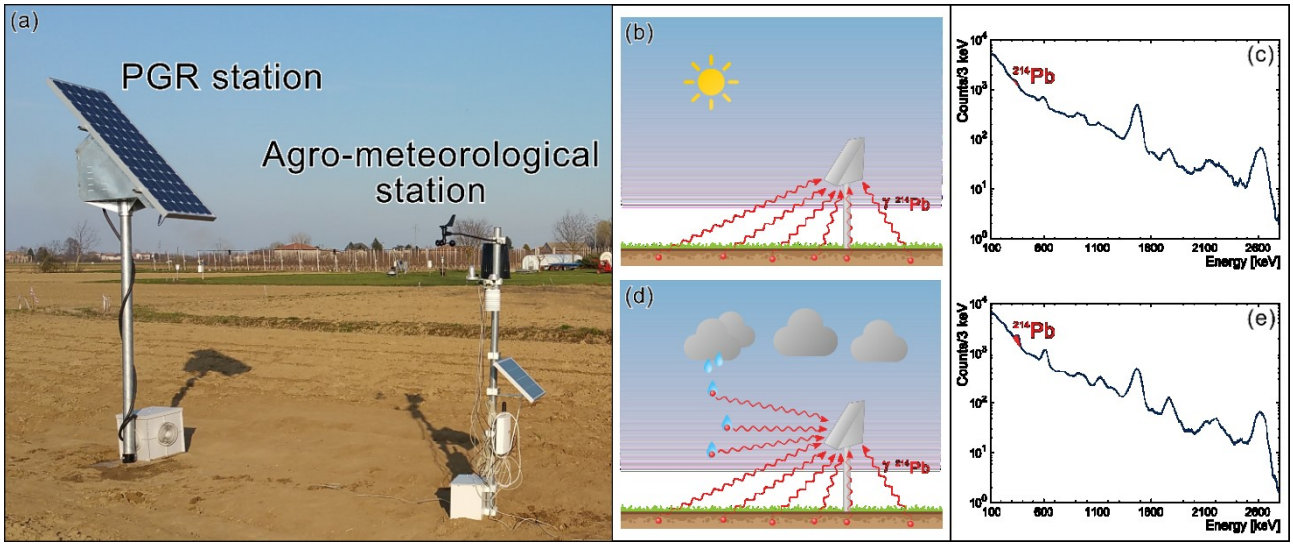

Figure 2.1. Panel (a): Proximal Gamma-Ray (PGR) spectroscopy station, equipped with a 1L NaI(Tl) detector, and agro-meteorological station installed at the test field located in the Emiliano-Romagnolo Canal irrigation district in Emilia Romagna, Italy (44.57° N, 11.53° E, 16 m above sea level). Panels (b) to (e) illustrate the rationale at the basis of rain-induced ^{214}Pb activity measurements through proximal gamma-ray spectroscopy. In absence of rain the detector receives gamma radiation produced in the decay of ^{214}Pb distributed in the soil (panel b) and measures a gamma spectrum (panel c) characterized by a net area in the main ^{214}Pb photopeak (in red) proportional to the ^{214}Pb ground abundance. When it rains, ^{214}Pb atoms in the clouds attach to rain drops (panel d) which, by falling off, generate a rain-induced increase of the ^{214}Pb gamma activity at ground level, experimentally observed as an increase in the ^{214}Pb photopeak net area (panel e).

The experimental setup (Figure 2.1a) consisted of an agro-meteorological station (MeteoSense 2.0, Netsens) and a custom Proximal Gamma-Ray (PGR) spectroscopy station. The agro-meteorological station measured air temperature [°C], relative air humidity $[\%]$, wind direction $[m\ s^{-1}]$, and rainfall amounts $[mm]$. The PGR station comprised a 1L NaI(Tl) scintillator providing a continuous log of individual energy depositions and corresponding detection times. By placing the detector at a 2.25 m height, PGR spectroscopy provided soil moisture measurements with a ~25 m footprint radius (Baldoncini et al., 2018a; Strati et al., 2018). Thanks to the installation of a solar panel and a GPRS antenna, both stations were self-powered and web connected. Dedicated software was developed to remotely pre-process the data for synchronizing meteorological and radiometric observations in a unique time-referenced dataset having a 0.25 hours temporal resolution.

As ^{40}K, ^{238}U and ^{232}Th amounts in the soil are constant, temporal variations in measured gamma spectra can be ascribed to: i) changes in soil and biomass water content, extensively studied in (Baldoncini et al., 2019), ii) changes in atmospheric ^{222}Rn, iii) changes in cosmic radiation levels and iv) rain-induced gamma activity, which can be traced by monitoring the ^{214}Pb net photopeak count rate. In absence of rain the net number of events recorded in the ^{214}Pb photopeak area is attributable to gamma radiation emitted

in the decay of ^{214}Pb distributed in the soil (Figure 2.1b and Figure 2.1c). In presence of rainfall ^{214}Pb radionuclides brought to ground by rain drops increase the ^{214}Pb gamma activity at ground level, leading to an increase of the ^{214}Pb photopeak net area (Figure 2.1d and Figure 2.1e).

The experimental setup and conditions were specifically tailored for gathering reliable and unbiased estimates of the ^{214}Pb activity at ground level and for studying its time series in relation to rainfall episodes. The CER research centre has been identified as an ideal site for hosting the experiment since irrigation amounts were carefully monitored and daily logged. The PGR station provided continuous measurements over a 7 months data-taking period with a 94.8% duty cycle overlapping with synchronized agro-meteorological acquisitions, including rainfall amount data relevant for this study. The 1L detector volume allowed for recording good counting statistics with a sampling frequency adequate for modelling the plateau, peak and exponential decay phases of the rain-induced ^{214}Pb gamma activity temporal dynamics (see Table 2.2 and Figure 2.5). Despite cosmic radiation can be subject to day-night and seasonal variations, it gives rise to a smooth gamma spectral shape (Baldoncini et al., 2018b) having no peaks interfering with the estimation of ^{214}Pb net photopeak count rates. The attenuation effect on the gamma radiation due to the aluminium box surrounding the NaI(Tl) detector is constant over time and does not affect ^{214}Pb activity measurements. Moreover, potential spectral gain variations due to temperature fluctuations were taken into account by energy calibrating each 0.25 hours gamma-ray spectrum in order to properly integrate net count rates in the ^{214}Pb photopeak energy window. Measurement conditions were stable and under control during the entire data-taking period as there were no potential anthropic interferences, no surrounding tall trees affecting rainfall estimations and both stations were installed in a homogeneous and morphologically flat terrain. Finally, attention was paid in placing the bucket rain gauge of the agro-meteorological station far enough from the two solar panels to avoid rainfall interception and consequently biased rain amount measurements.

2.1.2 Rain-induced gamma activity measurements

In the clouds, ^{222}Rn and its progenies are considered in secular equilibrium, but when rain droplets begin their descent to ground the equilibrium is broken (Figure 2.3). Although ^{222}Rn itself is chemically inert, its decay products (Figure 2.2) are mainly formed and are likely to remain in a positive charged state. They can attach to existing aerosol particles and droplets, falling to the ground with rain (Hopke and chemistry, 1996; Porstendörfer, 1994). This is what makes monitoring the activities of gamma emitting ^{222}Rn progeny extremely responsive to rainfall events (Barbosa et al., 2017).

This work focuses on the reconstruction of the gamma signal generated by ^{214}Pb, which has a half-life of 26.8 minutes (comparable to rain events time-scales) and which activity has been already monitored in previous studies in relation to rain events (Inomata et al., 2007; Livesay et al., 2014; Mercier et al., 2009).

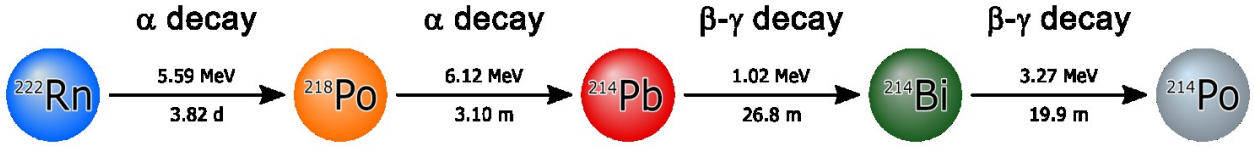

Figure 2.2. ^{238}U decay sub-chain from ^{222}Rn to ^{214}Po, simplified by excluding the decay channels with branching fractions $< 0.05\%$. The simplified sub-chain comprises 2 α decays and 2 β-γ decays. Each α or β-γ decay is represented with a horizontal arrow: the Q-value and the half-life of the father nucleus of a given decay are reported respectively above and below the corresponding arrow. The β-γ decay of interest for the rain-induced gamma activity measurements presented in this work is the one transforming ^{214}Pb into ^{214}Bi. In this decay the most intense gamma rays are those with characteristic energies of $295\ keV$ and $352\ keV$, the latter chosen for the estimation of the experimental ^{214}Pb net photopeak count rate.

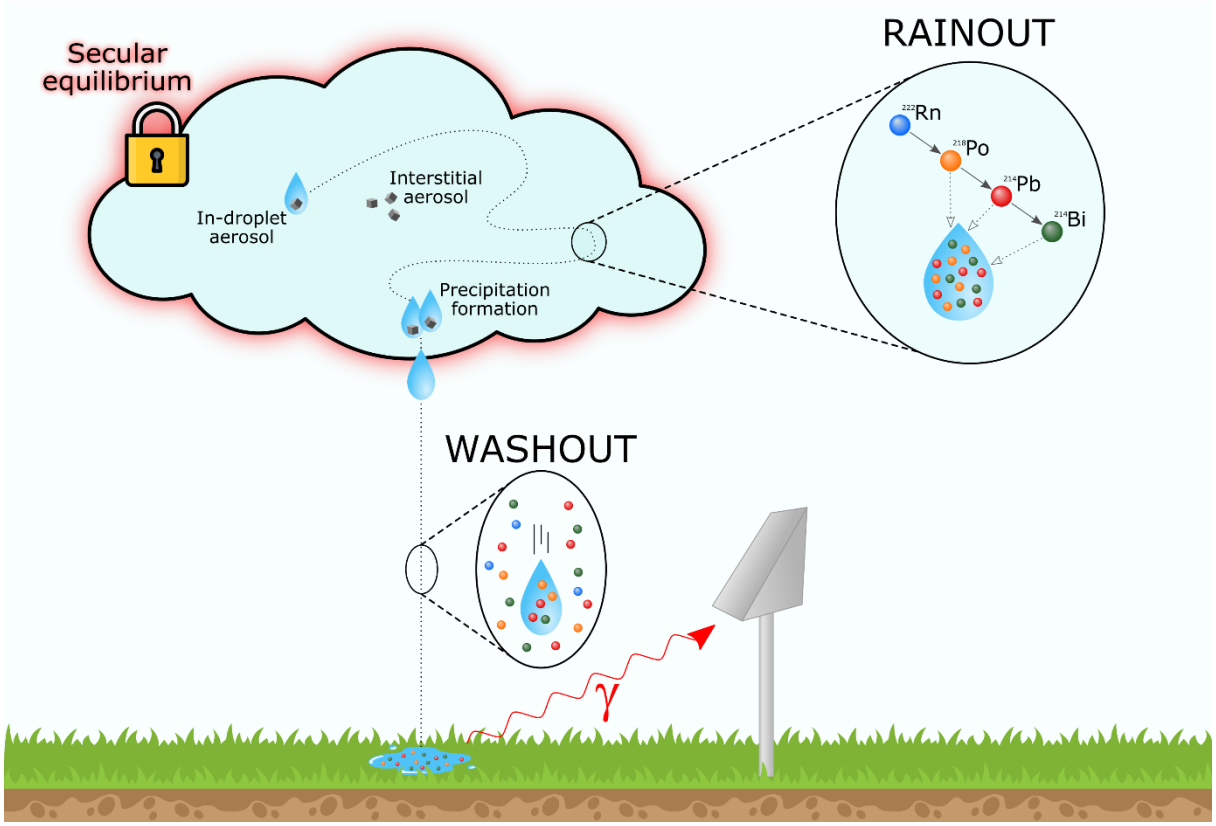

Figure 2.3. Scheme of the rainout and washout radioactivity charge mechanisms of raindrops. When in-cloud ^{222}Rn undergoes α-decay, its daughter products ^{218}Po, ^{214}Pb and ^{214}Bi are mainly formed in a positive charged state. Due to their high reactivity, they attach to in-cloud aerosol particles which in turn bind to growing droplets, making rainwater charged in radioactivity. In this in-cloud rain out scavenging process ^{222}Rn and its daughters are considered in secular equilibrium. The washout process is instead a below cloud scavenging process in which atmospheric ^{222}Rn progenies attach themselves to falling rain drops. This mechanism is typically much less efficient in radioactivity scavenging and is considered negligible in this work. After water droplets reach the ground surface, the gamma signal produced in the decay of ^{214}Pb brought to ground by rainfall can be detected by the PGR station.

Over the 190 days of effective data-taking in the period 4 April – 2 November 2017, it rained in 45 days. The maximum measured rain rate was $64\ mm\ h^{-1}$, while the minimum corresponds to the bucket rain gauge sensitivity of $1\ mm\ h^{-1}$ (Figure 2.4).

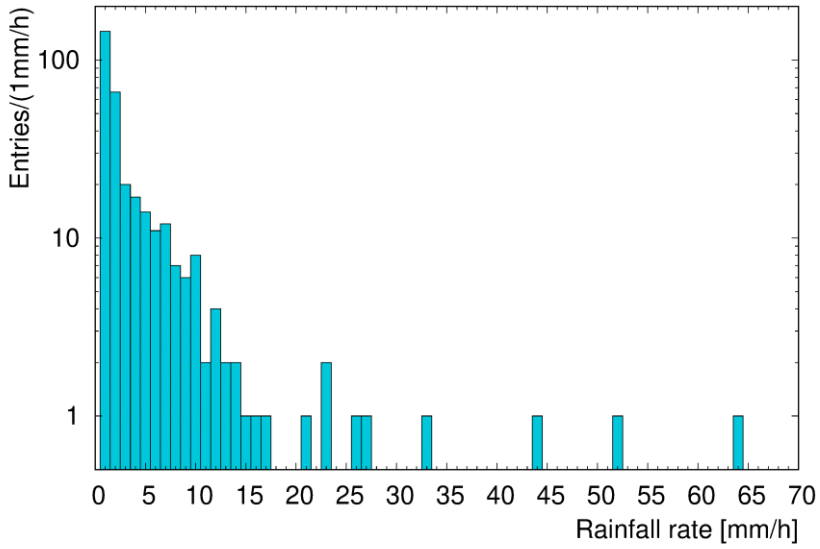

Figure 2.4. Histogram of the occurrences of rainfall rates recorded during the proximal gamma-ray spectroscopy experiment (4 April – 2 November 2017) performed at the agricultural test field of the Emiliano-Romagnolo Canal irrigation district in Emilia Romagna, Italy (44.57° N, 11.53° E, $16\ m$ above sea level). Each rainfall rate value was estimated from rainfall amounts measured over a $0.25\ h$ sampling time by the bucket rain gauge installed on the agro-meteorological station. The minimum measured rain rate is $1\ mm\ h^{-1}$, corresponding to the rain gauge sensitivity.

According to the selection criteria presented in Section 2.2, we identify 12 rain episodes (Table 2.1) subdivided in 82 measurements of $0.25\ h$ each. The minimum and maximum rain duration were respectively $45\ min$ and $3\ h$ and $45\ min$, the minimum and maximum average rainfall rates were respectively $2.9\ mm\ h^{-1}$ and $13.0\ mm\ h^{-1}$, and the minimum and maximum amount of precipitated water in a single episode were respectively $3.8\ mm$ and $23.5\ mm$.

Table 2.1. Main features of the chosen 12 rain episodes, listed in chronological order. Rain episodes were identified by analyzing rainfall data acquired by the bucket rain gauge, characterized by a $0.25\ h$ temporal resolution, and by applying the selection criteria discussed at the beginning of Section 2.2. In the column 3, 4 and 5 are presented the start, end time and duration referred to the episode period called P2 (see Section 2.1.3 for the definition). The total precipitation of each episode was estimated by summing individual precipitation amounts recorded over the episode duration. The mean rain rate of each episode was evaluated by dividing the total precipitation amount by the corresponding P2 duration.

N. episode	Date [DD/MM/YYYY]	P2 Start Time [hh:mm]	P2 End Time [hh:mm]	P2 Duration [hh:mm]	Precipitation [mm]	Rate [mm/h]
1	16/04/2017	23:15	02:00	2:45	8.0	2.9
2	27/04/2017	21:15	23:30	2:15	7.8	3.4
3	04/05/2017	23:00	23:45	0:45	6.3	8.3
4	25/06/2017	13:30	14:15	0:45	3.8	5.0
5	28/06/2017	18:45	20:15	1:30	15.3	10.2
6	11/07/2017	15:00	18:15	3:15	23.5	7.2
7	06/08/2017	18:30	20:15	1:45	18.3	10.4
8	10/08/2017	13:45	14:45	1:00	13.0	13.0
9	02/09/2017	22:15	23:00	0:45	3.8	5.0
10	07/09/2017	23:00	0:45	1:45	5.5	3.1
11	24/09/2017	12:30	13:45	1:15	9.0	7.2
12	06/10/2017	16:45	20:30	3:45	19.0	5.1

Table 2.2 reports the ^{214}Pb counting statistics for the 12 rain episodes. For each $0.25\ h$ temporal bin, individual ^{214}Pb gross count rates were obtained by integrating all events recorded in the $(320 - 380)\ keV$ photopeak energy window corresponding to the $352\ keV$ gamma emission line. The net ^{214}Pb photopeak area determination was performed according to the trapezoid method described in Section 5.4.1 of (Gilmore, 2008), where a fixed value of 3.5 was adopted for the m parameter, i.e. the mean number of channels on each side of the peak region used to estimate the linear background beneath the peak. Following the approach described in Section 2.1.3, the ^{214}Pb background count rate before and after the rain time were calculated respectively over period P1 and P4 for each rain episode (see also Figure 2.5 and Figure 2.8). They are a baseline representing the ^{214}Pb gamma signal associated to the soil source and to a mean atmospheric ^{222}Rn concentration, which is typically affected by a daily modulation (Figure 2.6).

Table 2.2. Gross and net counting statistics in the $(320 - 380)\ keV$ ^{214}Pb photopeak energy window before, during and after the period P2 for the 12 rain episodes, listed in chronological order. The mean ^{214}Pb gross and net background count rates before (after) the rain period, together with their uncertainty, were estimated as the average and standard deviation of individual count rates measured in each of the 20 $0.25\ h$ temporal bins of period P1 (P4). The max gross and net ^{214}Pb count rates referred to the rain period represent the maximum gross and net values recorded in period P2+P3. By assuming a Poissonian counting distribution, the uncertainty on the maximum gross count rate in the rain period was estimated as the square root of the gross counts divided by the width of the temporal bin. The uncertainty on the maximum net counts was obtained by combining the Poissonian uncertainty with the uncertainty associated to the background estimation, adapted from Equation 5.42 of (Gilmore, 2008). For the definitions of periods P1, P2, P3 and P4 see Section 2.1.3 and Figure 2.8.

	Background before rain period (Period 1)		**Rain period (Period 2 + Period 3)**		**Background after rain period (Period 4)**	
N. episode	**Mean gross [cps]**	**Mean net [cps]**	**Max gross [cps]**	**Max net [cps]**	**Mean gross [cps]**	**Mean net [cps]**
1	32.0 ± 0.5	1.3 ± 0.2	46.0 ± 0.2	4.5 ± 0.3	31.1 ± 0.7	1.1 ± 0.2
2	31.0 ± 0.6	1.1 ± 0.2	43.8 ± 0.2	4.9 ± 0.3	30.3 ± 0.5	1.0 ± 0.2
3	31.4 ± 0.7	1.1 ± 0.2	41.2 ± 0.2	4.0 ± 0.2	31.3 ± 0.8	1.1 ± 0.2
4	32.1 ± 0.6	1.2 ± 0.3	49.7 ± 0.2	6.2 ± 0.3	31.3 ± 0.5	1.0 ± 0.2
5	30.7 ± 0.7	1.0 ± 0.3	53.6 ± 0.2	5.6 ± 0.3	29.9 ± 0.5	1.1 ± 0.2
6	29.6 ± 0.6	0.8 ± 0.2	62.0 ± 0.3	7.5 ± 0.3	29.4 ± 0.6	1.0 ± 0.3
7	32.8 ± 1.4	1.4 ± 0.3	73.6 ± 0.3	7.3 ± 0.3	30.2 ± 0.5	1.0 ± 0.2
8	32.0 ± 0.7	1.1 ± 0.2	44.3 ± 0.2	3.9 ± 0.3	28.4 ± 0.6	0.8 ± 0.3
9	32.9 ± 1.6	1.4 ± 0.4	48.7 ± 0.2	4.5 ± 0.3	31.1 ± 0.6	1.0 ± 0.3
10	31.4 ± 0.8	1.0 ± 0.2	50.3 ± 0.2	5.5 ± 0.3	31.1 ± 0.6	0.9 ± 0.2
11	34.4 ± 1.1	1.5 ± 0.3	50.5 ± 0.2	4.3 ± 0.3	31.3 ± 0.5	1.1 ± 0.3
12	34.1 ± 0.8	1.3 ± 0.2	69.2 ± 0.3	6.2 ± 0.3	31.9 ± 0.5	1.1 ± 0.2

The time-series of the ^{214}Pb net count rates during each rain episode together with the predictions of the model presented in Section 2.1.3 are plotted in Figure 5. As expected, measurements performed with the PGR station are extremely sensitive to rain water but insensitive to irrigation water (Figure 5, Episode 6). Indeed, contrary to rain droplets, irrigation water does not collect ^{222}Rn daughters and therefore is not responsible for any increase in the ^{214}Pb count rate.

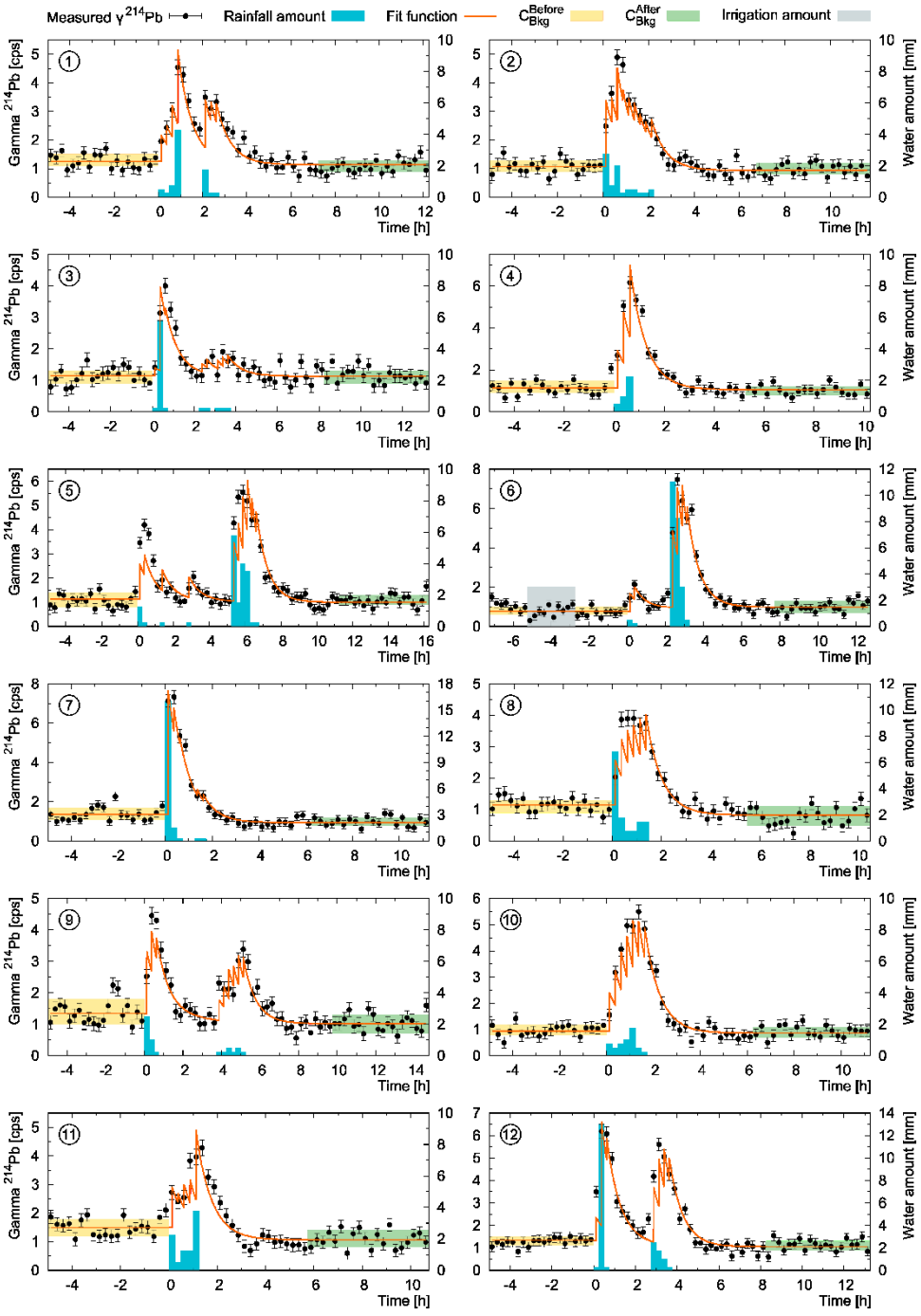

Figure 2.5. Time-series of the ^{214}Pb net count rates for the 12 rain episodes. For each episode, black dots correspond to the net count rates measured in the $(320 - 380\ keV)$ ^{214}Pb photopeak energy window, together with their uncertainties. The orange line corresponds to the predictions provided by the model described in Section 2.1.3. The yellow (green) bands are the 1σ-interval of the average net count rates estimated in periods P1 (P4) (see also Table 2.2 and Figure 2.8). Blue and grey bars report the amount of rainfall and irrigation water, respectively. Episode 6 shows an irrigation event which, as expected, does not produce any increase in the ^{214}Pb net count rate. Episodes 3, 5 and 9 comprise periods characterized by a rain amount of few mm precipitated after (episodes 3 and 9) or before (episode 5) the main rain episode. Since these periods did not satisfy the rain episode selection criteria reported in Section 2.2, they are excluded from the mean rainfall rate and duration calculation (see also Table 2.1) but are taken into account for the ^{214}Pb net count rate time series reconstruction.

2.1.3 Modelling the rain-induced gamma activity

The model developed for reconstructing the ^{214}Pb gamma activity time series at ground level as function of the rainfall rate is based on the following assumptions.

- The increase of ^{214}Pb gamma activity at ground level is only due to the decay of ^{214}Pb attached to rain drops.
- The temporal evolution of the ^{214}Pb rain induced-gamma activity depends only on the rainfall rate. This derives from the assumption that only the in-cloud activity accretion processes generate the ground-level ^{214}Pb activity increase. An explicit temporal component would have been introduced by including a below-cloud scavenging process, which has however a negligible ^{214}Pb collection efficiency with respect to in-cloud processes (Greenfield et al., 2008).
- The ^{214}Pb net background count rate (describing the not rain-induced gamma activity) before and after the rain time are in principle different. This is reasonable since precipitated water pours into the soil, attenuating the signal produced by ^{214}Pb present in the ground.

The ^{214}Pb net count rate exhibits a day-night fluctuation (Greenfield et al., 2002; Sturrock et al., 2018) with a period of $(1.0 \pm 0.1)\ days$ (Figure 2.6). A minimum count rate of $(0.4 \pm 0.1)\ cps$ and a maximum count rate of $(2.0 \pm 0.4)\ cps$ are typically recorded in the evening and in the morning, respectively, corresponding to an average linear count rate variation of $0.13\ cps\ h^{-1}$. Considering that the mean standard deviation characterizing a single ^{214}Pb net count rate measurement is $0.22\ cps$, a background count rate linear variation corresponding to 3 standard deviations ($0.66\ cps$) would be registered in $5\ h$. This argument justifies the adoption of a $5\ h$ reference time for the estimation of the average ^{214}Pb background net count rates before and after the beginning and the end of the rain. A further investigation of these fluctuations could shed light on possible sources of signal periodical increase/decrease related for instance to cosmic radiation, radon day-night average concentrations, variations in day-night top-soil moisture levels.

The model exposed in this section can be used for analysing ^{214}Pb gamma signal in any rain episode. Given a rain event (i.e. non-zero rainfall amount) separated from the previous one by at least $9.5\ h$, a rain episode is defined as four consecutive time Periods (P) (Figure 2.8) described as follows:

- P1: this Period covers the $5\ h$ before the beginning of the rainfall and permits the estimation of the ^{214}Pb background net count rate C_{Bkg}^{Before};
- P2: this Period starts and ends respectively at the first and last temporal bins for which a non-zero rainfall amount is measured. Note that this Period can include more rain events separated by no rainfall time intervals (e.g. Episode 1 in Figure 2.5) shorter than $9.5\ h$;
- P3: this Period follows the end of P2 for a duration of $4.5\ h$, corresponding to ~ 10 ^{214}Pb half-lives, necessary to let the ^{214}Pb net count rate exponentially decrease to the after-rain background value C_{Bkg}^{After};
- P4: this Period covers the $5\ h$ after the end of P3 and permits to estimate the ^{214}Pb background net count rate C_{Bkg}^{After}.

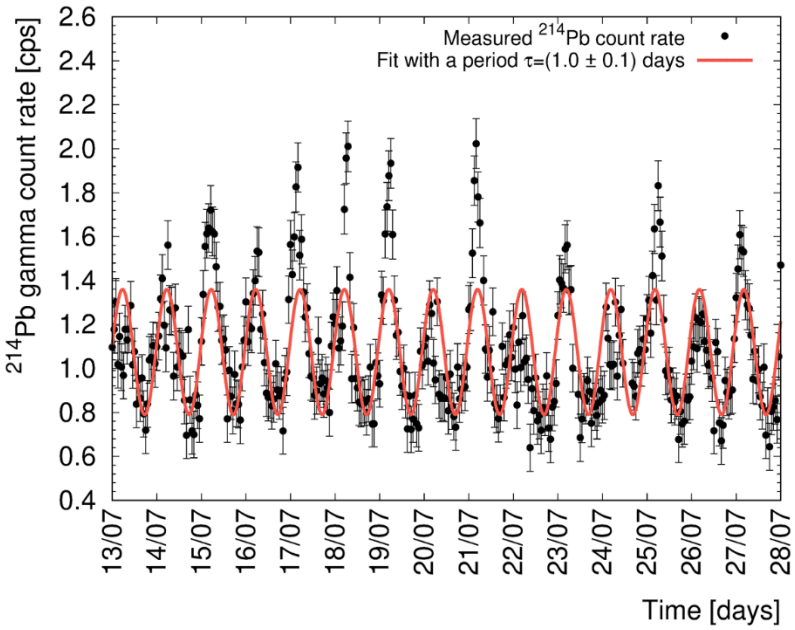

Figure 2.6. ^{214}Pb net count rate measured with 1 h temporal resolution in absence of irrigation and rainfall over a continuous period of 15 days. Measured ^{214}Pb net count rates (black dots) exhibit a daily periodical variation with minima ($\sim 0.4\ cps$) and maxima ($\sim 2.0\ cps$) typically recorded in the evening ($\sim 5{:}30\ PM$) and in the morning ($\sim 5{:}30\ AM$), respectively. The statistical uncertainty on each data point derives from an adaptation of Equation 5.42 of (Gilmore, 2008). The red line represents the best fit sinusoidal function modelled as $a \cdot \sin\left(\frac{2\pi \cdot t}{\tau} + b\right) + c$ with best fit parameters $a = (0.28 \pm 0.01)\ [cps]$, $\tau = (1.0 \pm 0.1)\ [days]$, $b = (0.12 \pm 0.06)$ and $c = (1.08 \pm 0.01)\ [cps]$.

With the purpose of describing the gamma ^{214}Pb net count rate time series during a rain episode, two signal components have to be taken into account: i) the rain induced source term and ii) the ^{214}Pb radioactive decay term. The source term in the ^{214}Pb Bateman equation due to the ^{218}Po decay is neglected since its half-life ($3.1\ min$) is sufficiently short that it will have decayed to 0.01% of its initial activity by the precipitation age ($\sim 30\ min$), i.e. the average time between the removal of ^{222}Rn progeny from secular equilibrium by rain and the deposition of ^{222}Rn progeny to the ground (Greenfield et al., 2008).

The variation in time of the number of ^{214}Pb nuclei $N_{Pb}(t)$ per unit of surface dS can be written as:

$$\frac{dN_{Pb}(t)}{dS \cdot dt} = + \frac{dN_{Pb}^{Rain}(t)}{dS \cdot dt} - \lambda_{Pb} \cdot \frac{dN_{Pb}(t)}{dS} \tag{2.1}$$

where dN_{Pb}^{Rain} is the increase in ^{214}Pb nuclei associated to the rain deposition and $\lambda_{Pb} = {}^{1}/_{\tau_{Pb}} = 4.28 \cdot 10^{-4}\ s^{-1} = 1.54\ h^{-1}$ is the ^{214}Pb decay constant which rules the exponential decay. The rain-induced source term $\frac{dN_{Pb}^{Rain}}{dS \cdot dt}$ can be described as a function of the rain rate R $\left[\frac{mm}{h}\right]$:

$$\frac{dN_{Pb}^{Rain}(t)}{dS \cdot dt} = n \cdot v_{term} \cdot N_{Pb}^{Drop} = \frac{R}{V_G} \cdot N_{Pb}^{Drop} \tag{2.2}$$

where $n\left[\frac{drops}{m^3}\right]$ is the number density at ground level of raindrops having identical size, $N_{Pb}^{Drop}\left[\frac{Pb\ nuclei}{drop}\right]$ is the number of ^{214}Pb nuclei in a raindrop having volume $V_G[m^3]$and $v_{term}\ [m\ s^{-1}]$ is the raindrop terminal velocity. Since in principle N_{Pb}^{Drop} can depend on the rain rate R, the rain induced source term is not expected to linearly scale with R but can be parameterized as a power law of the rain rate R with exponent d:

$$\frac{dN_{Pb}^{Rain}(t)}{dS \cdot dt} \sim R^d \tag{2.3}$$

As the efficiency and the geometric acceptance of the PGR station do not change over time, the footprint area of proximal gamma-ray spectroscopy measurement with a $\sim 25\ m$ radius can be considered constant. Consequently, the gamma count rate increase $\Delta C\ [cps]$ recorded in a time interval $\Delta T\ [h]$ is directly proportional to the number of ^{214}Pb nuclei accumulated to the ground during the same time:

$$\frac{\Delta N_{Pb}^{Rain}}{\Delta T} \propto \frac{\Delta C}{\Delta T} = A \cdot R^d \tag{2.4}$$

where $A\left[\frac{cps}{mm^d} h^{1-d}\right]$ is a proportionality factor that depends on the response of the 1L NaI(Tl) detector installed in the PGR station and on in-cloud ^{222}Rn concentration.

This theoretical background can be formulated also in terms of activity density $G[cps\ mm^{-1}]$, corresponding to the ^{214}Pb gamma activity in a rainwater layer of thickness $\Delta z\ [mm]$, accumulated on the ground in a time interval ΔT by a rainfall of rate R,

$$\frac{1}{R}\frac{\Delta C}{\Delta T} = \frac{\Delta C}{\Delta z} = G = A \cdot R^{d-1} \begin{cases} if\ 0 < d < 1 \rightarrow G\ is\ inversely\ correlated\ with\ R \\ if\ d = 1 \rightarrow G\ is\ independent\ from\ R \\ if\ d > 1 \rightarrow G\ is\ positively\ correlated\ with\ R \end{cases} \tag{2.5}$$

For a single rain event with duration $\Delta T = t_2 - t_1 = 0.25\ h$, corresponding to the experimental temporal resolution, it is assumed that the rain has fallen instantaneously to ground at $t = t_1 + \frac{0.25\ h}{2}$. At $t < t_1 + \frac{0.25\ h}{2}$ the ^{214}Pb net count rate $C(t)[cps]$ is expected to be equal to the background count rate before the rain event C_{Bkg}^{Before}. At the beginning of the rain event at $t = t_1 + \frac{0.25\ h}{2}$, $C(t)$ has a sharp increase due to the rain-induced activity source term ΔC. At $t > t_2$ $C(t)$ is then expected to asymptotically approach the after-rain background value C_{Bkg}^{After}. The temporal evolution of the ^{214}Pb net count rate $C(t)$ shown in Figure 2.7 can therefore be written as:

$$\begin{cases} C(t) = C_{Bkg}^{Before} & with\ t < t_1 + \dfrac{0.25\ h}{2} \\ C(t) = \Delta C \cdot e^{-\lambda_{Pb}\left[t - \left(t_1 + \frac{0.25\ h}{2}\right)\right]} + C_{Bkg}\ (t) & with\ t_1 + \dfrac{0.25\ h}{2} \le t < t_2 + \dfrac{0.25\ h}{2} \\ C(t) = \Delta C \cdot e^{-\lambda_{Pb}\left[t - \left(t_1 + \frac{0.25\ h}{2}\right)\right]} + C_{Bkg}^{After} & with\ t \ge t_2 + \dfrac{0.25\ h}{2} \end{cases} \tag{2.6}$$

where $\Delta C\ [cps] = \Delta T \cdot A \cdot R^d$ is the impulsive count rate increase associated to the single rainfall deposition.

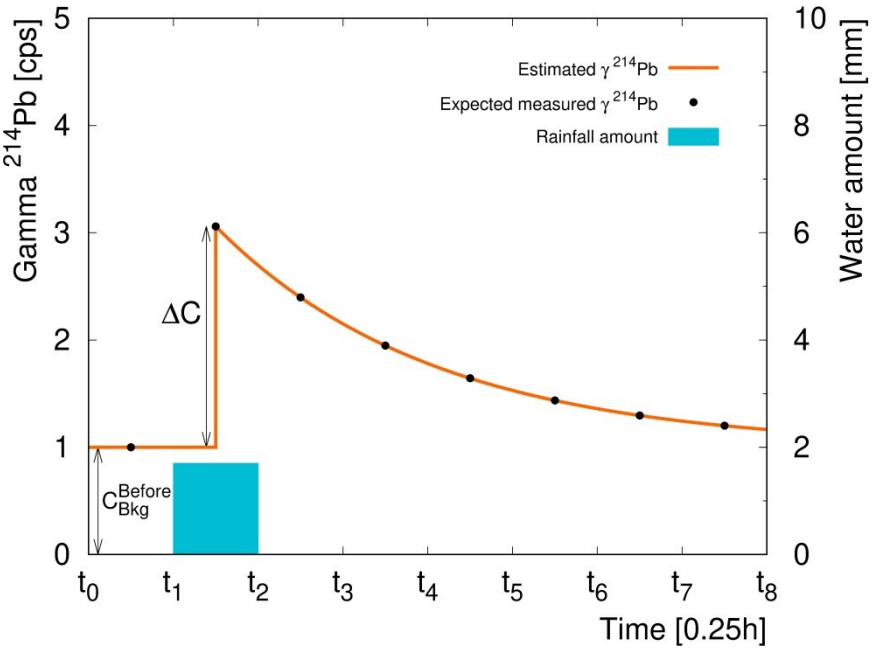

Figure 2.7. Example of the ^{214}Pb net count rate time series during a rain episode having a single rain event of 0.25 h duration, corresponding to the experimental temporal resolution of synchronized radiometric and rainfall data. Black dots simulate the measured ^{214}Pb net count rates. The orange line represents the ^{214}Pb net count rates predicted by the model described in Section 2.1.3 for an amount of precipitated water reported with a blue bar. At $t < t_1 + \frac{0.25\ h}{2}$ the ^{214}Pb net count rate is equal to the background value estimated before the rain event C_{Bkg}^{Before}. When the rain starts at $t = t_1 + \frac{0.25\ h}{2}$ the rain-induced gamma activity originates an impulsive count rate increase ΔC making the ^{214}Pb net count rate sharply rise to $C_{Bkg}^{Before} + \Delta C$. When rainfall stops the ^{214}Pb net count rate follows an exponential decrease ruled by the ^{214}Pb decay constant till it reaches the after-rain background asymptotic value C_{Bkg}^{After}.

In order to develop a theory adequate for describing an episode whose rain lasts for n temporal bins with width ΔT, characterized by R_i rain rates, ΔC_i impulsive count rate increases have to be introduced, with:

$$\Delta C_i = \Delta T \cdot A \cdot {R_i}^d, 1 \leq i \leq n \tag{2.7}$$

Under the assumption of constant radon (and radon progenies) concentration in clouds during a given rain episode, the A scaling factor and the exponent d are assumed to be constant during the episode duration, but they are allowed to vary from one rain episode to another.

Considering that the ^{214}Pb background net count rates before (C_{Bkg}^{Before}) and after (C_{Bkg}^{After}) are not necessarily equal, a time dependent background $C_{Bkg}(t)$ in period P2 is evaluated on the basis of a linear trend describing the transition from C_{Bkg}^{Before} to C_{Bkg}^{After} (Figure 2.8). Consequently, the ^{214}Pb net count rate time series can be mathematically described by the equations in Table 2.3.

Table 2.3. Scheme of the mathematical process used for reconstructing the ^{214}Pb net count rate time series during a rain episode. Every interval of time corresponds to a period P of the episode described in the beginning of Section 2.3. The equations in the third column are used sequentially for fitting the count rate $C(t)$ as function of time t (in hours) for getting the impulsive count rate increase (ΔC) and the background (C_{Bkg}), knowing λ_{Pb}.

Period	Interval of time	Equations
P1	$t < t_1 + \frac{0.25\ h}{2}$	$C(t) = C_{Bkg}^{Before}$
P2	$t_1 + \frac{0.25\ h}{2} \leq t < t_2 + \frac{0.25\ h}{2}$	$C(t) = \Delta C_1 e^{-\lambda_{Pb}\left[t-\left(t_1+\frac{0.25\ h}{2}\right)\right]} + C_{Bkg}(t)$
	$t_i + \frac{0.25\ h}{2} \leq t < t_{i+1} + \frac{0.25\ h}{2}$	$C(t) = \Delta C_1 e^{-\lambda_{Pb}\left[t-\left(t_1+\frac{0.25\ h}{2}\right)\right]} + \ldots + \Delta C_i e^{-\lambda_{Pb}\left[t-\left(t_i+\frac{0.25\ h}{2}\right)\right]} + C_{Bkg}(t)$
	$t_n + \frac{0.25\ h}{2} \leq t < t_{n+1} + \frac{0.25\ h}{2}$	$C(t) = \Delta C_1 e^{-\lambda_{Pb}\left[t-\left(t_1+\frac{0.25\ h}{2}\right)\right]} + \ldots + \Delta C_n e^{-\lambda_{Pb}\left[t-\left(t_n+\frac{0.25\ h}{2}\right)\right]} + C_{Bkg}(t)$
P3	$t_{n+1} + \frac{0.25\ h}{2} \leq t < t_{n+1} + 4.5\ h$	$C(t) = \Delta C_1 e^{-\lambda_{Pb}\left[t-\left(t_1+\frac{0.25\ h}{2}\right)\right]} + \cdots + \Delta C_n e^{-\lambda_{Pb}\left[t-\left(t_n+\frac{0.25\ h}{2}\right)\right]} + C_{Bkg}^{After}$
P4	$t \geq t_{n+1} + 4.5\ h$	$C(t) = C_{Bkg}^{After}$

with ΔC_i depending on the parameters (A, d) as reported in Eq. (2.7). As an example, Figure 2.8 shows the modelling of the ^{214}Pb net count rate $C(t)$ for a rain episode with a P2 lasting $0.5\ h$.

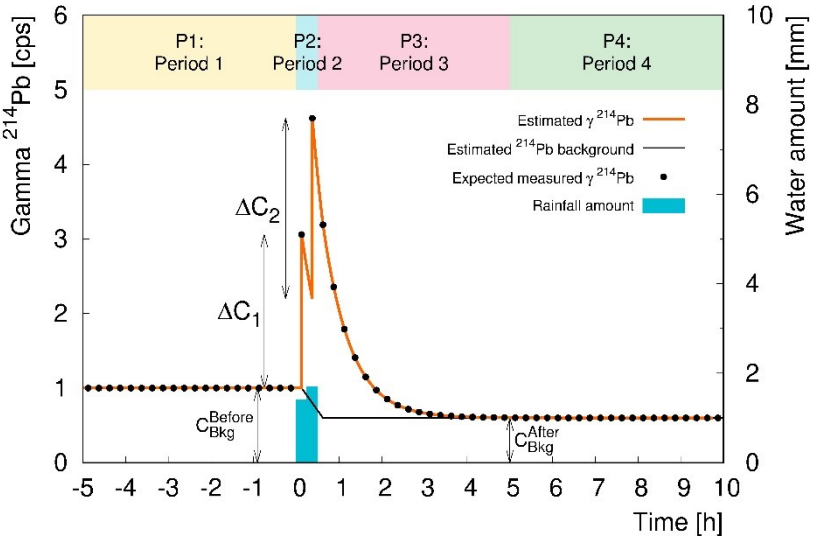

Figure 2.8. Example of the ^{214}Pb net count rate time series during a single rain event of 0.50 h duration, corresponding to twice the experimental temporal resolution of synchronized radiometric and rainfall data. Black dots simulate the measured ^{214}Pb net count rates. The orange line represents the ^{214}Pb net count rates predicted by the model described in Section 2.1.3 for an amount of precipitated water reported with a blue bar. At $t < \frac{0.25\ h}{2}$ the ^{214}Pb net count rate is equal to C_{Bkg}^{Before}, corresponding to the before rain background value estimated over P1 (see also beginning of Section 2.1.3). In the rain time P2 the rainfall amounts precipitated during the first temporal bin at $t = \frac{0.25\ h}{2}$ and second temporal bin at $t = 0.25\ h + \frac{0.25\ h}{2}$ originate an impulsive count rate increase respectively equal to ΔC_1 and ΔC_2. When the rain stops, the ^{214}Pb net count rate exponentially decreases over P3 till it reaches the after rain background asymptotic value C_{Bkg}^{After}, estimated over P4. The black line describes the temporal evolution of the ^{214}Pb background net count rate: it assumes the C_{Bkg}^{Before} and C_{Bkg}^{After} constant values respectively in P1 and P3+P4 and a temporal dependent value during P2 estimated from a linear regression describing the transition from C_{Bkg}^{Before} to C_{Bkg}^{After}.

The model was applied against radiometric data measured for each of the 12 rain episodes (Figure 2.5) in order to reconstruct the experimental ^{214}Pb net count rate series and to estimate the best fit values

of four free parameters: A, d, C_{Bkg}^{Before} and C_{Bkg}^{After}. For a given rain episode, the model *C* given by the equations in Table 2.3 with parameters $\left\{A, d, C_{Bkg}^{Before}, C_{Bkg}^{After}\right\}$ was fitted to M experimental ^{214}Pb net count rates $y_m\ [cps]$, measured with uncertainty $\sigma_m\ [cps]$ at temporal positions $t_m\ [s]$, by minimizing the following χ^2 function:

$$\chi^2 = \sum_{m=1}^{M} \frac{\left[y_m - C\left(t_m; A, d, C_{Bkg}^{Before}, C_{Bkg}^{After}\right)\right]^2}{\sigma_m^2} \tag{2.8}$$

where the *m* index indicates a $0.25\ h$ temporal bin and runs from 1, corresponding to the beginning of period P1, up to M, corresponding to the end of period P4.

2.2 Results and discussions

Out of 45 rainy days, 12 rain episodes (Table 2.1) were identified according to the following two criteria: i) mean rainfall rate ≥ 3 mm/h and ii) P2 duration < 4 h. The first criterion is applied in order to assure the actual observation of a rainfall event since the threshold rainfall rate of 3 mm/h corresponds to 3 times the rain gauge sensitivity. Some drizzles (secondary rain events characterized by a mean rainfall rate < 3 mm/h) are not considered during episode selection (i.e. are ignored in the overall duration and mean rainfall rate calculation in Table 1), but are however taken into account in the analysis (e.g. episodes 5 and 9 of Figure 2.5). It is not necessary to take precautions in case of irrigations concomitant or close in time to rainfall events as irrigation water does not produce any increase in the ^{214}Pb net count rate (see panel 6 of Figure 2.5).

Table 2.4 summarizes the main results obtained in reconstructing the experimental ^{214}Pb net count rate time series over the 12 rain episodes according to the model developed in the previous section. Globally, the model allowed for estimating the ^{214}Pb net count rate temporal profiles in agreement with measured time series, as proved by the good reduced chi-square values, all < 2.9 (see also Figure 2.5).

For each rain episode the best fit values of the ^{214}Pb background net count rates C_{Bkg}^{Before} and C_{Bkg}^{After} are compatible with the corresponding experimental values reported in Table 2.1. As expected, the best fit value of C_{Bkg}^{Before} is generally larger than C_{Bkg}^{After}, due to the shielding effect caused by rain water deposited and penetrated in the soil (Baldoncini et al., 2019). The exception represented by Episode 6, for which C_{Bkg}^{After} is larger than C_{Bkg}^{Before}, can be explained considering that irrigation water was distributed to the soil approximately 5 to 3 hours prior the beginning of the rain time (panel 6 of Figure 2.5).

The linear relation between measured and estimated ^{214}Pb net count rates (Figure 2.9a), described by a slope (0.93 ± 0.01) and intercept $(0.14 \pm 0.03)[cps]$, proves the good reliability of the model in the reconstructions of the 352 0.25 h bins in periods P2 and P3. The fit becomes even better if we consider only the 139 bins in periods P2 (Figure 2.9b). The best fit values of the slope (0.95 ± 0.03) and intercept $(0.15 \pm 0.08)[cps]$ are respectively compatible with 1 and 0 within 2σ, allowing to exclude statistically significant systematics.

Table 2.4. Best fit parameters obtained by applying the model developed in Section 2.1.3 to fit the experimental ^{214}Pb net count rate time series measured during the 12 rain episodes, listed in chronological order (see also Figure 2.5). The first and second columns identify respectively the rain episode number and date, the third one the reduced chi-square value obtained from the fit. The last four columns report respectively the best fit values of the *A*, *d*, C_{Bkg}^{Before} and C_{Bkg}^{After} free parameters, together with their estimation uncertainty, obtained after the χ^2 minimization procedure.

N. episode	Date [DD/MM/YYYY]	$\tilde{\chi}^2$	A±δA [cps mm^{-d} h^{d-1}]	d±δd	C_{Bkg}^{Before}±δC_{Bkg}^{Before} [cps]	C_{Bkg}^{After}±δC_{Bkg}^{After} [cps]
1	16/04/17	1.3	2.6 ± 1.0	0.48 ± 0.06	1.25 ± 0.05	1.14 ± 0.04
2	27/04/17	1.4	1.5 ± 0.6	0.77 ± 0.06	1.07 ± 0.05	0.94 ± 0.04
3	04/05/17	1.6	1.0 ± 0.4	0.75 ± 0.07	1.15 ± 0.05	1.13 ± 0.04
4	25/06/17	1.8	5.4 ± 3.2	0.42 ± 0.09	1.14 ± 0.05	1.05 ± 0.04
5	28/06/17	2.9	3.4 ± 0.7	0.34 ± 0.03	1.14 ± 0.04	1.00 ± 0.03
6	11/07/17	1.8	2.5 ± 0.5	0.48 ± 0.04	0.77 ± 0.05	0.99 ± 0.04
7	06/08/17	1.6	1.4 ± 0.3	0.71 ± 0.05	1.36 ± 0.05	0.94 ± 0.05
8	10/08/17	1.3	3.4 ± 0.2	0.16 ± 0.09	1.15 ± 0.05	0.83 ± 0.04
9	02/09/17	2.2	2.6 ± 1.0	0.48 ± 0.05	1.35 ± 0.05	1.02 ± 0.04
10	07/09/17	1.3	4.6 ± 3.7	0.23 ± 0.11	0.94 ± 0.05	0.86 ± 0.04
11	24/09/17	2.2	0.7 ± 0.6	0.99 ± 0.15	1.50 ± 0.05	1.06 ± 0.04
12	06/10/17	1.8	4.0 ± 0.8	0.39 ± 0.03	1.34 ± 0.05	1.05 ± 0.04

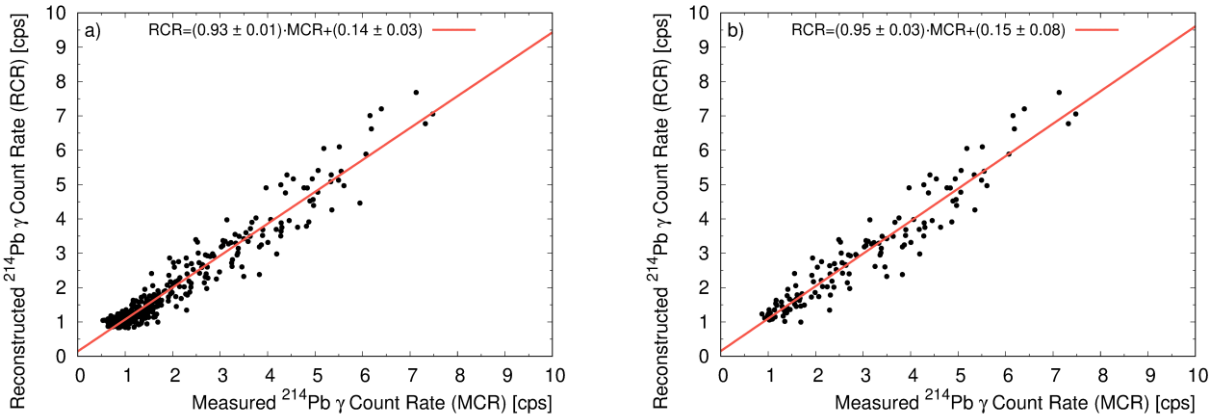

Figure 2.9. The two panels report the ^{214}Pb net reconstructed count rate (RCR) versus the ^{214}Pb net measured count rate (MCR). Panel a) reports the 352 black points acquired every 0.25 h during P2 and P3, together with the best fit linear regression (red line) with a slope of (0.93 ± 0.01), an intercept of (0.14 ± 0.03) [cps] and a coefficient of determination r^2=0.93. The subset of 139 data points acquired only in P2 is reported in panel b): the red line is characterized by a slope of (0.95 ± 0.05), an intercept of (0.15 ± 0.08) [cps] and a coefficient of determination r^2=0.91.

As introduced in Section 2.1.3, the impulsive count rate increase ΔC and the gamma activity density G can be analysed as tracers of precipitations. In particular, the model functions built from Eq. (2.4) and Eq. (2.5) are adopted to reproduce respectively the ΔC and G dependence on the rain rate R:

$$\Delta C = \Delta T \cdot A \cdot R^d \tag{2.9}$$

$$G = A \cdot R^{d-1} \tag{2.10}$$

where for a fixed $\Delta T = 0.25\ h$, ΔC and G are obtained with $\{A, d\}_{\Delta C}$ and $\{A, d\}_G$ as free parameters respectively. We analysed 82 temporal bins characterized by non-zero rainfall amount. The fit of ΔC and G

as a function of the rain rate R is shown in Figure 2.10 and Figure 1.11 and permits us to calculate the best values of $\{A, d\}_{\Delta C}$ and $\{A, d\}_G$.

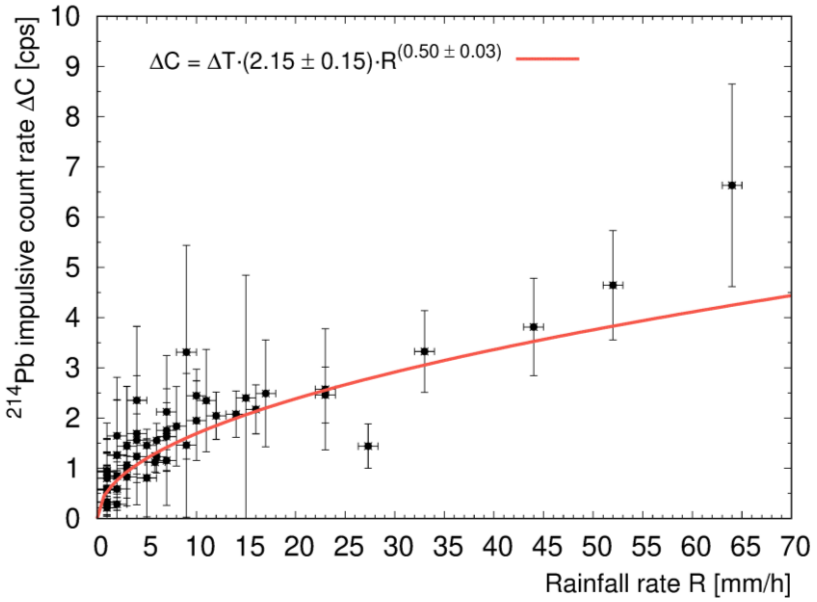

Figure 2.10. Plot of the ^{214}Pb impulsive count rate increase ΔC as function of the rainfall rate R. The ΔC values were calculated over all the 82 temporal bins ($\Delta T = 0.25\ h$) characterized by non-zero rainfall amounts. The best fit curve in red was obtained using Eq. (2.9) as model function.

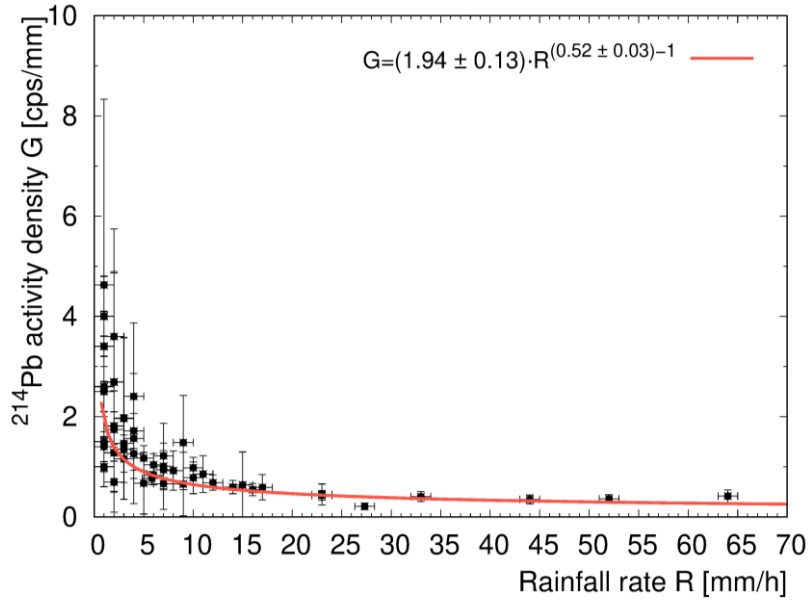

Figure 2.11. Plot of the ^{214}Pb activity density G as function of the rainfall rate R. The G values were calculated over all the 82 temporal bins ($\Delta T = 0.25\ h$) characterized by non-zero rainfall amounts. The best fit curve in red was obtained using Eq. (2.10) as model function.

We note that the best fit parameters $\{A = (2.15 \pm 0.15)[cps\ mm^{-0.50}h^{-0.50}], d = (0.50 \pm 0.03)\}_{\Delta C}$ and $\{A = (1.94 \pm 0.13)[cps\ mm^{-0.52}h^{-0.48}], d = (0.52 \pm 0.03)\}_{G}$ are completely compatible within 1σ. In the theoretical framework described in Section 2.1.3, these two independent results prove that rain induced gamma activity and the activity density are directly and inversely related to the rain rate respectively. Since d parameter is detector independent, we emphasize that our result is in excellent

agreement with the value $x = (0.5 \pm 0.1)$ published by (Mercier et al., 2009). The variability of A and d values reported in Table 2.4 can be explained with variations in in-cloud ^{222}Rn concentration and/or in in-cloud scavenging efficiency (Mercier et al., 2009).

Results shown in Figure 2.10 confirm that the impulsive count rate increase ΔC is positively correlated with the rain rate R ($\Delta C \propto R^{1/2}$), which implies that the more intense is the precipitation event, the higher is the count rate increase recorded by the PGR station. Analogously, results presented in Figure 2.11 show that the ^{214}Pb gamma activity density G is inversely correlated with the rain rate R ($G \propto R^{-1/2}$), which means that, being equal the absolute precipitation amount, the lower is the rainfall intensity (i.e. the longer is the rain duration), the higher is the radioactive content of rain water. For instance, although episode 12 and 7 were characterized by approximately the same amount of precipitated water (Table 2.1), episode 12 had about half the mean rain rate of episode 7 but a larger overall ^{214}Pb gamma activity increase, as can be inferred from the ^{214}Pb net count rate time series over the rain time (Figure 2.5).

These evidences appear even clearer by studying the activity density G as a function of the droplet diameter. Following (Villermaux and Bossa, 2009), the rain rate R can be linked to the average droplet diameter $\langle\lambda\rangle$ $[cm]$ by the relation:

$$\langle\lambda\rangle = k \cdot R^{\frac{2}{9}} \tag{2.11}$$

where $k = \frac{1}{48.5}\left[cm \cdot \left(\frac{mm}{h}\right)^{-2/9}\right]$. By substituting Eq. (2.11) in Eq. (2.10), it is possible to infer the correlation between the activity density G as a function of the average droplet diameter $\langle\lambda\rangle$:

$$G = A \cdot R^{d-1} = A \cdot \left[\left(\frac{\langle\lambda\rangle}{k}\right)^{\frac{9}{2}}\right]^{d-1} = A \cdot \left(\frac{\langle\lambda\rangle}{k}\right)^{\frac{9}{2}\cdot(d-1)} \tag{2.12}$$

By substituting the best fit parameters $\{A = (1.94 \pm 0.13)[cps\ mm^{-0.52}h^{-0.48}], d = (0.52 \pm 0.03)\}_{\mathrm{G}}$ (Figure 2.11) in Eq. (2.12), it is possible to obtain the following relation:

$$G = 1.94 \cdot \left(\frac{\langle\lambda\rangle}{k}\right)^{\frac{9}{2}\cdot(0.52-1)} = 4.43 \cdot 10^{-4} \cdot \langle\lambda\rangle^{-2.16} \tag{2.13}$$

where G is expressed in $[cps\ mm^{-1}]$ and $\langle\lambda\rangle$ in $[cm]$. However, frequency in raindrop size distributions is usually based upon volume rather than number: it is useful to define a median volume diameter λ_m, which divides the larger and smaller drops of the distribution into two groups of equal volume (Laws and Parsons, 1943). By assuming an exponential drop size distribution (Villermaux and Bossa, 2009), the median volume diameter λ_m can be linked to the average droplet diameter $\langle\lambda\rangle$ as (Eq. (5) of (Ulbrich and meteorology, 1983) with $\mu = 0$):

$$\lambda_m = 3.67 \cdot \langle\lambda\rangle \tag{2.14}$$

As depicted in Figure 2.12, is hence possible to express the relation between the activity density $G[cps\ mm^{-1}]$ and the median volume diameter λ_m $[cm]$:

$$G = 7.35 \cdot 10^{-3} \cdot \lambda_m^{-2.16} \tag{2.15}$$

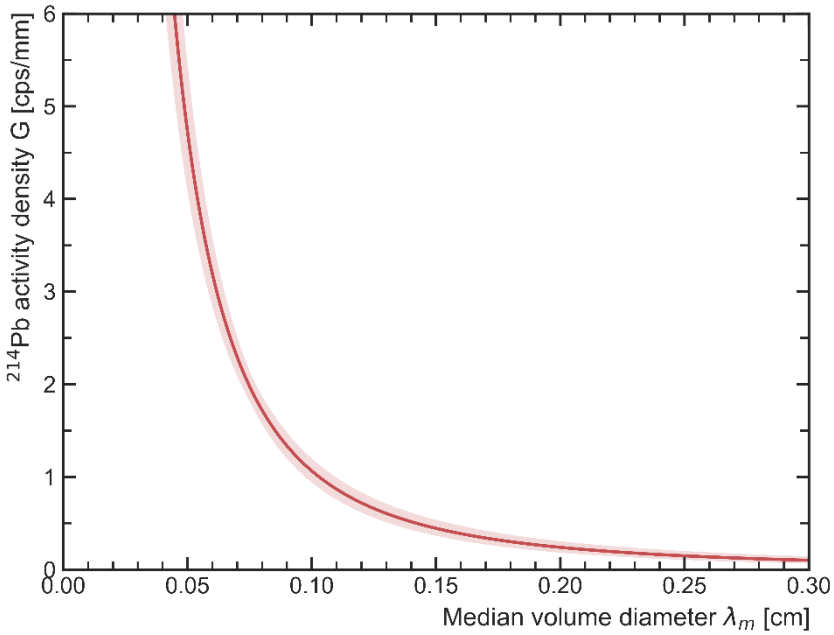

Figure 2.12. The activity density G $[cps/mm]$ of ^{214}Pb nuclei in raindrops as a function of the median volume diameter λ_m $[cm]$ follows a curve (red line) described by Eq. (2.15). The shaded pink line shows the uncertainty due to the standard deviations of the best fit parameters of Figure 2.11.

2.3 Conclusions

In this work we present an exhaustive study of the radon daughters' gamma activity measured at the ground in relation to rain rate. The results shown in this paper have been achieved analysing data acquired for 7 months with a proximal gamma-ray spectroscopy detector and an agro-meteorological station installed in a test field. We summarize here the main conclusions of this paper.

i) A reproducible mathematical model was developed for reconstructing the temporal evolution of the ^{214}Pb net count rate during rain episodes as function of the rain rate R. The reliability of the method was confirmed by two relevant results. The predicted ^{214}Pb net count rates, 5 hours before the rain event and 5 hours after the ^{214}Pb exponential decrease post-rain, are in agreement at 1σ level with the measured values (Table 2.2 and Table 2.4). The ^{214}Pb signals reconstructed by the model are linearly correlated with the values measured during the rain time with a coefficient of determination r^2=0.91. Moreover, the slope and the intercept coefficients are compatible within 2σ with 1 and 0 respectively (Figure 2.9).

ii) The impulsive increase of ^{214}Pb count rates (ΔC) observed during every rain event is clearly related to the rain rate (R) by the power law $\Delta C = A \cdot R^d$, where $A = (2.15 \pm 0.15)[cps\ mm^{-0.50} h^{-0.50}]$ is an equipment dependent parameter. The calculated universal parameter $d = (0.50 \pm 0.03)$ proves that the expected increase of radon daughters'

activity at the ground due to rainfalls depends on the square root of the rain rate (Figure 2.10).

iii) For a fixed rainfall amount, the lower is the rainfall intensity (i.e. the longer is the rain duration), the higher radon daughters' content of the rain water (i.e. the ^{214}Pb activity density G). We observed a power law dependence $G = A \cdot R^{d-1}$ between the ^{214}Pb gamma activity density $G\ [cps\ mm^{-1}]$ and the rain rate R (Figure 2.11). The best fit parameters $A = (1.94 \pm 0.13)[cps\ mm^{-0.52} h^{-0.48}]$ and $d = (0.52 \pm 0.03)$ agree with those obtained by an independent analysis in ii).

iv) Studying the ^{214}Pb activity density G as a function of droplet size, we can conclude that radon daughters' abundance in a rain droplet is inversely proportional to the rain median volume diameter λ_m, according to the following function: $G = 7.35 \cdot 10^{-3} \cdot \lambda_m^{-2.16}$. This experimental evidence shows that the smaller droplets have on average higher radon daughters' abundances.

We shall learn more about the rain formation and scavenging mechanisms from future refined gamma measurements at the ground, including ^{214}Bi data. Using the data from the network of thousands gamma sensors distributed on the ground (typically utilised for monitoring the air radioactivity in case of nuclear fallout) or radiation portal monitors the activity density of the rain could provide valuable information to cloud science.

Chapter 3

Gamma-ray spectroscopy in the framework of precision agriculture and soil water content

The continuous determination of soil moisture dynamics at field scale with non-invasive and contactless measurement techniques is at the time the most promising challenge for optimizing agricultural management and in particular for a sustainable use of water (Ochsner et al., 2013). Among the proximal sensing techniques, gamma ray spectroscopy is recognized as one of the best space-time trade off methods (Bogena et al., 2015; Rouze et al., 2017). Thanks to the permanent installation of measurement stations, soil water content can be estimated in real time on the basis of temporal changes in gamma ray intensity to which soil moisture is negatively correlated. Although the possibility of performing non-destructive and fast measurements has been investigated in the past decades (Carroll, 1981; Grasty, 1997; Loijens, 1980; McHenry and Gill, 1970), recent developments in cyber-physical systems boosted by investments in Industry 4.0 sectors and supported by the cloud technology are opening new perspectives in the field. In this scenario, the gamma ray spectroscopy method excellently matches the current needs for high accuracy nonstop soil water content monitoring representing a joining link between punctual and satellite fields of view.

In section 3.1 I present the relation between soil water content and gamma signal, which is applied to a Monte Carlo synthetic calibration performed with the specific soil composition of the experimental site. The proposed method in estimating soil water content provides excellent results (Baldoncini et al., 2018a).

In section 3.2 I take into account the gamma signal attenuation due to the growing plants in the test field. The presented approach permits soil moisture estimation in complete agreement with gravimetric data (Baldoncini et al., 2019).

In section 3.3 is presented a comparison between the soil water content measured with the gamma detector and the data simulated by the models AquaCrop, CRITeRIA and IRRINET. Overall the entire data-taking period CRITeRIA showed the best agreement with the experimental data (Strati et al., 2018).

3.1 Investigating the potentialities of Monte Carlo simulation for assessing soil water content via proximal gamma-ray spectroscopy

Monte Carlo methods refer to a broad class of computational techniques that use random sampling to solve a given problem. Since a scenario including the photon emission from all the radionuclides in the soil, their transport and detection is too complex for an analytical solution, a computational technique can be involved. Computer simulations can be a very powerful tool in modeling such a scenario. In this context, the power of Monte Carlo methods relies in the possibility of simulating the behavior of each single photon, by simulating both the emission and propagation of photons one-by-one. Monte Carlo simulations generate the random distances each photon travels before undergoing interactions in a specific medium, testing the interaction most likely to occur and determining full or partial energy deposition.

In the panorama of environmental variables affecting radiometric measurements, water content and bulk density are the most crucial factors. As water has 1.11 times as many electrons per gram compared to

most soils, water is 1.11 times as effective in attenuating gamma-radiation compared to typical soils (Grasty, 1997). If, from one side, proximal gamma-ray spectroscopy experienced in the last decades a boost in terms of technological and spectral analysis developments, concerning the specific topic of soil moisture assessment current radiometric data processing is typically based on first order analytical models (Carroll, 1981; Grasty, 1997; Loijens, 1980). These methods lack however a custom approach able to integrate individual site characteristics to distinct experimental set up features. In this perspective, Monte Carlo simulations can overcome the limits of analytical solutions, which generally address the description of the sole unscattered gamma-ray flux, by providing information on the entire gamma spectra (Allyson and Sanderson, 1998; Androulakaki et al., 2016; Vlastou et al., 2006). In a Monte Carlo simulation all parameters can be separately controlled and uncertainties coming from temporary variations in the experimental conditions can be excluded, which is particularly relevant in relation to calibration procedures and feasibility studies (Chirosca et al., 2013; De Groot et al., 2009; Van der Graaf et al., 2011). This peculiarity makes the methodology highly versatile in terms of input boundary conditions and extraordinarily effective in both investigating the effects of individual variables (e.g. for sensitivity studies) and in the calibration of different source-detector systems (e.g. permanent stations, carborne based platforms).

The Monte Carlo simulations are in this section applied to the reconstruction of gamma-ray spectra collected by a NaI scintillation detector permanently installed at an agricultural experimental site. A two steps simulation strategy based on a geometrical translational invariance is developed. The strengths of this approach are the reduction of computational time with respect to a direct source-detector simulation, the reconstruction of ^{40}K, ^{232}Th and ^{238}U fundamental spectra, the customization in relation to different experimental scenarios and the investigation of effects due to individual variables for sensitivity studies. The reliability of the simulation is effectively validated against an experimental measurement with known soil water content and radionuclides abundances. I derived theoretically the relation between soil water content and gamma signal and applied to a Monte Carlo synthetic calibration performed with the specific soil composition of the experimental site. Ready to use general formulae and simulated coefficients for the estimation of soil water content are also provided adopting standard soil compositions. Linear regressions between input and output soil water contents, inferred from simulated ^{40}K and ^{208}Tl gamma signals, provide excellent results demonstrating the capability of the proposed method in estimating soil water content with an average uncertainty < 1%.

3.1.1 Horizons of proximal gamma-ray spectroscopy

Proximal gamma-ray spectroscopy investigates high energy photon radiation produced in the decays of ^{40}K and daughter products of the ^{238}U and ^{232}Th decay chains, which are the only naturally occurring radionuclides producing gamma radiation of sufficient energy and intensity to be measured in the framework of in-situ surveys. Since each gamma decay has a specific emission energy, it is possible to recognize distinctive structures (photopeaks) in a gamma spectrum, which allow for the quantification of ^{40}K, ^{238}U and ^{232}Th abundances in the soil source. The integrated numbers of events inside the energy ranges associated to the main photopeaks (IAEA, 2003) are typically adopted for determining the corresponding counts per second (cps) which are related to ^{40}K, ^{238}U and ^{232}Th activities in the soil by some sensitivity calibration factors. While ^{208}Tl (^{232}Th decay chain) and ^{40}K are distributed solely in the soil, gamma radiation produced by the decay of ^{214}Bi (^{238}U decay chain) comes both from ^{214}Bi in the soil and from ^{214}Bi in the atmosphere originated by the decay of ^{222}Rn gas exhaled from rocks and soils.

The number of net counts recorded in the photopeak centered at the gamma emission energy E by a detector placed at height h scales with the photon flux $\Phi(h)$, which can be written as follows, assuming an

infinite half-space soil volume source, a homogeneous radionuclide concentration and homogeneous soil and air materials (Feng et al., 2009):

$$\Phi(h) = \frac{A_V P_\gamma}{2\mu_s(E)} \int_0^{\pi/2} \sin\theta \, e^{-\frac{\mu_a(E)h}{\cos\theta}} d\theta \tag{3.1}$$

where A_V is the unit volume activity in Bq/m^3, P_γ is the γ-ray intensity in number of gammas per Bq, $\mu_s(E)$ and $\mu_a(E)$ are the linear attenuation coefficients in m^{-1} of soil and air, respectively, and θ is the polar angle between the detector vertical symmetry axis and one radioactive unit element in the source. Linear attenuation coefficients μ define the probability P_0 that a photon travels a distance d in a given material without suffering any interaction and are generally expressed as the product of the mass attenuation coefficients μ/ρ (m^2/kg) (which depend only on the material composition and on photon energy) times the material density ρ (kg/m^3):

$$P_0(E) = e^{-\mu(E)d} = e^{-\left(\frac{\mu}{\rho}(E)\right)\rho d} \tag{3.2}$$

Eq. (3.2) is what governs photon survival in traversing a given material as photon attenuation is respectively positively and negatively correlated to material density and photon energy. This is the key for understanding the lateral and vertical horizons of proximal gamma-ray spectroscopy.

The vertical field of view of a gamma-ray detector placed at height h can be estimated on the basis of the photon flux produced within a soil thickness t, which can be written according to Eq. (3.3), where the notation is simplified for the implicit photon energy dependence (Feng et al., 2009):

$$\Phi(h) = \frac{A_V P_\gamma}{2\mu_s} \int_0^{\pi/2} \sin\theta \, e^{-\frac{\mu_a h}{\cos\theta}} \left[1 - e^{-\frac{\mu_s t}{\cos\theta}}\right] d\theta \tag{3.3}$$

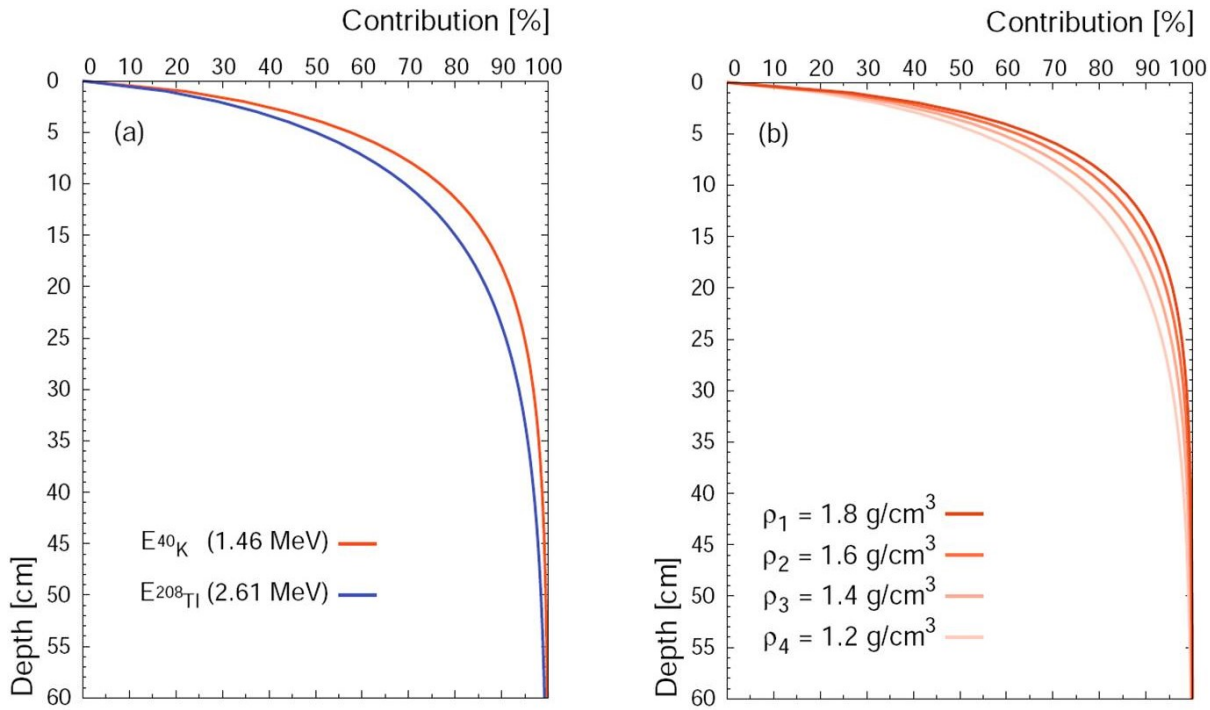

Figure 3.1. Cumulative percentage contribution to the unscattered photon flux at ground level as function of soil depth. Panel (a) refers to ^{40}K (1.46 MeV) and ^{208}Tl (2.61 MeV) emission energies and a soil density ρ = 1.345 g/cm^3 (corresponding to the soil bulk density of the experimental site). Panel (b) considers a typical [1.2 – 1.8] g/cm^3 range of soil densities and the ^{40}K gamma emission energy.

The cumulative contribution to the unscattered photon flux as function of soil depth has a steeper profile for decreasing photon energy (Figure 3.1a) and for increasing soil density (Figure 1.1b). Considering a [1.2 – 1.8] g/cm^3 typical range of soil densities, 95% of the unscattered gamma flux at the soil surface is produced within the first [19 – 28] cm for ^{40}K gamma photons (E = 1.46 MeV) and within the first [24 – 36] cm for ^{208}Tl gamma photons (E = 2.61 MeV) (Table 3.1).

Table 3.1. Thickness of the soil layer producing 95% of the unscattered photon flux at ground level for ^{40}K (1.46 MeV) and ^{208}Tl (2.61 MeV) gamma energies for typical values of soil bulk density.

ρ [g/cm^3]	Thickness [cm]	
	E_{40K} (1.46 MeV)	E_{208Tl} (2.61 MeV)
1.2	28	36
1.4	24	31
1.6	21	27
1.8	19	24

The horizontal field of view of a gamma-ray detector placed at height *h* can be estimated on the basis of the photon flux produced within a cone of radius *r* and opening angle 2θ* (Feng et al., 2009):

$$\Phi(h) = \frac{A_V P_\gamma}{2\mu_s} \int_0^{\theta^*} \sin\theta \, e^{-\frac{\mu_a h}{\cos\theta}} \left[1 - e^{-\mu_s\left(\frac{r}{\sin\theta} - \frac{h}{\cos\theta}\right)}\right] d\theta \qquad (3.4)$$

In the height range of proximal surveys (~ few meters), the cumulative contribution to the unscattered flux as function of the cone radius is slightly influenced by photon energy (Figure 3.2a), while it

sensibly changes for different heights above the ground (Figure 3.2b). By lifting a detector from 1 m to 10 m height the radius from which 95% of the unscattered flux is produced increases from ~15 m to ~85 m (Table 3.2). This trend is also related to the behaviour of the differential contribution to the unscattered photon flux originated by concentric hollow cylinders: by increasing the detector height, the hollow cylinder originating the highest contribution is progressively farer from the detector vertical axis (Figure 3.3).

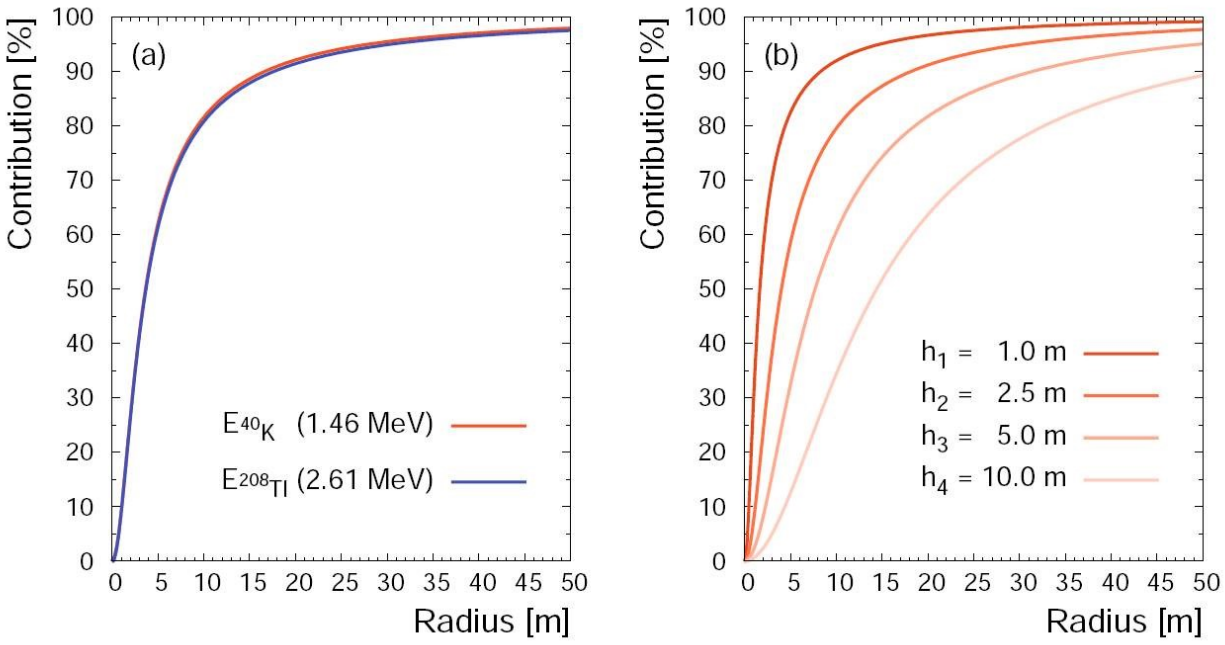

Figure 3.2. Cumulative percentage contribution to the unscattered photon flux as function of the radial distance from the detector vertical symmetry axis assuming the soil density of the experimental site. Panel (a) refers to ^{40}K (1.46 MeV) and ^{208}Tl (2.61 MeV) emission energies and a detector height h = 2.25 m (corresponding to the height of the experimental set up). Panel b (b) considers a [1 – 10] m height range and the ^{40}K gamma emission energy.

Photon flux attenuation for increasing height is directly connected to the acquisition time which is needed for attaining a target counting statistics (Table 3.2): by increasing the detector height from 1 m to 10 m, the acquisition time needs to be extended by approximately 20% in order to measure the same number of events in a given energy range.

Table 3.2. Radial distance from the detector vertical symmetry axis from which 95% of the unscattered photon flux is produced, together with the acquisition time needed to collect 10^4 photons for unitary parent radionuclides abundances in dry soil and for the specific experimental set up used in the Monte Carlo simulations. Values are obtained for ^{40}K (1.46 MeV) and ^{208}Tl (2.61 MeV) gamma energies considering different heights of the detector.

Height [m]	E_{40K} (1.46 MeV)		E_{208Tl} (2.61 MeV)	
	Radius [m]	Time [10^3 s]	Radius [m]	Time [10^4 s]
1.0	14.9	1.07	15.7	2.71
2.5	31.4	1.11	32.9	2.75
5.0	49.6	1.16	55.5	2.86
10.0	77.5	1.29	88.5	3.17

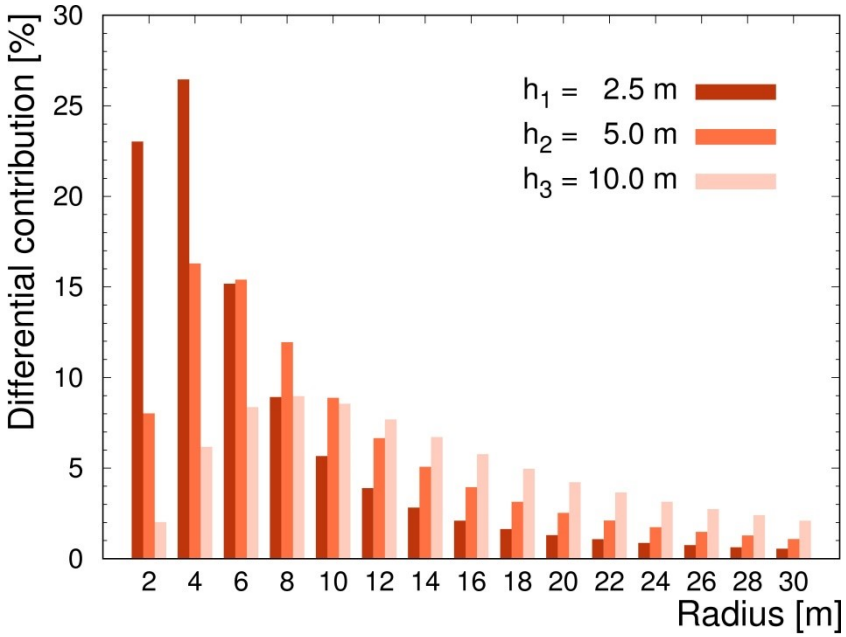

Figure 3.3. Histograms of the percentage contributions to the ^{40}K (1.46 MeV) unscattered photon flux produced by concentric hollow cylinders of soil centered at the detector vertical axis. Each x axis value corresponds to the value of the external radius of each cylinder. The difference between external and internal radius of the cylinders is always 2 m. The histograms are obtained considering a 2.5 m, 5.0 m and 10.0 m height of the detector.

3.1.2 Monte Carlo simulation method

The three major tasks of the Monte Carlo simulation applied to proximal gamma-ray spectroscopy consist in: (i) generating radioactive decays inside a source having distinct features (e.g. density, chemical composition, radionuclide distribution), (ii) chasing photons by simulating their propagation/interactions in different media, (iii) reconstructing the gamma-ray spectrum recorded by a specific detection system.

The photon flux that a detector intercepts comes, in principle, from all the radioactive sources present in the environment; however, if the photon emission points are spread throughout a soil of infinite dimensions and if photons are radiated isotropically, the probability for a photon to reach the detector position is extremely low (i.e. the computational time for attaining enough statistics is dramatically high).

A C++ Monte Carlo code based on GEANT4 (Agostinelli et al., 2003) is developed in order to perform a simulation structured into two independent steps. The adopted strategy relies on a translational invariance (Feng et al., 2009; Jacob and Paretzke, 1986; Likar et al., 2004): the first step is dedicated to the Photon Field Building (PFB) (Figure 3.4), while the second one is devoted to the Gamma Spectrum Reconstruction (GSR) inside the detector (Figure 3.5). The translational invariance is justified by the fact that, for homogeneous traversed materials and homogeneous radioactive content of the source, a photon radiated from a given point inside a volume element propagates equivalently to a photon emitted at the same depth from a laterally shifted point (i.e. the two photons undergo the same interactions and travel the same distances in all materials). As the output of the PFB process is used as input for the GSR simulation step, the simulation of photon transport from the emission point to the detector position is completely disentangled from the simulation of the detected spectral shape. For this reason this simulation strategy is highly versatile: indeed, only the GSR process should be simulated in order to reconstruct gamma-ray spectra acquired by various detection systems for given source and traversed media.

3.1.2.1 Photon Field Building (PFB)

For symmetry reasons, a geometry of an infinite source and a finite-volume detection plane can be equally modeled as a geometry of a finite-volume source and an infinite detection plane (Figure 3.4). In the PFB process the spatial scale of the simulation is adjusted to the experimental site conditions (see section 3.1.3.1). Photons are isotropically radiated one-by-one from homogeneously distributed emission points located inside a 1 m x 1 m x 1 m cubic source and tracked until they lose their energy down to a 0.2 MeV threshold or escape the 100 m x 100 m x 10 m global simulation volume (Figure 3.4a). User defined 100 m x 100 m detection planes are placed at a height 2.250 m and 3.108 m, corresponding to the altitude above the ground of the lower and upper surfaces of the detector container. These planes do not act as physical media in which photons propagate and interact, but they allow to record the necessary information regarding photon states, i.e. spatial position, energy and direction cosines. The original theoretical geometry is then restored by shifting a posteriori the photons arrival positions on the detection surface, which essentially translates into "piling up" 10^4 $1m^2$ tiles in order to reconstruct the Photon Field Layer (PFL) that would have been obtained from a direct simulation of the real geometry (Figure 3.4b).

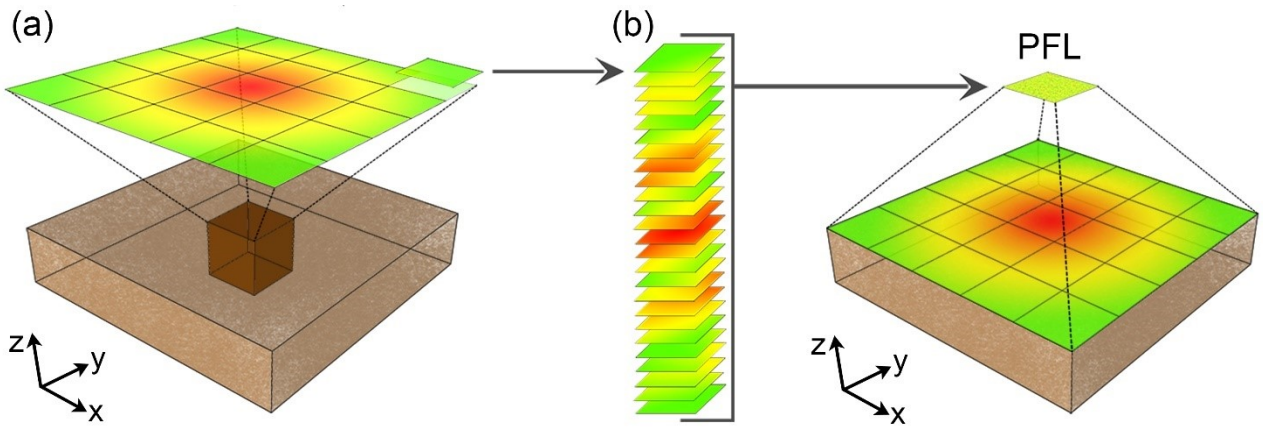

Figure 3.4. Scheme of the Monte Carlo Photon Field Building (PFB) process. (a) A 1 m x 1 m x 1 m cube is adopted as isotropic and homogeneous source of photons which are propagated one-by-one inside the 100 m x 100 m x 10 m world volume. (b) The application of the horizontal translation to photons arrival position on the 100 m x 100 m detection surface corresponds to a "piling up" of 10^4 $1m^2$ tiles of the detection plane. This procedure allows for reconstructing the Photon Field Layer (PFL), which contains information on photons spatial position, energy and direction cosines and which corresponds to the photon field that would have been obtained from a direct simulation of the actual source-detector configuration.

As expected, the event and energy surface densities associated to the detection surfaces are maximal at the center (i.e. on the vertical with respect to the volume source position) and gradually decrease in the radial direction, directly reflecting the fact that photons reaching positions close to the center are the ones which, on average, traveled a shorter distance and suffered fewer interactions (Figure 3.5a and Figure 3.5c). The radial pattern disappears after the application of the translational symmetry, which leads to the reconstruction of homogeneous event and energy areal distributions on the PFL (Figure 3.5b and Figure 3.5d).

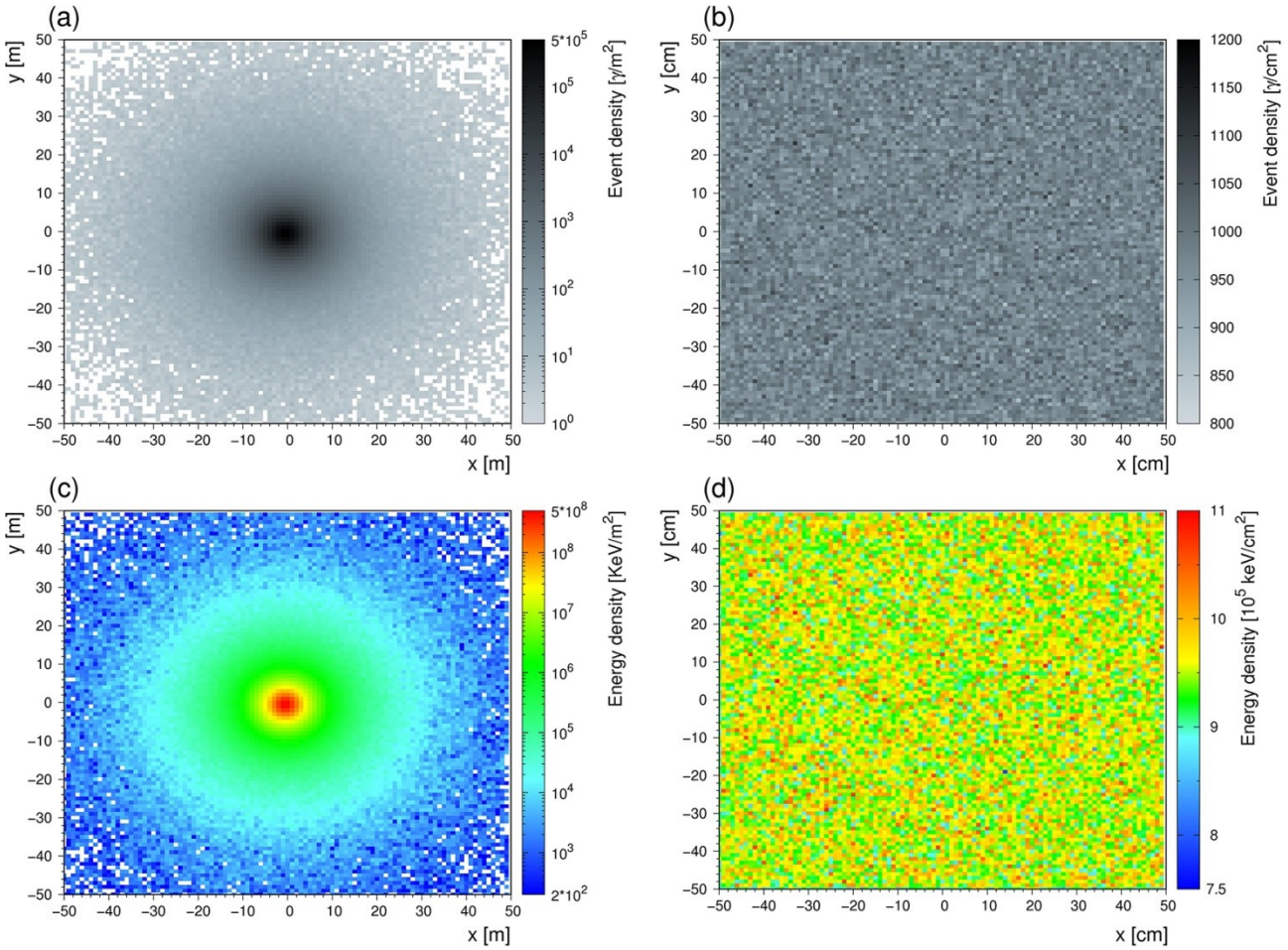

Figure 3.5. (a) and (c) show the photon and energy areal distributions on the 10^4 m^2 planar detection surface placed at 2.250 m height. (b) and (d) illustrate the corresponding homogeneous event and energy areal distributions in the 1m^2 PFL obtained after the application of the translational invariance.

The most relevant variables that can be set are: the geometrical dimensions of the global system, the materials used (in terms of both chemical composition and density), the source configuration (e.g. point-like or diffuse, isotropic or collimated), the radionuclide species emitting gamma radiation and the radionuclide distribution in the source. The radioactivity of the source is defined by setting the total number of generated photons and their energy according to the emission spectrum of the parent nuclide. Therefore, simulation of photons emitted from natural radioactive sources is separately performed for ^{40}K, ^{238}U and ^{232}Th, which is also a key point for the reconstruction of the detector fundamental spectra (Figure 3.8).

The number of photons emitted per second by a unitary concentration of the i-th atomic species (n_i) can be determined as stated by:

$$n_i = N_i a_i \rho_{soil} V \tag{3.5}$$

where N_i is the number of photons emitted per decay by the i-th atomic species, a_i is the specific activity associated to a unitary concentration of the i-th atomic species (Bq/kg) (IAEA, 2003), ρ_{soil} is the soil density (kg/m^3) and V is the source volume (m^3). The total number of photons γ_i, emitted on average by a soil having radioelement concentration c_i during a time interval t, can be evaluated by using:

$$\gamma_i = n_i c_i t \tag{3.6}$$

Storing particle direction cosines allows for distinguishing, for each detection surface, photons traveling upwards from those traveling downwards.

3.1.2.2 Gamma Spectrum Reconstruction (GSR)

The PFLs of photons moving upwards and downwards at respectively 2.250 m and 3.108 m height are used as inputs for the GSR stage (Figure 3.6a) and placed respectively on the bottom and on the top of the Monte Carlo detector prior the resuming of the simulation of photon propagation and interaction with the equipment materials. The detector employed in the experimental site and described in section 3.1.3.1 is modeled in the GSR process according to the simplified geometrical scheme shown in Figure 3.7. In particular, the simulated components are the detector container, the photomultiplier tube, the 1L NaI (Tl) scintillator and the detector casing. The detector behaves as a device having ideal energy resolution: what is simulated are the energy depositions inside the different detector materials, which implies that the photopeaks corresponding to specific gamma emissions are reproduced in the Monte Carlo spectrum as "Dirac delta functions" (Figure 3.6b). The ^{40}K, ^{238}U and ^{232}Th energy-deposition spectra are broadened by folding with Gaussian resolution functions characterized by energy dependent values of the Full Width at Half Maximum (FWHM).

The shapes of six prominent photopeaks observed in measured spectra, associated with the ^{238}U and ^{232}Th decay chains most intense gamma lines and to the single ^{40}K gamma emission, are fitted according to a Gaussian shape, providing a mean value and a FWHM value. The FWHM values have subsequently been fitted to model the FWHM energy resolution curve (Figure 3.6c) according to the following simplified parameterization:

$$FWHM = k\sqrt{E} \tag{3.7}$$

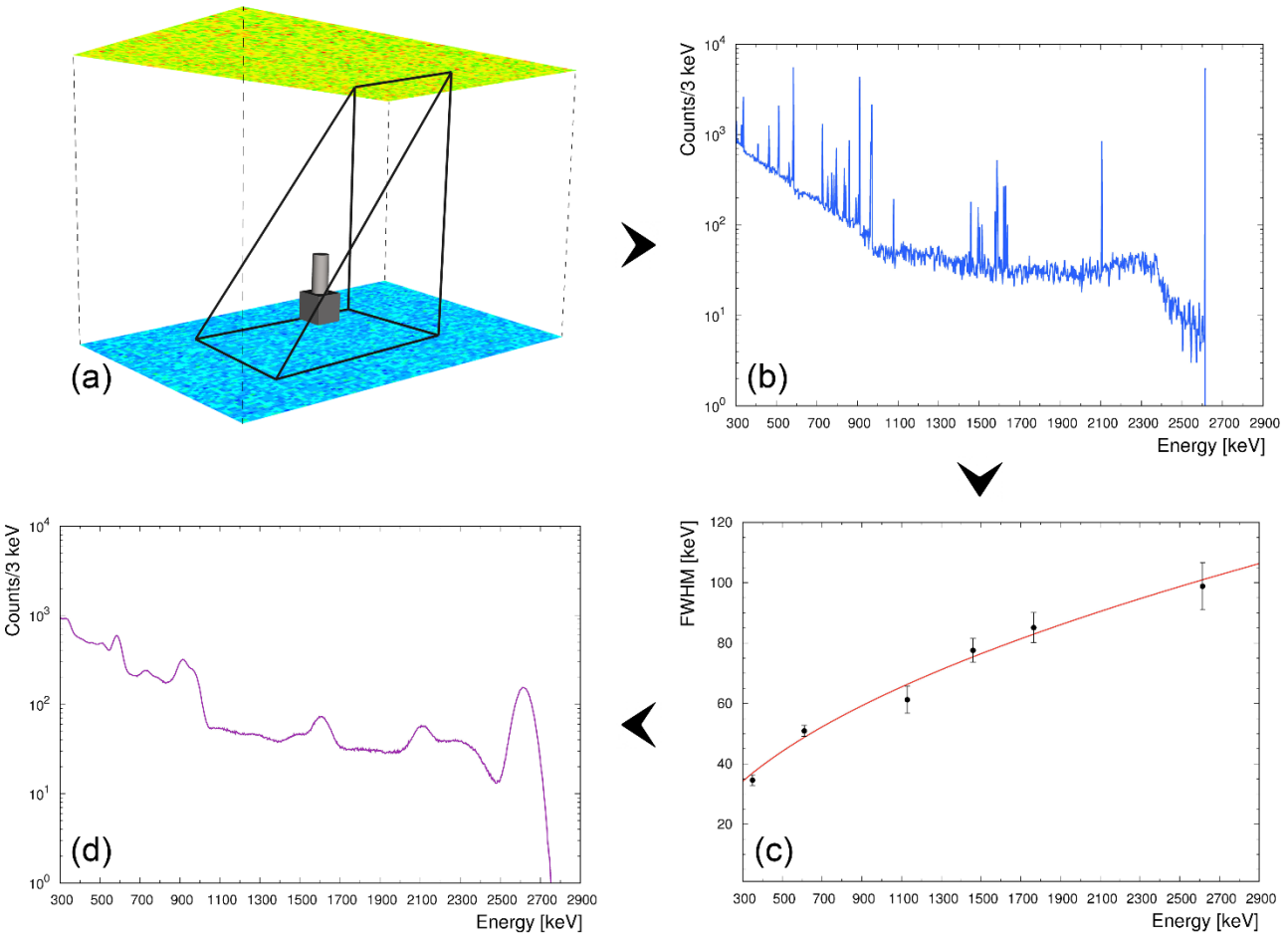

Figure 3.6. Scheme of the four steps of the Gamma Spectrum Reconstruction (GSR) process. (a) The Monte Carlo detector is placed in between the 2.250 m and 3.108 PFLs. (b) ^{232}Th Monte Carlo spectrum with ideal energy resolution obtained after photon energy deposition. (c) Full Width at Half Maximum (FWHM) energy resolution curve obtained by fitting, according to Eq. (3.7) (k=1.97 $\sqrt{keV}$), the six values determined by reconstructing the Gaussian shape of prominent photopeaks observed in measured spectra. (d) ^{232}Th Monte Carlo spectrum obtained summing the two spectra associated to photons moving upwards and downwards broadened by folding with the energy resolution curve.

3.1.3 Application and validation of the method

The Monte Carlo simulation method presented above is applied in the context of a proximal gamma-ray spectroscopy experiment (Baldoncini et al., 2018a; Strati et al., 2018). An ad-hoc NaI measurement station is designed and installed at an agricultural experimental field with the aim of estimating soil water content on the basis of temporal changes in photopeak counting rates. The simulation of gamma-ray spectra acquired at the experimental site and the determination of fundamental spectra allowed for estimating soil water content and evaluating the accuracy of the method.

3.1.3.1 Experimental site and setup

The experimental site is a 40 m x 108 m testing field (44.57° N, 11.53° E; 16 m above sea level) of the Acqua Campus, a research center of the Emiliano Romagnolo Canal (CER) irrigation district in the Emilia-Romagna region (Italy). The soil is characterized by a dry density of 1.345 g/cm^3 and by a loamy texture, determined on the basis of measured percentages of sand (45%), silt (40%) and clay (15%) (Strati et al., 2018).

Percentages of the major oxides, quantified after a mineralogical analysis, are adopted for modeling the composition of the simulated soil material (Table 3.3).

Table 3.3. Chemical composition of the soil adopted in the Monte Carlo simulation obtained after a mineralogical analysis. Trace elements and organic matter were considered negligible for the purpose of the simulation. The H_2O mass fraction refers to the structural water, corresponding to water incorporated in the formation of soil minerals.

Major oxides/compounds	Mass Fraction [%]
Si_2O	60.41
Al_2O_3	12.72
CaO	10.43
Fe_2O_3	4.71
MgO	3.08
K_2O	2.25
Na_2O	1.04
TiO_2	0.55
P_2O_5	0.29
MnO	0.13
H_2O	4.34
Air	0.05

A total of 16 soil samples are collected within a 15 m radial distance from the detector vertical axis to homogeneously cover the area generating about 85% of the signal (Figure 4 of (Baldoncini et al., 2019)). The radioactive content of the samples is characterized on the basis of 1 hour gamma spectra acquired by the MCA_RAD system, which is made up of two coaxial HPGe detectors, able to automatically perform up to 24 measurements without human attendance (Xhixha et al., 2013). The mean abundances obtained by averaging over all samples are a_K = (1.59 ± 0.17) 10^{-2} g/g, a_U= (2.48 ± 0.25) μg/g and a_{Th} = (9.37 ± 1.12) μg/g. The relatively low standard deviations highlight a homogeneous radionuclide distribution over the area of interest of the experimental site.

Gamma-ray spectra are measured by a permanent gamma station specifically designed and built for the experiment (Figure 3.7). A 1L sodium iodide (NaI) crystal is placed inside a steel box mounted on top of a 2.25 m high steel pole. The gamma spectrometer is coupled to a photomultiplier tube base which output is processed by a digital multi-channel analyzer (MCA, CAEN γstream) having 2048 acquisition channels; the whole system is powered by a solar panel. A dedicated software is developed to post-process the output list mode files (i.e. a continuous logging of individual photons arrival time and acquisition channel) in order to (i) generate gamma spectra corresponding to 15 minutes acquisition time, (ii) perform an energy calibration procedure, (iii) remove the spectral background and (iv) retrieve the net count rate in the main ^{40}K, ^{214}Bi and ^{208}Tl photopeaks (Baldoncini et al., 2019).

3.1.3.2 Simulated and experimental spectra

The Monte Carlo method illustrated in section 3.1.2 is applied to simulate gamma-ray spectra acquired at the experimental site by the setup described in section 3.1.3.1. The reliability of the simulation is tested against an experimental measurement performed in bare soil condition with known gravimetric water content (see definition in section 3.1.4.1). The weighted average gravimetric water content at calibration time w^{Cal} = (0.167 ± 0.008) kg/kg is estimated on the basis of a dedicated gravimetric measurements survey,

during which soil samples are collected with the same spatial distribution adopted for the radiometric characterization (Baldoncini et al., 2019).

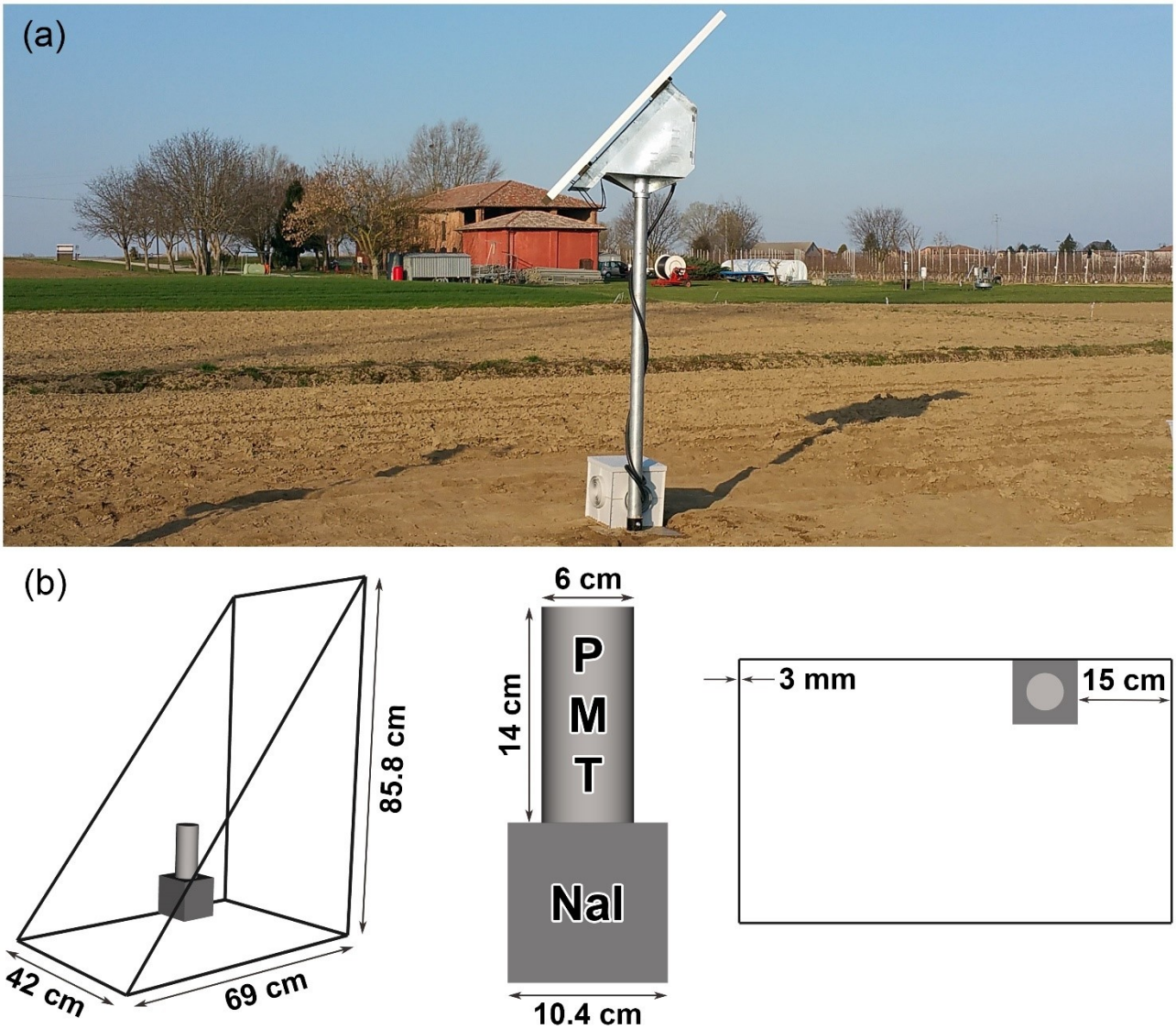

Figure 3.7. Panel (a) shows a picture of the NaI gamma station installed at the experimental site. Panel (b) illustrates the scheme of the experimental set up adopted for the modeling of the Monte Carlo simplified detector.

Independent ^{40}K, ^{238}U and ^{232}Th Monte Carlo simulations are carried out in order to perform a full-spectrum detector calibration by reconstructing the so-called fundamental spectra (Figure 3.8), i.e. the individual radionuclide spectral shapes that a specific detection system would measure for unitary acquisition time and unitary radionuclide concentration in the soil (Hendriks et al., 2001). Fundamental spectra are generally determined by means of an experimental sensitivity calibration process according to which high statistics radiometric measurements performed on calibration homogeneous extended sources (calibration pads or natural calibration sites) successively undergo a least square analysis, necessary to unfold the separate ^{40}K, ^{238}U and ^{232}Th spectral components (Caciolli et al., 2012). As the least square analysis does not intrinsically comprise any constraint on the physical gamma emission lines, this method can give rise to residual interferences in the fundamental spectral shapes of different radionuclides, especially in correspondence of photopeaks structures. In this perspective, the Monte Carlo simulation has the remarkable advantage of avoiding any type of cross-talk effect in the reconstruction of individual spectral shapes, typically caused by the minimization procedure or by the co-presence of different radionuclides

having close energy gamma lines (e.g. in the case of the 0.583 MeV (^{208}Tl), 0.609 MeV (^{214}Bi) and 0.662 MeV (^{137}Cs) gamma emissions).

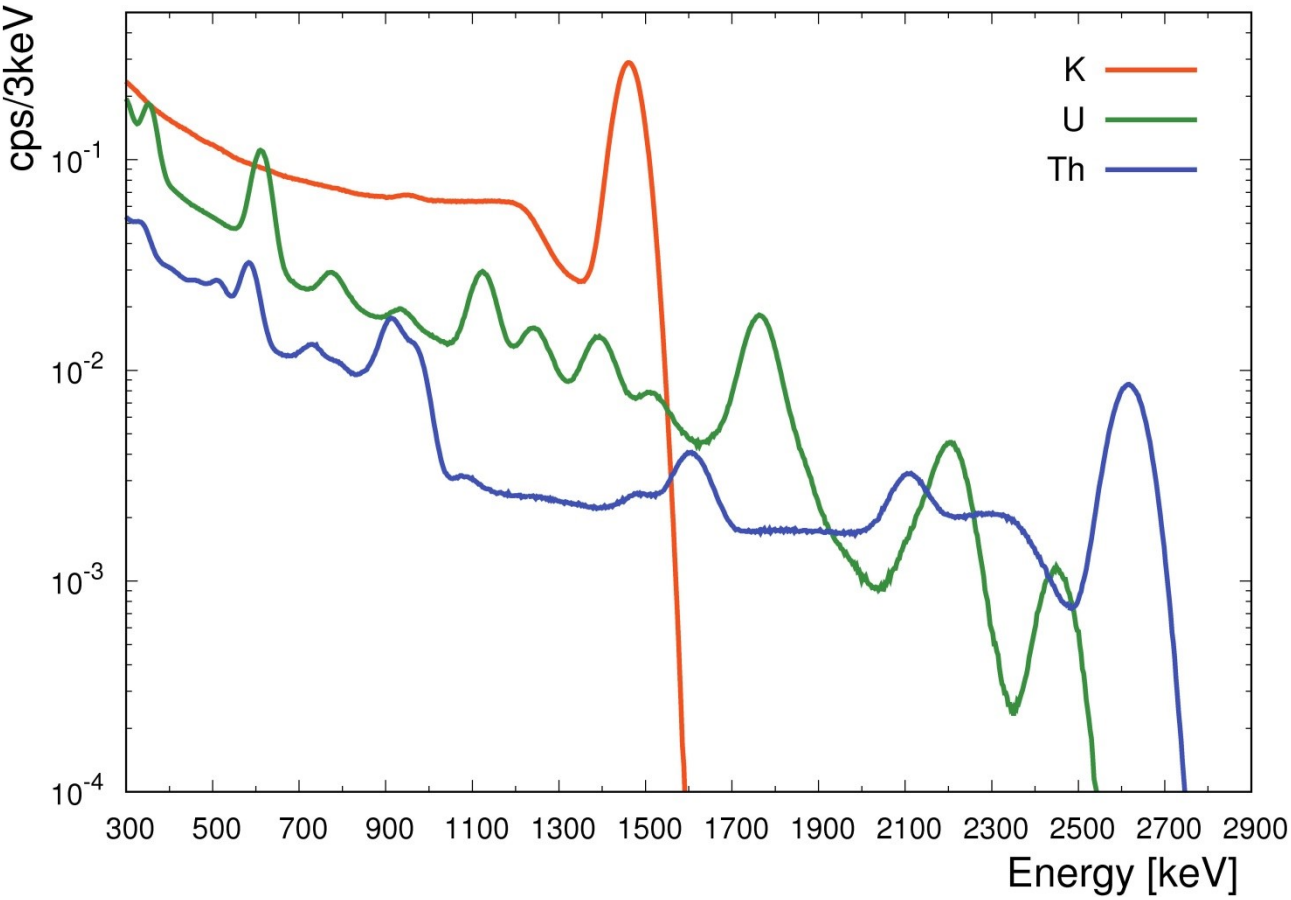

Figure 3.8. ^{40}K (orange), ^{238}U (green) and ^{232}Th (blue) fundamental spectra obtained with the Monte Carlo simulations referred to unitary radionuclide concentrations in dry soil condition (a_K= 10^{-2} g/g, a_U = 1 μg/g and a_{Th} = 1 μg/g) and to calibration gravimetric water content (w^{Cal} = 0.167 kg/kg).

The fundamental spectra are used for the FSA-NNLS analysis (Guastaldi et al., 2013; Strati et al., 2015) to reconstruct the 2 hour (10.00 a.m. – 12 a.m.) calibration experimental measurement concomitant with the gravimetric sampling (Figure 3.9). The acquisition is distant from rainfall events and scheduled irrigations and is performed with stable atmospheric parameters (i.e. air temperature and pressure, wind direction and speed).

As the adopted Monte Carlo simulation method does not structurally provide any background radiation contribution, a cosmic background spectral shape to be subtracted to the experimental measurement is inferred from a 24 hour background calibration measurement according to the approach described in (Baldoncini et al., 2018b). Without the introduction of any arbitrary rescaling factor, a good agreement between experimental and simulated spectra is obtained concerning both absolute counting statistics and the spectral shape profile (Figure 3.9). The reconstructed a_K = 1.63 10^{-2} g/g and a_{Th} = 10.92 μg/g abundances are respectively compatible at 0.2 and 1.4 σ level with the radioactive content of the experimental site (see section 3.1.3.1), while the a_U = 3.91 μg/g abundance is highly affected by the extra contribution in the experimental measurement due to atmospheric radon.

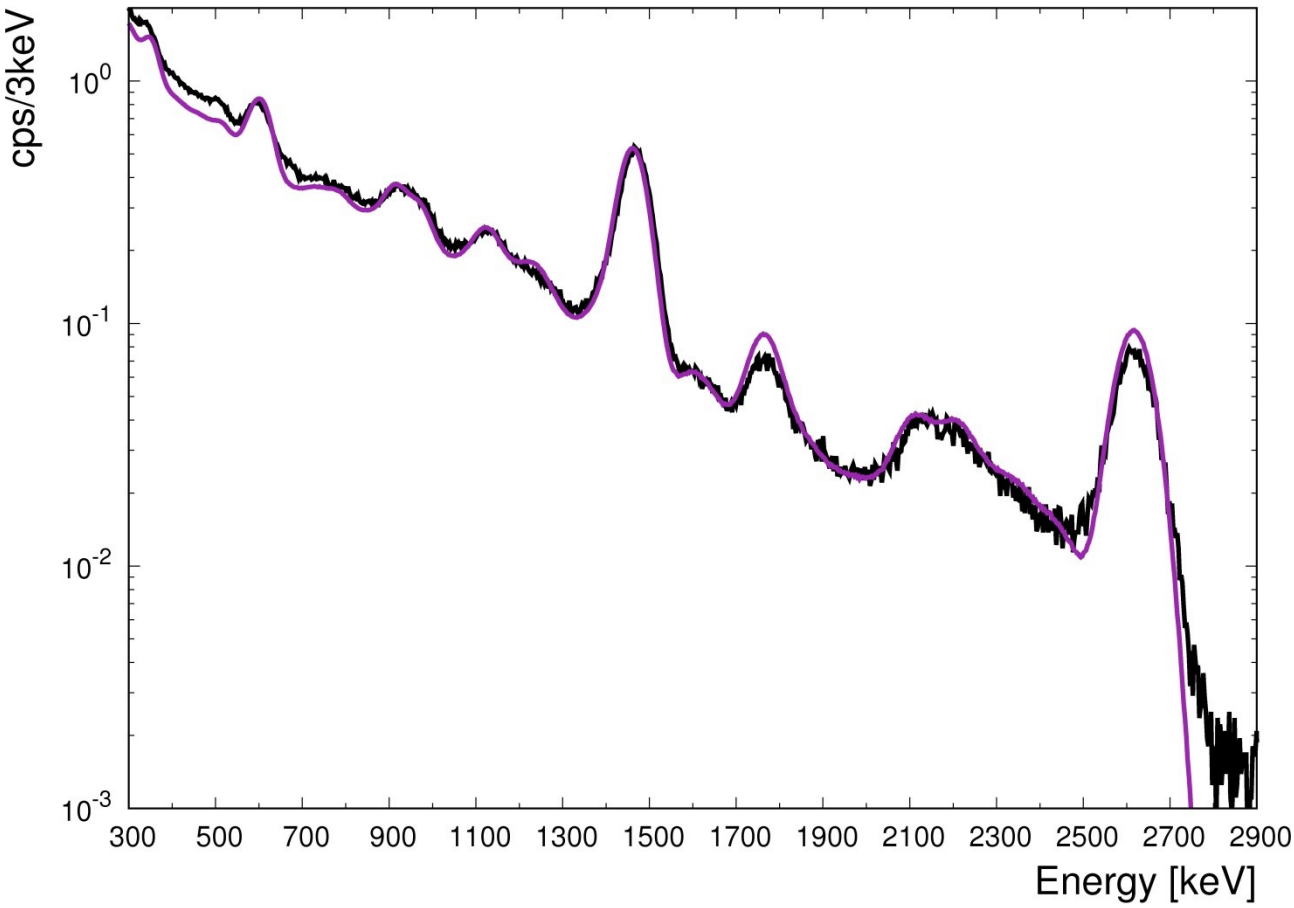

Figure 3.9. Gamma spectrum (black curve) acquired during the calibration day (w^{Cal} = (0.167 ± 0.008) kg/kg) and reconstructed spectrum (purple curve) obtained by applying the FSA-NNLS analysis with the simulated fundamental spectra. The reconstructed abundances are a_K = 1.63 10^{-2} g/g, a_U = 3.91 µg/g and a_{Th} = 10.92 µg/g.

3.1.4 Soil water content estimation

In this section a theoretical model relating the gamma signal to soil water content is derived both taking into account the specific soil composition of the experimental site and in terms of ready to use general formulae refereed to standard soil compositions. The capabilities of proximal gamma-ray spectroscopy in assessing soil water content are finally demonstrated by means of Monte Carlo simulations applied in the framework of a synthetic calibration.

3.1.4.1 Theoretical background

Soil is a complex system made up of a heterogeneous mixture of solid, liquid and gaseous phases. In the presence of a mixture, the mass attenuation coefficient *(μ/ρ)* (section 3.1.1) is obtained as the weighted sum of the mass attenuation coefficients of individual soil material constituents, i.e.

$$\left(\frac{\mu}{\rho}\right) = \sum_{i=1}^{n} a_i \left(\frac{\mu}{\rho}\right)_i \tag{3.8}$$

where a_i [kg/kg] is the mass abundance of the i-th soil material constituent and $\sum_{i=1}^{n} a_i = 1$.

Gamma-ray spectroscopy essentially treats soil as a two-phase medium in which the total mass *M* comprises a mass of solid constituents M^S (the largest portions typically due to the oxides SiO_2, Al_2O_3 and CaO) and a water mass, the latter partially distributed in soil matrix pores (M_{H2O}^{P}) and partially incorporated as structural water (M_{H2O}^{struct}) (Sun et al., 2009). By applying Eq. (3.8) to a wet soil it follows that:

$$\left(\frac{\mu}{\rho}\right) = \sum_{i=1}^{S} a_i \left(\frac{\mu}{\rho}\right)_i + a_{H2O^{struct}} \left(\frac{\mu}{\rho}\right)_{H2O} + a_{H2O^{p}} \left(\frac{\mu}{\rho}\right)_{H2O} \tag{3.9}$$

where the sum is extended over all the soil solid constituents (neglecting trace elements components).

Considering that the mineral components have comparable mass attenuation coefficients (Lovborg, 1984), which are significantly different from that of water, it is possible to split a water component and a solid component as follows:

$$\left(\frac{\mu}{\rho}\right) = \frac{M^S}{M}\left(\frac{\mu}{\rho}\right)_S + \frac{M_{H2O}^{struct} + M_{H2O}^{P}}{M}\left(\frac{\mu}{\rho}\right)_{H2O} \tag{3.10}$$

where $(\mu/\rho)_s$ corresponds to the mass attenuation coefficient of the soil solid portion.

The gamma signal *S(E)* [cps] measured for a photopeak energy *E* by a given detection system can be written as:

$$S(E) = \frac{C(E)}{\left(\frac{\mu}{\rho}(E)\right)} a_{rad} \tag{3.11}$$

where *C(E)* is a constant comprising the gamma yield [γ/(s kg)], an adimensional geometrical factor and a flux-to-signal effective cross section factor [counts/(γ m^2)], while a_{rad} is the mass abundance of the parent radionuclide [kg/kg].

Generally speaking, soil water content at time *t* can be inferred from gamma-ray spectroscopy measurements provided a detector calibration on the basis of a soil water content independent calibration measurement. The key for soil water content assessment is the ratio between the gamma signal measured at the calibration time (S^{Cal}), for which the soil water content is known, and the gamma signal measured at the time *t* (*S*). By adopting Eq. (3.10) and Eq. (3.11) (simplifying the notation for the implicit energy dependence), and by explicitly inserting the definition of radionuclide mass abundance and of soil mass it is possible to obtain:

$$\begin{aligned}\frac{S^{Cal}}{S} = \frac{C a_{rad}^{Cal}}{\left(\frac{\mu}{\rho}\right)^{Cal}} \frac{S^{Cal}}{S} = \frac{a^{Cal}}{a} \cdot \frac{\left(\frac{\mu}{\rho}\right)}{\left(\frac{\mu}{\rho}\right)^{Cal}} \\ = \frac{M_{rad}}{M^{Cal}} \cdot \frac{M}{M_{rad}} \cdot \frac{\frac{M^S}{M}\left(\frac{\mu}{\rho}\right)_S + \frac{M_{H2O}^{struct}}{M}\left(\frac{\mu}{\rho}\right)_{H2O} + \frac{M_{H2O}^{P}}{M}\left(\frac{\mu}{\rho}\right)_{H2O}}{\frac{M^S}{M^{Cal}}\left(\frac{\mu}{\rho}\right)_S + \frac{M_{H2O}^{struct}}{M^{Cal}}\left(\frac{\mu}{\rho}\right)_{H2O} + \frac{M_{H2O}^{PCal}}{M^{Cal}}\left(\frac{\mu}{\rho}\right)_{H2O}}\end{aligned} \tag{3.12}$$

By properly rearranging Eq. (3.12) we end up with:

$$\frac{S^{Cal}}{S} = \frac{M^s \left(\frac{\mu}{\rho}\right)_S + M_{H2O}^{struct} \left(\frac{\mu}{\rho}\right)_{H2O} + M_{H2O}^{P} \left(\frac{\mu}{\rho}\right)_{H2O}}{M^s \left(\frac{\mu}{\rho}\right)_S + M_{H2O}^{struct} \left(\frac{\mu}{\rho}\right)_{H2O} + M_{H2O}^{PCal} \left(\frac{\mu}{\rho}\right)_{H2O}} \tag{3.13}$$

We define the water-to-solid mass fraction *w** [kg/kg] as the ratio between the total water mass and the solid mass:

$$w^* = \frac{M_{H2O}^{P} + M_{H2O}^{struct}}{M^S} \tag{3.14}$$

which can be used to make explicit the water content dependence of Eq. (3.13) as follows:

$$\frac{S^{Cal}}{S} = \frac{\Psi + w^*}{\Psi + w^{*Cal}} \tag{3.15}$$

where

$$\Psi = \frac{\left(\frac{\mu}{\rho}\right)_S}{\left(\frac{\mu}{\rho}\right)_{H2O}} \tag{3.16}$$

and w^{*Cal} [kg/kg] is the water-to-solid mass fraction at the calibration time.

Finally, the water-to-solid mass fraction *w** at time *t* can be determined according to the following equation:

$$w^* = \frac{S^{Cal}}{S} \cdot \left(\Psi + w^{*Cal}\right) - \Psi \tag{3.17}$$

By adopting the specific composition of our experimental site (Table 3.3), we end up with the Eq. (3.18) and Eq. (3.19) referred respectively to the ^{40}K (1.46 MeV) and to the ^{208}Tl (2.61 MeV) gamma signals.

$$w_{40_K}^* = \frac{S_{40_K}^{Cal}}{S_{40_K}} \cdot \left(\Psi_{40_K} + w^{*Cal}\right) - \Psi_{40_K} = \frac{S_{40_K}^{Cal}}{S_{40_K}} \cdot \left(0.895 + w^{*Cal}\right) - 0.895 \tag{3.18}$$

$$w_{208_{Tl}}^* = \frac{S_{208_{Tl}}^{Cal}}{S_{208_{Tl}}} \cdot \left(\Psi_{208_{Tl}} + w^{*Cal}\right) - \Psi_{208_{Tl}} = \frac{S_{208_{Tl}}^{Cal}}{S_{208_{Tl}}} \cdot \left(0.908 + w^{*Cal}\right) - 0.908 \tag{3.19}$$

In the energy range of natural gamma emissions typically monitored in radiometric measurements (~ 1 MeV) soil solid constituents generally have comparable mass attenuation coefficients as a result of the dominating Compton scattering interaction, which cross section is proportional to the electron density. As soil major constituents (*Z*<30) have *Z/A* values close to 0.5 and considering that water has a fixed *Z/A* = 0.556, it turns out that the typical value for the Ψ coefficient is 0.90 (i.e. 1/1.11) as adopted by (Carroll, 1981; Grasty, 1997) in the processing of ^{40}K and ^{208}Tl photopeak signals from airborne radiometric surveys. Table 3.4 shows that the Ψ coefficient has some *Z* dependence, i.e. a site dependence related to the specific soil chemical composition, as well as a gamma energy dependence.

Table 3.4. Ratio Ψ between the mass attenuation coefficient of the soil solid portion to that of water (see Eq. (3.16)) for the major oxides constituting the soil material and for different standard soils. Ψ values are separately given for the ^{40}K (1.46 MeV) and ^{208}Tl (2.61 MeV) gamma energies.

Major oxides	Ψ(^{40}K)	Ψ(^{208}Tl)
Si_2O	0.900	0.910
Al_2O_3	0.884	0.893
CaO	0.903	0.927
Fe_2O_3	0.864	0.894
MgO	0.895	0.904
K_2O	0.883	0.908
Na_2O	0.872	0.880
TiO_2	0.861	0.882
MnO	0.844	0.875
Standard soils	**Ψ(^{40}K)**	**Ψ(^{208}Tl)**
Experimental site[1]	0.895	0.908
Beck[2]	0.906	0.916
Soil 1[3]	0.913	0.924
Soil 5[3]	0.889	0.905
Soil 2[3]	0.914	0.924
Nist SRM 2711[4]	0.895	0.907

[1]Table 3.3
[2](Beck et al., 1972)
[3](Jacob et al., 1994)
[4](Mackey et al., 2010)

In the framework of proximal gamma-ray spectroscopy applied to precision farming, the relevant fraction of water for irrigation purposes is the gravimetric water content w_G [kg/kg], defined as follows:

$$w_G = \frac{M_{H2O}^P}{M^s + M_{H2O}^{struct}} \tag{3.20}$$

which specifically refers to the amount of water at disposal to the crop system for its growth and sustenance. By applying the described method to the gravimetric water content, it is possible to derive an equation analogous to Eq. (3.17), which follows:

$$w_G = \frac{S^{Cal}}{S} \cdot \left(\Omega + w_G^{Cal}\right) - \Omega \tag{3.21}$$

where the adimensional factor Ω is given as:

$$\Omega = \Psi + (1 - \Psi) \cdot f_{H2O}^{struct} \tag{3.22}$$

and f_{H2O}^{struct} is the fraction of structural water [kg/kg], i.e. water incorporated in the formation of soil minerals, defined as:

$$f_{H2O}^{struct} = \frac{M_{H2O}^{struct}}{M^s + M_{H2O}^{struct}} \tag{3.23}$$

Considering that (Sun et al., 2009) report a value of structural water that is the (0.41 ± 0.29) mass fraction of LOI (i.e. loss of ignition) and combining with the median (0.03 kg/kg), 1st quartile (0.02 kg/kg) and 3rd quartile (0.058 kg/kg) LOI values reported in (Weynants et al., 2013), an average value of $f_{H2O}^{struct} = (0.012^{+0.030}_{-0.010})$[kg/kg] is obtained. By averaging Ψ values over standard soil compositions (Table 3.4), it is possible to derive two general formulas for the ^{40}K and ^{208}Tl gamma signals which can be used in case a detailed mineralogical soil analysis is missing.

$$w_{G\,40_k} = \frac{S_{40_K}^{Cal}}{S_{40_K}} \cdot \left(\Omega_{40_K} + w^{Cal}\right) - \Omega_{40_K} = \frac{S_{40_K}^{Cal}}{S_{40_K}} \cdot [(0.903 \pm 0.011) + w^{Cal}] - (0.903 \pm 0.011) \quad (3.24)$$

$$w_{G\,208_{Tl}} = \frac{S_{208_{Tl}}^{Cal}}{S_{208_{Tl}}} \cdot \left(\Omega_{208_{Tl}} + w^{Cal}\right) - \Omega_{208_{Tl}} = \frac{S_{208_{Tl}}^{Cal}}{S_{208_{Tl}}} \cdot [(0.915 \pm 0.009) + w^{Cal}] - (0.915 \pm 0.009) \quad (3.25)$$

3.1.4.2 Application of the method to Monte Carlo simulated spectra

In the framework of a "synthetic calibration", ^{40}K and ^{208}Tl Monte Carlo simulations are performed by adopting the soil composition and dry bulk density of the experimental site (section 3.1.3.1). Monochromatic monodirectional simulations considering a material made up by 100% water and by 100% soil solid phase are performed in order to reconstruct the water and solid mass attenuation coefficient (μ/ρ) for the 1.46 MeV (^{40}K) and 2.61 MeV (^{208}Tl) emission energies by applying the Beer-Lambert attenuation law. The obtained values are $(\mu/\rho)_{H2O}$ (1.46MeV) = 0.05825 cm^2/g, $(\mu/\rho)_S$ (1.46MeV) = 0.05211 cm^2/g, $(\mu/\rho)_{H2O}$ (2.61MeV) = 0.04268 cm^2/g and $(\mu/\rho)_S$ (2.61MeV) = 0.03874 cm^2/g, which provide the Ψ coefficients for ^{40}K and ^{208}Tl referred to the experimental site reported in Table 3.4 and adopted in Eq. (3.18) and Eq. (3.19).

Table 3.5. Results of the Monte Carlo validation test for the assessment of the water-to-solid mass fraction w* on the basis of ^{40}K and ^{208}Tl gamma signals. The first two columns report respectively the input w* and density values ρ of the simulated soil material. The output values in terms of overall soil mass attenuation coefficient μ/ρ, count rate for unitary radioelement abundance referred to dry soil conditions, and w* are reported for ^{40}K and ^{208}Tl gamma energies (see Eq. (3.18) and Eq. (3.19)).

INPUT		OUTPUT ^{40}K			OUTPUT ^{208}Tl		
w* [kg/kg]	ρ [g/cm^3]	μ/ρ [cm^2/g]	Count rate [cps]	w* [kg/kg]	μ/ρ [cm^2/g]	Count rate [cps]	w* [kg/kg]
0.045	1.345	0.0524	9.10	0.045	0.0389	0.364	0.045
0.094	1.390	0.0527	8.66	0.093	0.0391	0.346	0.092
0.167	1.449	0.0530	8.07	0.166	0.0393	0.323	0.165
0.261	1.516	0.0534	7.41	0.260	0.0396	0.297	0.258
0.372	1.583	0.0538	6.76	0.371	0.0398	0.271	0.369
0.571	1.680	0.0543	5.85	0.569	0.0402	0.235	0.567

The validation test covers water-to-dry fractions *w** ranging from dry soil condition up to saturation (Table 3.5), where for each configuration 10^{10} initial number of events are simulated and the wet bulk density is increased accordingly. Linear regressions between estimated and inputted water-to-dry fraction *w** (Figure 3.10) show that, for both ^{40}K and ^{208}Tl, the described method allows for determining *w** with an uncertainty <1%.

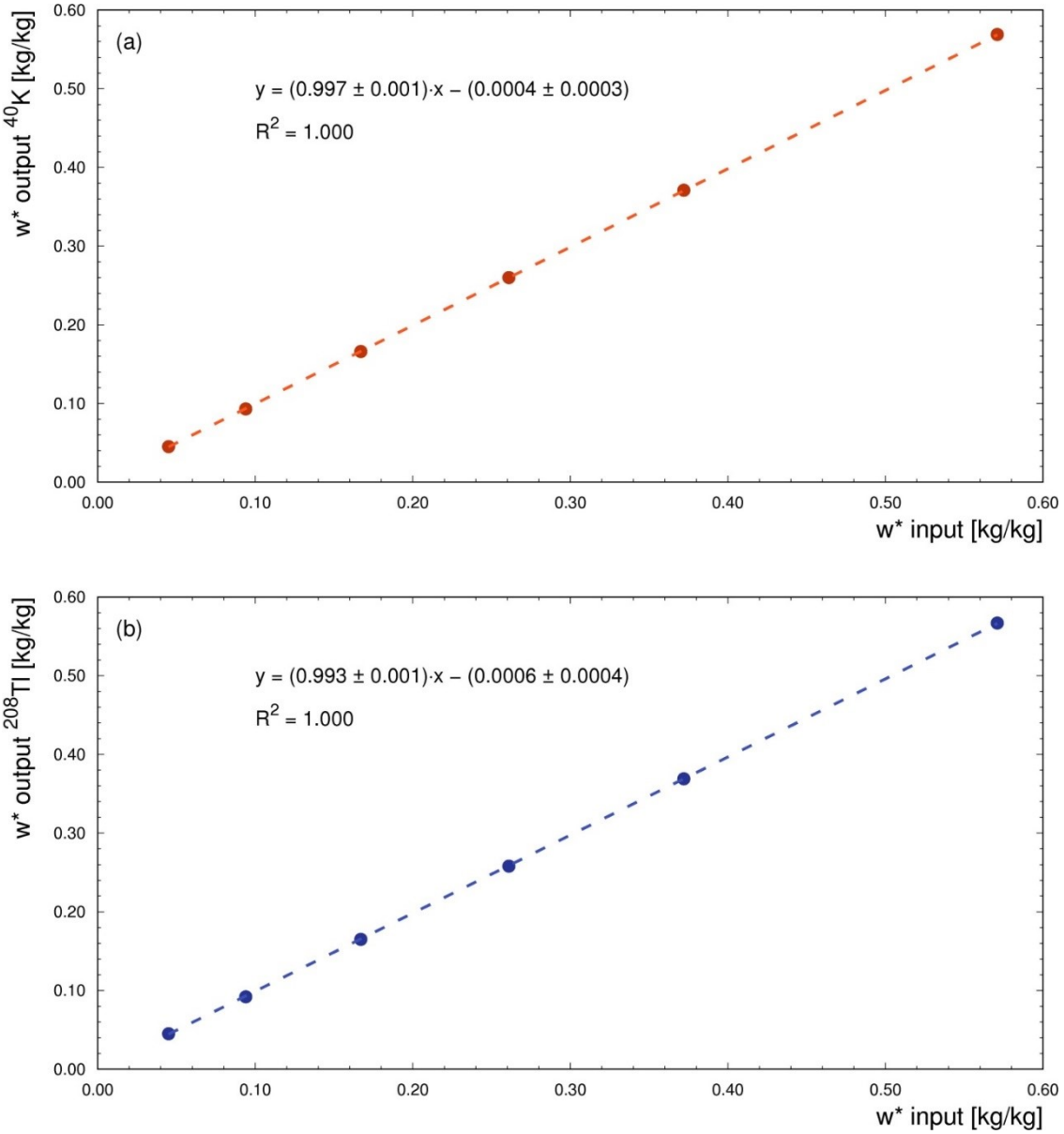

Figure 3.10. Linear regressions between water-to-solid mass fractions w* obtained as output of the Monte Carlo simulations for the ^{40}K (a) and ^{208}Tl (b) gamma energies versus input w* values used for building the Monte Carlo soil material (see Table 3.5).

The simulated detection system is expected to record for soil dry condition and radionuclide unitary abundances about 9.1 cps in the ^{40}K photopeak to be compared with 0.36 cps in the ^{208}Tl photopeak (Table 3.5). Since in natural contexts ^{208}Tl gamma emission is characterized by a lower gamma luminosity compared to that of ^{40}K and since detection efficiency decreases for increasing photon energy, comparable counting

statistics in the ^{40}K and ^{208}Tl photopeaks for unitary radionuclide abundances are obtained by integrating over acquisition times having a ratio of about 1:25 (see also Table 3.2).

Starting from soil in dry condition characterized by unitary radionuclide abundances, the addition of water leads to a dilution of the radionuclide concentration, an effective increase in soil density and an almost linear scaling of the spectral shapes. By increasing the water-to-dry fraction by a factor of 5, an average 32% reduction of the bin-by-bin counting statistics for both ^{40}K and ^{232}Th is observed (Figure 3.11).

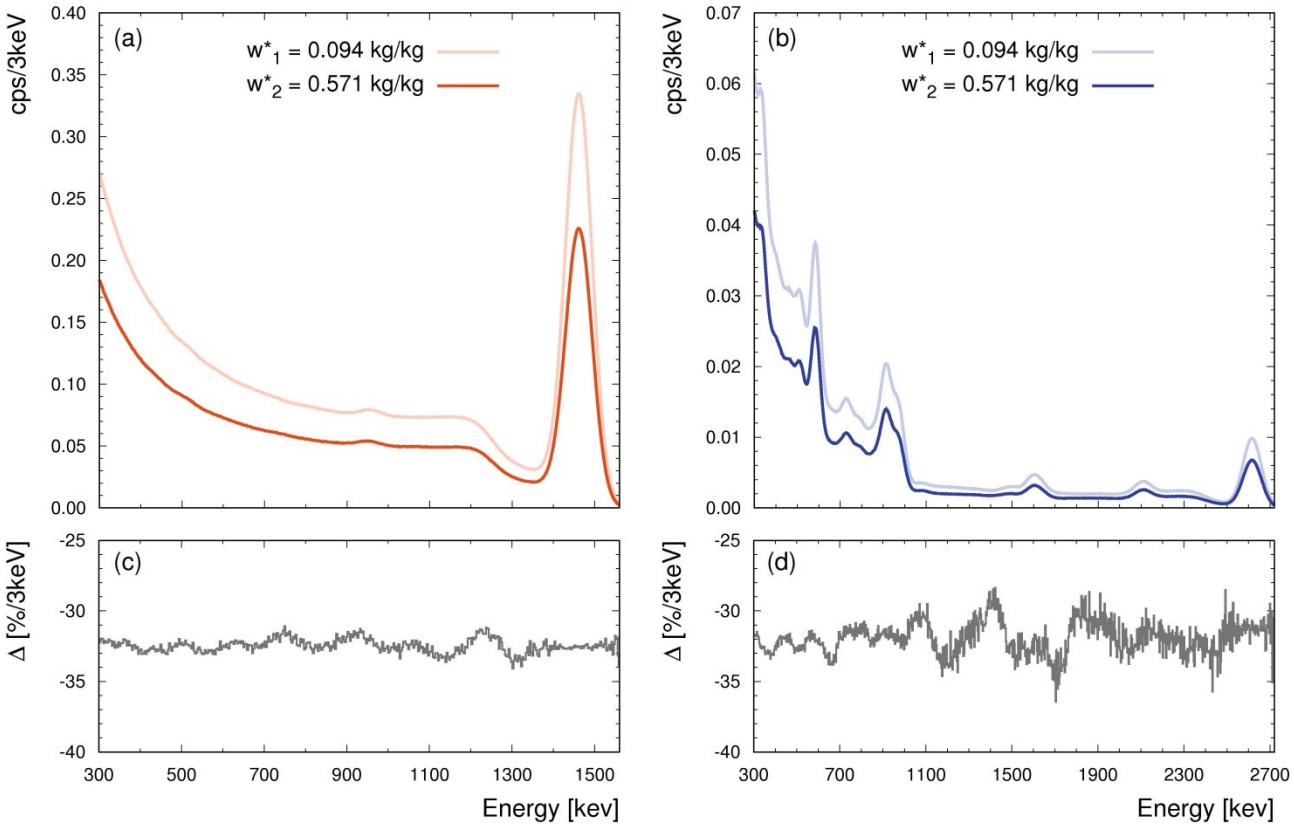

Figure 3.11. ^{40}K (a) and ^{232}Th (b) fundamental spectra referred to unitary radionuclide concentrations in dry soil condition and obtained via Monte Carlo simulations with 10^{10} gammas, assuming w^*_1 = 0.094 kg/kg and w^*_2 = 0.571 kg/kg (see Table 3.5). Bin-to-bin percentage differences (Δ) between fundamental spectra simulated with w^*_1 and w^*_2 are shown for ^{40}K (c) and ^{232}Th (d).

3.1.5 Conclusions

Proximal gamma-ray spectroscopy is being recognized as one of the best space-time trade off methods for a continuous and non-invasive determination of soil moisture dynamics and as an extraordinary joining link between punctual and satellite fields of view. However, the potentialities of the method have not been fully explored yet.

In this paper a Monte Carlo method is applied to the simulation of NaI gamma-ray spectra for soil water content estimation at field scale. The strength of this approach relies in the adoption of a two-steps strategy obtained by splitting the simulation into an equipment independent Photon Field Building (PFB), which simulates photon transport from the source to the detector position, and a Gamma Spectrum Reconstruction (GSR) process, devoted to the simulation of the employed detection system and of the recorded gamma spectra. This method allows for (i) the achievement of high simulated counting statistics with the potential for real time processing, (ii) calibrate for fundamental spectra produced by individual radionuclides, (iii) perform sensitivity studies for distinct environmental variables, e.g. soil moisture. In the

perspective of investigating variegated experimental scenarios, the high degree of customization provides an effective tool for feasibility and sensitivity studies. Different environmental conditions related to physical and chemical variables, distinct detection set ups and fields of view can be simulated.

The reliability of the method is effectively validated with gamma spectra measured by a permanent station installed at an agricultural experimental site, which is constituted by a 1L NaI detector placed at a height of 2.25 m, sensitive to an area having a ~25 m radius and to a depth of approximately 30 cm.

The developed theoretical model which relates soil water content to gamma signal according to an inverse proportionality law needs, in addition to the signal and water content values at calibration time, a soil dependent coefficient Ω. The energy dependent adimensional coefficient Ω combines the amount of structural water and the ratio Ψ between the mass attenuation coefficient of the soil solid portion to that of water. The latter, determined by Monte Carlo, is provided for the major soil oxides, which can be combined according to their mass abundance for retrieving site specific Ψ values. The Ω coefficient is provided both for the specific composition of the experimental site and for standard soils.

The theoretical model is applied in the framework of a Monte Carlo synthetic calibration, providing an excellent agreement in terms of linear regression between input and output soil water contents, inferred from simulated ^{40}K and ^{208}Tl gamma signals. By simulating 10^{10} initial events in the soil source, the $\sim 10^6$ reconstructed statistics inside the detector is affected by an uncertainty < 0.1%. The excellent results in terms of slope, intercept and coefficient of determination values demonstrate the capability of the proposed method in estimating soil water content with an average uncertainty < 1%.

3.2 Biomass water content effect on soil moisture assessment via proximal gamma-ray spectroscopy

Once the relation between soil water content and gamma signal is known, it must be corrected for the presence of growing vegetation beneath the detector position. Airborne gamma-ray spectroscopy already raised the attention on the attenuating effects on the gamma signal due to the presence of vegetation (Dierke and Werban, 2013; Norwine et al., 1979; Sanderson et al., 2004; Wilford et al., 1997): in the case of proximal surveys the presence of biomass in terms of plants, leaves and fruits is expected to play a much more critical role, and therefore there is an evident need for a more quantitative estimate of the signal reduction.

In the case of proximal gamma-ray measurements at agricultural sites, the physical and chemical properties of the soil as well as the soil radioactive content can be considered almost stationary, or at least sufficiently under control. The same is not true for the crop system which evolution is highly dynamic and is affected by variable climatic conditions and irrigation management practices. Indeed, the presence of growing vegetation introduces a sizable extra attenuation due to the Biomass Water Content (BWC), which varies in time during the crop life-cycle and is in principle undistinguishable from that generated by an increase in soil water content (SWC). In this perspective, a reliable correction for the BWC shielding is mandatory in order to avoid a systematic overestimation of SWC.

The gamma signal attenuation due to biomass is modelled with a Monte Carlo-based approach in terms of an equivalent water layer which thickness varies in time as the crop evolves during its life-cycle. I demonstrate that a permanent gamma station installed at an agricultural field can reliably probe the water content of the top soil only if systematic effects due to the biomass shielding are properly accounted for. I compared the biomass corrected experimental values of soil water content inferred from radiometric

measurements with gravimetric data acquired under different soil moisture levels, resulting in an average discrepancy of about 3% in bare soil condition and of 4% during the vegetated period. The temporal evolution of corrected soil water content values exhibits a dynamic range coherent with the soil hydraulic properties in terms of wilting point, field capacity and saturation.

3.2.1 Material and methods

In the following section we briefly present a geographical and climatic setting of the experimental site and a characterization of the main physical-chemical properties of the soil. The gamma and agro-meteorological stations are described together with the data acquisition methods. The gravimetric sampling campaign performed on soil and biomass samples is described along with the obtained results.

3.2.1.1 Experimental site

The experiment was conducted in the period 4th of April – 2nd of November 2017 at a tomato field of the Acqua Campus, a research center of the Emiliano-Romagnolo Canal (CER) irrigation district in the Emilia Romagna region in Italy (44.57° N, 11.53° E; 16 m above sea level) (Figure 3.12). According to the Köppen-Geiger climate classification (Peel et al., 2007), this geographical area is classified as Cfa (i.e. temperate, without dry season and with hot summer); its average annual temperature is 14 °C and rainfall is 700 mm.

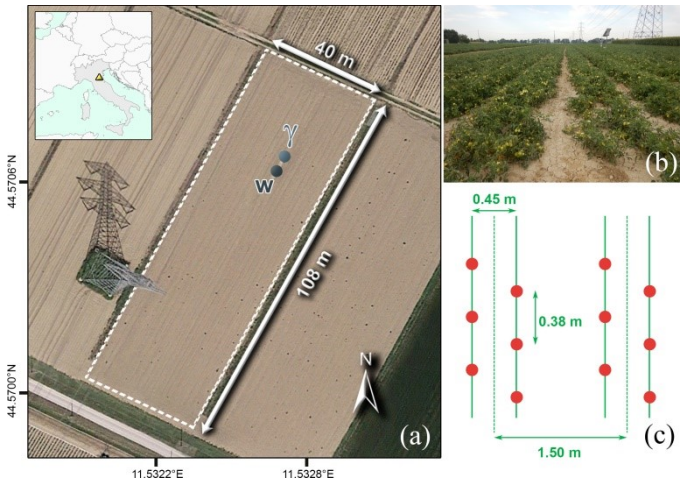

Figure 3.12. Panel (a), geographic location of the experimental site where the field dimensions and the positions of the gamma (γ) and agro-meteorological (w) stations are reported (cartographic reference system WGS 84). Panel (b), picture of the tomato plants rows; panel (c), schematic diagram of their disposition.

About 24% of the agricultural territory in Emilia Romagna, one of the richest regions of Italy and Europe, is devoted to irrigated agriculture, which plays a major role in the regional economy (Munaretto and Battilani, 2014). In particular, Emilia Romagna is the Italian region having the largest surface of land cultivated with tomatoes, one of the most water-demanding crops among vegetables, and contributes for about one third of the tomato national production (ISTAT, 2017).

The physical parameters of the soil, classified according to a loamy texture and a 1.26% organic matter content, are listed in Table 3.6. The hydraulic properties in terms of wilting point (0.07 kg/kg), field

capacity (0.24 kg/kg) and saturation (0.36 kg/kg) were inferred from volumetric soil water content values reported in (Strati et al., 2018).

Table 3.6. Physical parameters of the experimental site soil for the [0 – 30] cm depth horizon.

Parameter	Value
Sand [%]	45
Silt [%]	40
Clay [%]	15
Soil bulk density [kg/m^3]	1345

Tomato plants were transplanted on the 23rd of May with a row and plant spacing as shown in Figure 3.12, which corresponds to a 3.5 plants/m^2 density, and harvested on the 14th of September. The crop phenological growth stages of anthesis and maturity, together with the planting and harvesting dates, are indicated in panel (a) of Figure 3.14. Irrigation water was delivered by a sprinkler system, following a schedule based on the criteria provided by the decision support tool of IRRINET (Munaretto and Battilani, 2014).

3.2.1.2 Experimental setup

The experimental setup is composed of a gamma spectroscopy station and a commercial agro-meteorological station (MeteoSense 2.0, Netsens) both powered by solar panels and provided with an internet connection (Figure 3.13).

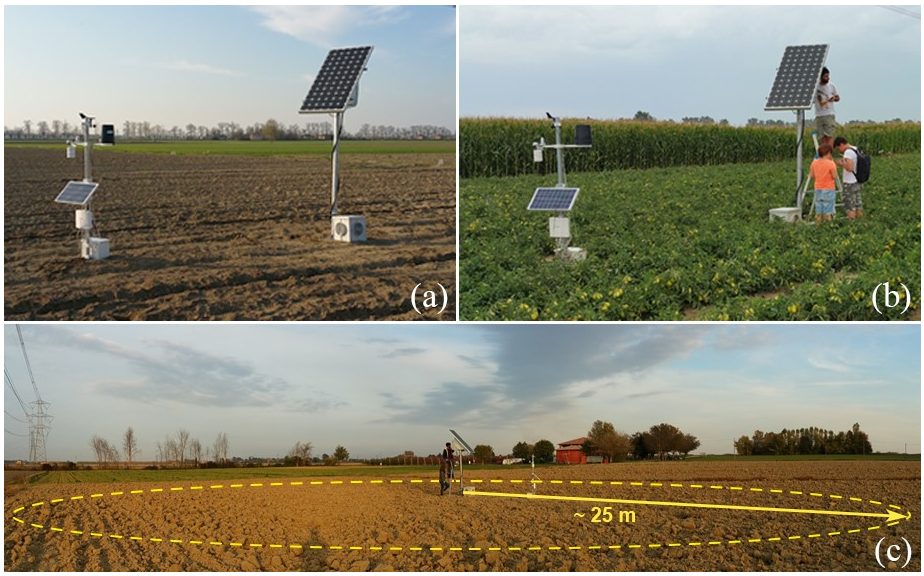

Figure 3.13. Panel (a) and (b) show the gamma and weather stations installed at the experimental site respectively in bare soil condition and during the vegetated period. Panel (c) illustrates a schematic representation of the gamma-ray spectrometer horizontal field of view at 2.25 m height: 95% of the detected signal comes from an area having radius of ~25 m.

The gamma station was specifically designed and built for the purpose of this experiment: its external structure is made up of steel and comprises a steel box welded on top of a 2.25 m high pole which hosts a 1L sodium iodide (NaI(Tl)) gamma-ray spectrometer (Baldoncini et al., 2018a). The crystal is coupled to a photo-multiplier tube base which output is processed by a digital Multi-Channel Analyzer (MCA, CAEN γstream) having 2048 acquisition channels. At a height of 2.25 m about 95% of the detected gamma signal is produced within a cone having base radius of approximately 25 meters (Feng et al., 2009) (Figure 3.13).

The MCA is complemented with a small integrated computer which provides the necessary hardware interface to the detector and runs the software required for managing the acquisition parameters, namely the start time, the acquisition dynamics in terms of spectral gain [keV/ch], and the operating high voltage. Additional software was developed to make the data-taking continuous and more resilient to some hardware related failures like accidental restarts or power shortages.

Measured weather data include air temperature, relative air humidity, wind direction and speed, precipitation and Short Wave Incoming Radiation (SWIR). Figure 3.14 shows the daily values of Minimum and Maximum Temperatures (T_{min} and T_{max}), ranging in the T_{min} = [1.3 - 22.7] °C and T_{max} = [13.5 - 39.3] °C intervals (panel a), the SWIR (ranging from 34.7 to 257.3 W/m^2) (panel b), the daily rainfall amount (up to a maximum of 56.2 mm) and irrigation water (up to a maximum of 35 mm) (panel c). The evapotranspiration (ET0, panel b) is calculated with the Hargreaves method (Hargreaves and Samani, 1985) using weather data recorded by the agro-meteorological station. During the last ten years (2008 - 2017) local meteorological archives (Arpae) recorded a mean total rainfall in the same period of 384.3 mm, a mean daily minimum temperature of 13.2 °C and a mean daily maximum temperature of 26.3 °C.

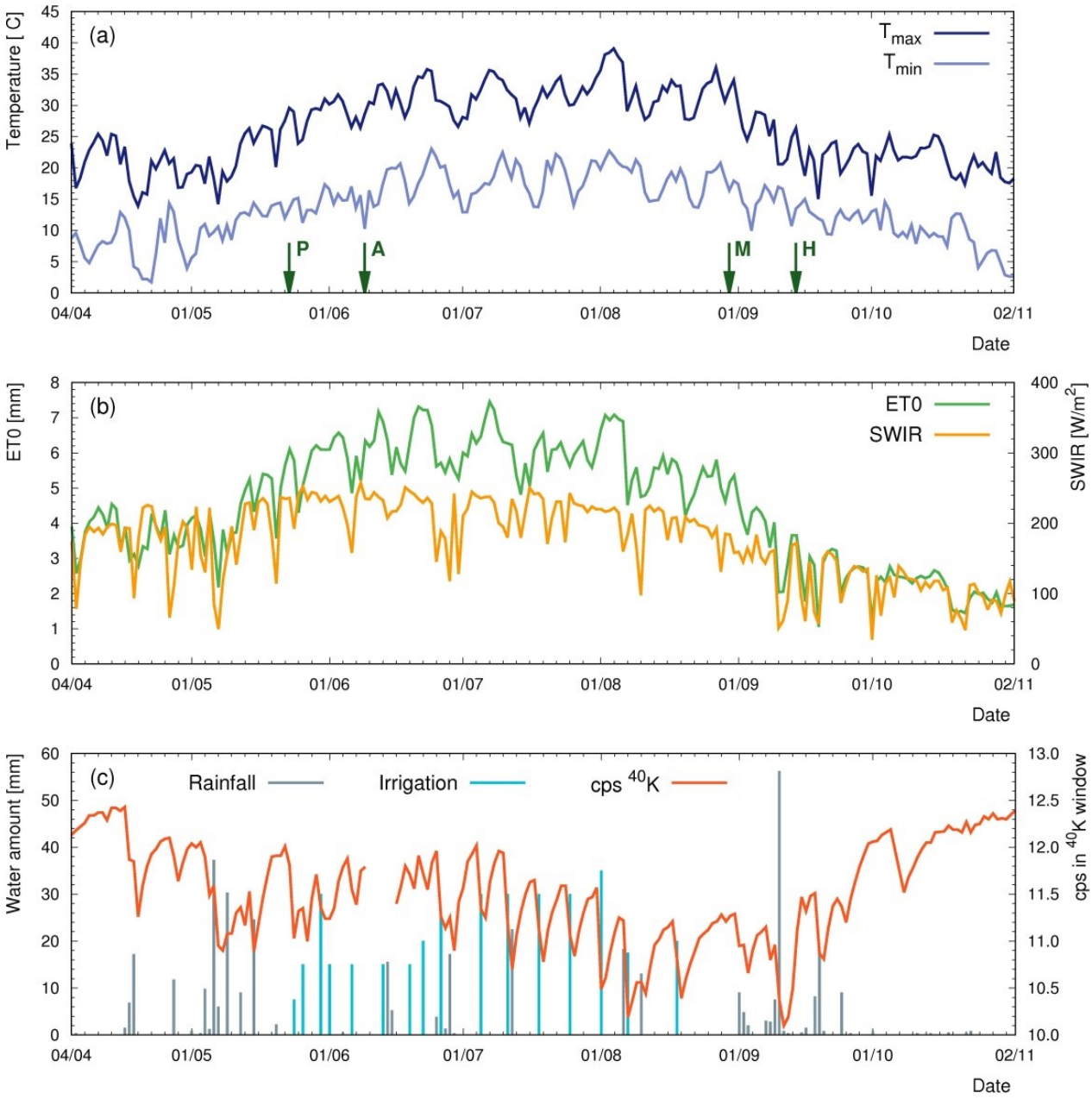

Figure 3.14. Daily meteorological and gamma data. In panel (a), maximum (T_{max}) and minimum (T_{min}) temperatures; the arrows indicate the crop stages of planting (P), anthesis (A), maturity (M) and harvesting (H). In panel (b), reference crop evapotranspiration (ET0) and Short Wave Incoming Radiation (SWIR). In panel (c), amount of rainfall and irrigation water and daily average counts per second (cps) in the ^{40}K gamma photopeak energy window.

3.2.1.3 Data acquisitions: gravimetric and gamma-ray measurements

Gravimetric measurements were carried out on bulk soil samples as means to both calibrate and validate the soil water content estimation based on proximal gamma-ray spectroscopy. Five sets of gravimetric measurements were performed: a calibration and a validation sets in bare soil condition respectively on the 18th of September and on the 21st of September (two days after a rainfall event) and three validation sets in presence of the tomato crop and in different soil moisture conditions, i.e. one Day Before Irrigation (DBI) (24th of July), one (26th of July) and three (28th of July) Days After Irrigation (DAI), referred to the same event (Table 3.7).

Samples were collected by using a soil-auger following a sampling scheme (Figure 3.15) including 16 planar sampling points and covering homogeneously the area within a ~15 m radius from the gamma station position from which about 85% of the detected signal is produced (Figure 2 of (Baldoncini et al., 2018a)).

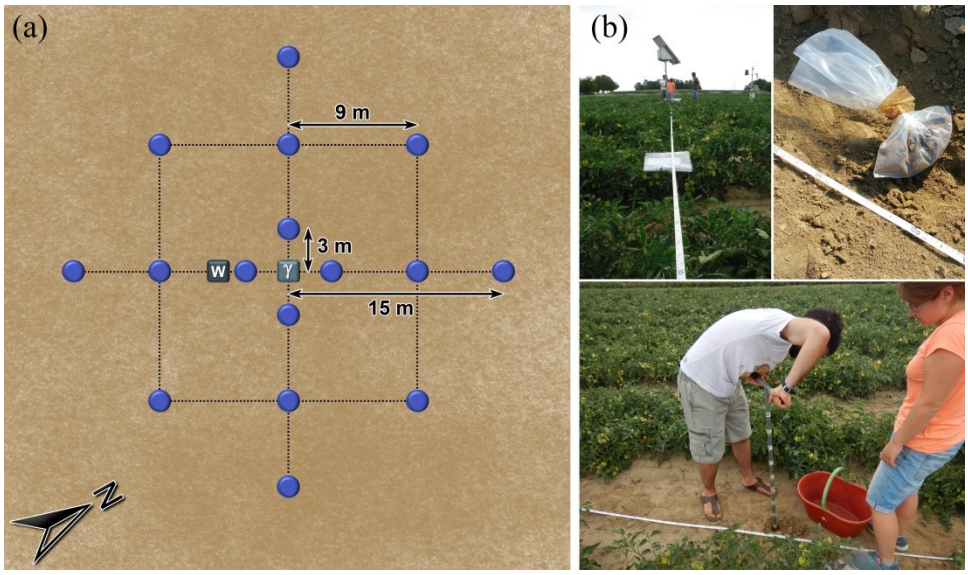

Figure 3.15. Panel (a), scheme of the soil gravimetric sampling campaign with the 16 collection points and their relative distances to the gamma (γ) and agro-meteorological (w) stations. Panel (b), different stages of the sampling procedure.

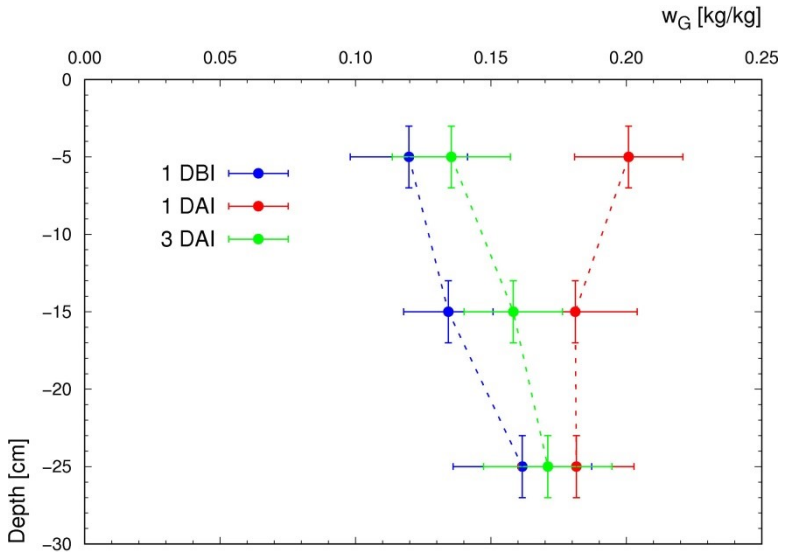

Figure 3.16. Individual gravimetric soil water contents for the [0 – 10] cm, [10 – 20] cm and [20 – 30] cm depth horizons are reported in terms of mean and standard deviation of the corresponding 16 samples for the three sets of measurements performed in the vegetated period: 1 Day Before Irrigation (DBI) (24/07/17), 1 and 3 Days After Irrigation (DAI) (26/07/17 and 28/07/17). Each data point is referred to the median depth, characterized by a 2 cm sampling uncertainty.

For each sampling planar position three samples were collected respectively in the [0 – 10] cm, [10 – 20] cm and [20 – 30] cm depth horizons for a 48 total number of samples for each set.

The results of the measurements (Figure 3.16) show a monotonically increasing trend in water content for increasing depth for the 1 DBI and 3 DAI depth profiles, which is reversed for the 1 DAI validation set. Among the three datasets the deepest soil horizon exhibits a much less pronounced variation in soil water content compared to the superficial layers.

Above-ground crop biomass samples were collected at four different maturity stages in order to evaluate the overall water mass per plant of stems, leaves and fruits according to standard operating procedures (SERAS, 1994) and by using the destructive sampling method (Catchpole and Wheeler, 1992).

The BWC (mm) data were derived after the water mass per plant (kg/plant) measurements, adopting the specific density of 3.5 plants/m^2, and linearly fitted to obtain the BWC temporal evolution over the vegetated period (Figure 3.17).

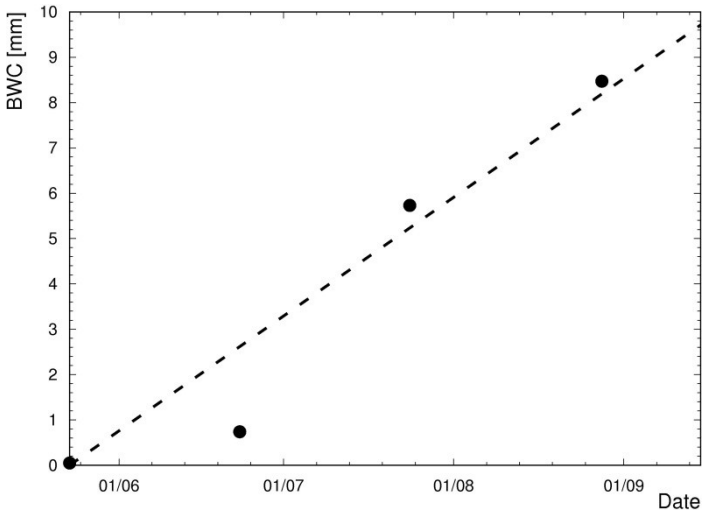

Figure 3.17. Overall Biomass Water Content (BWC) estimated from destructive gravimetric measurements on stems, leaves and fruits samples collected at four different stages of the tomato crop. Data were fitted according to a linear regression curve with a 0.084 [mm/day] slope and a 0.921 coefficient of determination.

The gamma-ray spectrometer detects the photon radiation produced in the decays of natural occurring radionuclides (^{40}K, ^{238}U and ^{232}Th) and records a list mode output, i.e. a continuous logging of individual photons arrival time and acquisition channel. A dedicated software was developed to post-process the output list mode files in order to (i) generate gamma spectra corresponding to 15 minutes acquisition time, (ii) perform an energy calibration procedure, (iii) remove the spectral background, and (iv) retrieve the net count rate in the main ^{40}K, ^{214}Bi (^{238}U) and ^{208}Tl (^{232}Th) photopeak energy windows (IAEA, 2003). Average net count rates are 11.51 cps in the ^{40}K energy window (1.37 – 1.57 MeV), 0.89 cps in the ^{214}Bi energy window (1.66 – 1.86 MeV) and 2.49 cps in the ^{208}Tl energy window (2.41 – 2.81 MeV), while the gross counting statistics in the [0.30 – 3.00] MeV range is of about 200 cps. While ^{40}K and ^{208}Tl are distributed only in the soil, ^{214}Bi gamma radiation has an atmospheric component due to the exhaled ^{222}Rn gas which makes the ^{214}Bi count rate inadequate for soil water content estimation as it visibly fluctuates in the day-time and in relation to rainfall events (Barbosa et al., 2017). For this reason, we chose ^{40}K as natural gamma emitter for soil water content assessment purposes, given also the highest net counting statistics in its photopeak.

Thanks to a specifically developed management software, gamma and meteorological data were temporally aligned and merged in a unique database having a 15 minutes temporal resolution and 44 different fields (34 related to gamma measurements and 10 to meteorological measurements). Data were hourly averaged and a statistical fluctuation typically lower than 1% is observed in the net number of events. The global dataset has 20502 entries corresponding to a 5125 hours acquisition time during which both the gamma and agro-meteorological stations were operative, for a 260 GB total amount of raw data.

3.2.2 Soil water content estimation

3.2.2.1 Theoretical background

The inverse proportionality between soil moisture and gamma signal is the key point suggesting that gamma-ray spectroscopy can be an operative method for retrieving SWC (Carroll, 1981; Grasty, 1997). (Baldoncini et al., 2018a) provides by means of Monte Carlo simulations a proof of concept of the effectiveness and reliability of proximal gamma-ray spectroscopy for the determination of the gravimetric SWC, w_G (kg/kg).

The SWC at time t can be determined by monitoring the counting statistics of a gamma spectrum in the photopeak of energy E_i (Baldoncini et al., 2018a) as:

$$w_\gamma^i(t) = \frac{S^{Cal}(E_i)}{S(E_i,t)} \cdot \left(\Omega(E_i) + w_G^{Cal}\right) - \Omega(E_i) \tag{3.26}$$

where

- $S(E_i,t)$(cps) is the net count rate in the photopeak of energy E_i at time t;
- $S^{Cal}(E_i)$(cps) is the net count rate in the photopeak of energy E_i at the calibration time;
- w_G^{Cal}(kg/kg) is the SWC determined on the basis of independent measurements at the calibration time.

The adimensional factor $\Omega(E_i)$ is defined as:

$$\Omega(E_i) = \Psi(E_i) + [1 - \Psi(E_i)] \cdot f_{H2O}^{struct} \tag{3.27}$$

where f_{H2O}^{struct}(kg/kg) is the fraction of structural water (i.e. water incorporated in the formation of soil minerals) and $\Psi(E_i)$ corresponds to the ratio between the mass attenuation coefficient of the soil solid portion $\left(\frac{\mu}{\rho}\right)_S$ (cm^2/g) to the mass attenuation of water $\left(\frac{\mu}{\rho}\right)_{H2O}$ (cm^2/g):

$$\Psi(E_i) = \frac{\left(\frac{\mu}{\rho}(E_i)\right)_S}{\left(\frac{\mu}{\rho}(E_i)\right)_{H2O}} \tag{3.28}$$

By adopting the specific values referred to the composition of the soil at the experimental site (Baldoncini et al., 2018a), Eq. (3.26) can be numerically written for the ^{40}K photopeak (1.46 MeV) as:

$$w_{\gamma\,K} = \frac{S_K^{Cal}}{S_k(t)} \cdot \left(0.899 + w_G^{Cal}\right) - 0.899 \tag{3.29}$$

In absence of a detailed mineralogical analysis, a Ω = (0.903 ± 0.011) mean value can be employed (Baldoncini et al., 2018a). In any case, the uncertainty on the estimated SWC is typically dominated by the

systematic uncertainty on the S_K^{Cal} and w_G^{Cal} calibration reference values, implying an almost negligible contribution from the Ω variability to the ~0.017 kg/kg absolute uncertainty.

In order to extract time-by-time SWC values from proximal gamma-ray spectroscopy measurements it is necessary to take into account a non-constant correction due to the presence of growing vegetation beneath the detector position (Figure 3.13). Indeed, as the tomato plants mature, the gamma spectrometer receives a progressively reduced gamma flux due to the shielding effect produced by the crop system. The latter can be estimated by modelling stems, leaves and fruits as an equivalent water layer characterized by a given thickness which we express as a BWC in units of mm (Figure 3.17). In particular, the time dependent correction to be applied to the measured gamma signal *S* can be expressed as the Λ ratio given in:

$$\Lambda_K(BWC)\left[\frac{cps}{cps}\right] = \frac{S_K^{MC}(BWC)}{S_K^{MC}(BWC=0)} \tag{3.30}$$

It follows that the SWC corrected for the attenuation due to the vegetation $w_{\gamma\,K}^{\Lambda}$ at time t is given by:

$$w_{\gamma\,K}^{\Lambda} = \frac{S_K^{Cal}\cdot\Lambda_K\big(BWC(t)\big)}{S_k(t)}\cdot\left(0.899+w_G^{Cal}\right)-0.899 \tag{3.31}$$

With the aim of going after the crop evolution temporal profile, a curve describing the attenuation factor Λ(BWC) as function of the BWC was determined by adopting the Monte Carlo simulation method described in (Baldoncini et al., 2018a) (Figure 3.18 panel a). Nine independent simulations were performed by progressively increasing the thickness of the equivalent water layer from BWC = 0 mm up to BWC = 20 mm with steps of 2.5 mm. Simulations were carried out with an initial statistics of 10^9 emitted photons having 1.46 MeV energy and assigning to the soil source a SWC corresponding to w_G^{Cal}. The nine Λ(BWC) values were fitted according to a linear regression curve with an intercept fixed by definition to 1 (Figure 3.18 panel a).

In order to estimate how the attenuation due to vegetation affects the estimation of SWC, we evaluate on the basis of the Monte Carlo results the quantity δ defined as:

$$\delta(BWC)[\%] = 100\cdot\frac{w_{\gamma\,K}^{\Lambda}-w_G^{Cal}}{w_G^{Cal}} \tag{3.32}$$

where:

$$w'_{\gamma\,K} = \frac{S_K^{Cal}}{S_K^{Cal}\cdot\Lambda(BWC)}\cdot\left(0.899+w_G^{Cal}\right)-0.899 = \frac{1}{\Lambda(BWC)}\cdot\left(0.899+w_G^{Cal}\right) \tag{3.33}$$

that corresponds to the SWC that would have been measured without correcting for BWC for fixed w_G^{Cal} in the soil. As shown in Figure 3.18 panel b, the non-corrected SWC $w'_{\gamma\,K}$ differs from the w_G^{Cal} = 0.163 kg/kg calibration value (Table 3.7) by about 70% for a BWC of 7.5 mm, almost reproducing the BWC at the tomato harvesting (Figure 3.17). Therefore, neglecting the application of a vegetation correction factor Λ(BWC) to the measured gamma signal has a large systematic effect on the SWC retrieving in proximal gamma-ray spectroscopy (Figure 3.19).

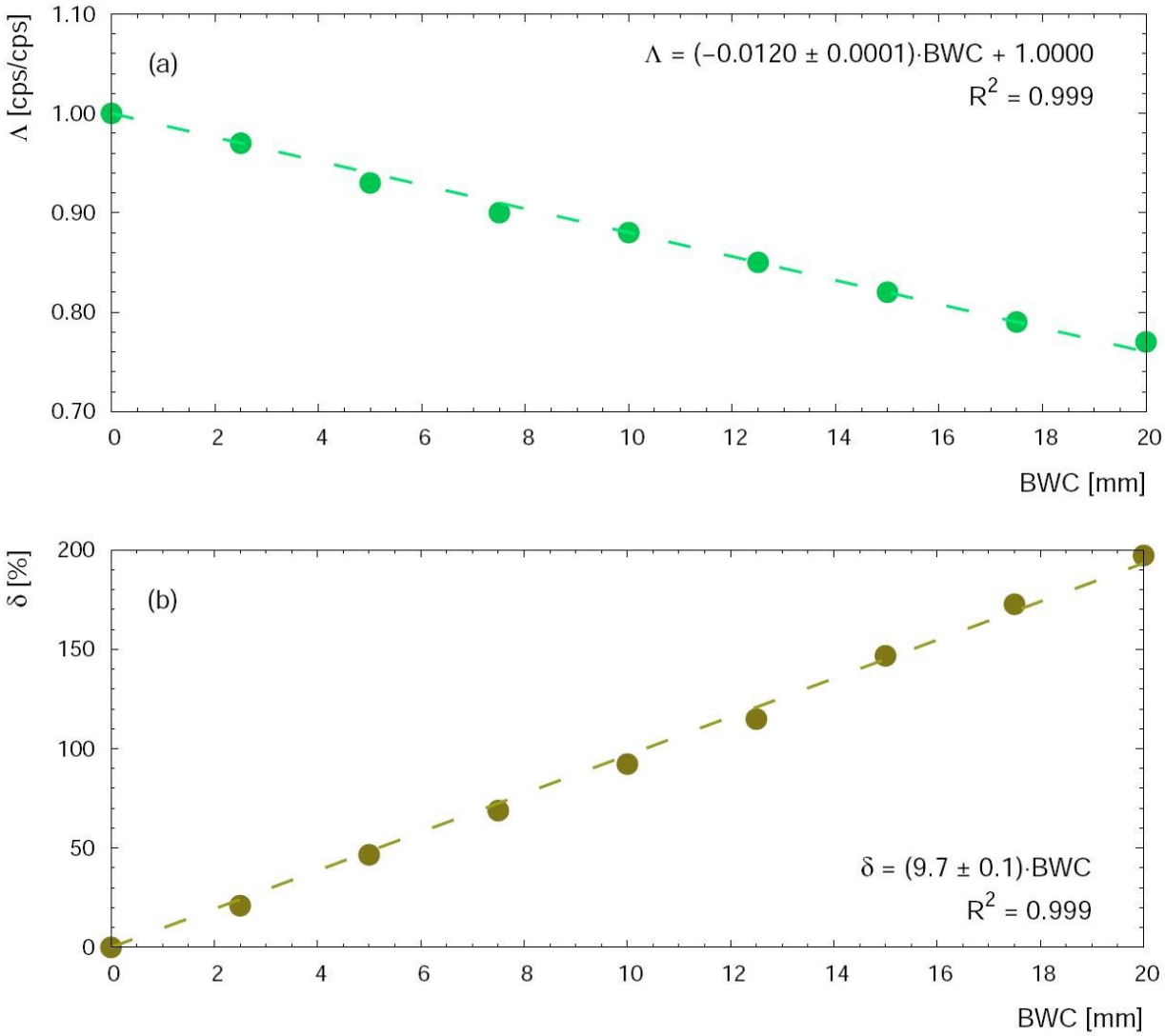

Figure 3.18. Panel (a), simulated values of Λ (Eq. (3.30)) for the 1.46 MeV ^{40}K gamma emission energy as function of the BWC, t fitted with a linear regression curve. Panel (b), percentage overestimation δ (Eq. (3.32)) of the SWC as function of the BWC in case no vegetation cover correction is applied.

3.2.2.2 Experimental result and validation

The theoretical approach presented in Section 3.2.2.1 was applied to the analysis of gamma-ray spectra measured over the entire data taking period, which comprises a vegetated phase accounting for 54% of the duty cycle. As detailed in Section 3.2.1.3, a gravimetric sampling campaign was performed with the objective of both calibrating and validating the SWC estimation based on ^{40}K radiometric data: the results of this procedure are reported in Table 3.7. The [0–10] cm, [10–20] cm, and [20–30] cm w_G values were combined with weights respectively equal to 0.79, 0.16, and 0.05, determined on the basis of the gamma signal depth profile (Figure 5 of (Strati et al., 2018)). Particular attention was paid in collecting soil samples in different environmental conditions in terms of both temporal proximity to irrigation events and of amount of biomass. This sampling strategy allowed for testing the reliability of the proximal gamma-ray spectroscopy method as well as for having insights on the bias that the BWC has on the SWC estimation.

Table 3.7. Results of SWC (w_G) for the gravimetric calibration measurement (18 September, one day before a rainfall event) and for four validation measurements. The latter were performed in bare soil condition (21 September, two days after a rainfall event) and during the vegetated period, one day before an irrigation event (24 July), one (26 July) and three days (28 July) after the same event. The w_G values are the weighted average SWC determined from 16 planar sampling points homogeneously distributed within 15 m from the gamma station. For each measurement we report the SWC inferred from proximal gamma-ray spectroscopy measurements without ($w_{\gamma K}$) and with BWC correction ($w^{\Lambda}_{\gamma K}$) together with the corresponding 1σ uncertainty. Δw and Δw^{Λ} are the percentage differences between w_G and $w_{\gamma K}$ and between w_G and $w^{\Lambda}_{\gamma K}$, respectively.

Date	w_G[kg/kg]	$w_{\gamma K}$ [kg/kg]	$w^{\Lambda}_{\gamma K}$ [kg/kg]	Δw[%]	Δw^{Λ}[%]
18 September	0.163 ± 0.008	0.163 ± 0.017	0.163 ± 0.017	0.0	0.0
21 September	0.176 ± 0.011	0.182 ± 0.017	0.182 ± 0.017	3	3
24 July	0.124 ± 0.021	0.196 ± 0.017	0.126 ± 0.017	58	2
26 July	0.197 ± 0.021	0.256 ± 0.017	0.181 ± 0.017	30	-8
28 July	0.141 ± 0.021	0.203 ± 0.017	0.133 ± 0.017	44	-6

In bare soil condition (21st of September) the correction of BWC plays no role, as the value of the attenuation function Λ is identical to 1 for null BWC (see Eq. (3.30)). On the other hand, the three validation measurements performed in July allow for investigating the effect of the BWC correction as the tomato crop was at about midlife of its growing cycle. By neglecting the attenuation due to the presence of BWC (see Eq. (3.29)), the $w_{\gamma K}$ is affected by a systematic positive bias larger than 30%. By accounting for the attenuation effect of BWC (see Eq. (3.31)), an excellent agreement between $w^{\Lambda}_{\gamma K}$ and w_G is obtained, with a maximum discrepancy below 10% and a 1σ level agreement for all the three validation measurements. Systematic errors leading to underestimations or overestimation of the SWC are to be excluded also in presence of the tomato crop at the experimental site.

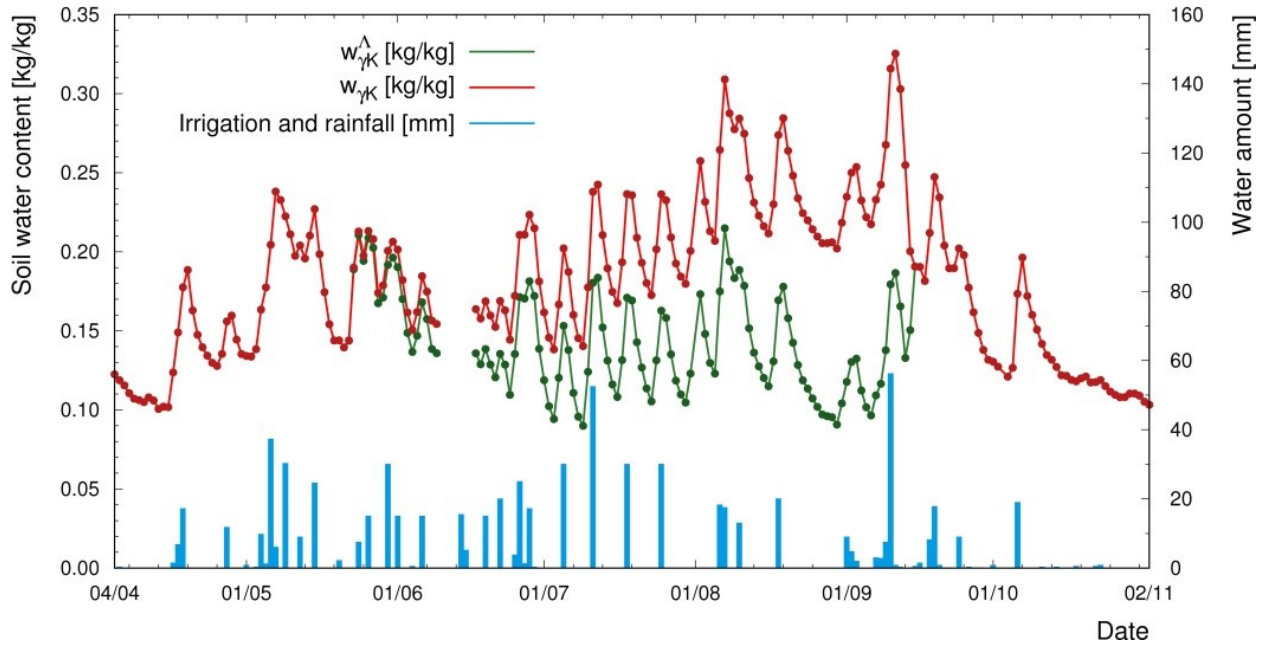

Figure 3.19. SWC inferred from measured ^{40}K count rate without ($w_{\gamma K}$, see Eq. (3.29)) and with ($w^{\Lambda}_{\gamma K}$, see Eq. (3.31)) BWC correction for the entire data taking period.

As the BWC changes in time as the tomato crop grows, a non-constant BWC correction was applied to gamma signals over the entire tomato life cycle, where the correction temporal evolution was estimated on the basis of the BWC temporal growth (see Figure 3.17). Figure 3.19 shows a positive correlation between radiometric inferred SWC and the amount of precipitations that includes both rainfall and irrigation water. Nevertheless, the $w^{\Lambda}_{\gamma K}$ and $w_{\gamma K}$ datasets exhibit significantly different dynamic ranges which interpretation

requires a comparison with the soil hydraulic properties, typically used as reference for defining crop water demand. Without the BWC correction, the systematic bias can lead to non-physical results corresponding to SWC frequently exceeding soil field capacity and sometimes close to saturation (see Section 3.2.1.1) as the crop maturity stage is approached (Figure 3.19). During the vegetated period, $w_{\gamma}^{\Lambda}{}_{K}$ values vary from 0.09 kg/kg to 0.21 kg/kg, coherently with the range identified by wilting point (0.07 kg/kg) and field capacity (0.24 kg/kg). Conversely, the $w_{\gamma\,K}$ values vary from 0.14 kg/kg to 0.33 kg/kg and show a substantial progressive positive drift as the tomato crop matures. In the perspective of employing proximal gamma-ray spectroscopy for automatic irrigation management, the BWC correction is mandatory for assessing crop water demand and for a sustainable use of water.

3.2.3 Conclusions

The continuous tracing of soil water content provided by radiometric measurements has high potentialities for a site specific rational irrigation planning aimed at a sustainable use of water. The proposed method can be adopted both as a stand-alone approach at intermediate scale and as a benchmark for satellite and punctual based soil water content estimations.

Proximal gamma-ray spectroscopy performed with permanent stations installed at agricultural sites is an effective tool for estimating soil water content, only if provided both a reliable calibration and an adequate correction for the gamma signal reduction provoked by growing vegetation. Indeed, in order to obtain an unbiased quantitative estimate of the gravimetric water content a proper biomass water content correction is mandatory.

In this context we performed a proximal gamma-ray spectroscopy experiment by installing a permanent station in a tomato field which allowed for assessing soil water content dynamics over a 7 months period. We demonstrate that an effective way to evaluate the shielding due to stems, leaves and fruits is to model biomass as an equivalent water layer which thickness increases during the crop life-cycle. Monte Carlo simulations highlight that gamma-ray measurements are not only extremely sensitive to water in the soil but also to water concentrated in the biomass which acts as a shielding layer sitting on top of the soil gamma source. In particular, the gamma signal is affected by a sizeable reduction on the order of 10% for 10 mm equivalent water thickness, which would translate into a soil water content estimation biased by 90%.

Soil water content inferred from proximal gamma-ray spectroscopy was validated against independent gravimetric measurements. The validation set of measurements performed in bare soil condition provides an excellent result, with a 3% deviation of the gamma estimated value from the reference gravimetric one. By applying the BWC correction to gamma measurements acquired during the vegetated period, the systematic positive bias is prevented and an average discrepancy of 4% for the validation measurements is observed. The proposed method permitted to exclude systematic underestimations or overestimation of the SWC: a reliable reconstruction of soil water content temporal dynamics over the entire data taking period is obtained, coherent with the hydraulic properties of the soil at the experimental site. Otherwise, neglecting the BWC shielding effect would provide overestimated soil water content values implying that proximal gamma-ray spectroscopy would be useless as a monitoring and decision support tool for automatic irrigation scheduling with negative impacts on crop productivity.

3.3 Modelling soil water content in a tomato field: proximal gamma ray spectroscopy and soil-crop system models

In this section are exposed the investigate the potentialities of proximal gamma ray spectroscopy for a real-time and continuous monitoring of soil water content in the framework of an ad-hoc experiment. By employing a 1L sodium iodide detector placed at a height of 2.25 m, I investigated the gamma signal coming from an area having a ~25 m radius and from a depth of approximately 30 cm. Experimental values, inferred after a calibration measurement and corrected for the presence of biomass, were corroborated with gravimetric data acquired under different soil moisture conditions, giving an average absolute discrepancy of about 2%. A quantitative comparison was carried out with data simulated by AquaCrop, CRITeRIA and IRRINET soil-crop system models. The different goodness of fit obtained in bare soil condition and during the vegetated period highlighted that CRITeRIA showed the best agreement with the experimental data over the entire data-taking period while, in presence of the tomato crop, IRRINET provided the best results.

3.3.1 Materials and Methods

3.3.1.1 Experimental site

The proximal-gamma ray sensing experiment was conducted in the period 4th of April – 2nd of November 2017 in a 40 m × 108 m tomato test field of the Acqua Campus (44.57° N, 11.53° E; 16 m above sea level), a research centre close to Bologna of the CER irrigation district in Emilia-Romagna (Munaretto and Battilani, 2014) (Figure 3.20). The climate of the experimental area is classified according to the Koppen-Geiger classification as Cfa (Peel et al., 2007), i.e. a temperate climate, without dry seasons and with hot summers, with a mean temperature of 14.0 °C and mean annual precipitation of about 700 mm.

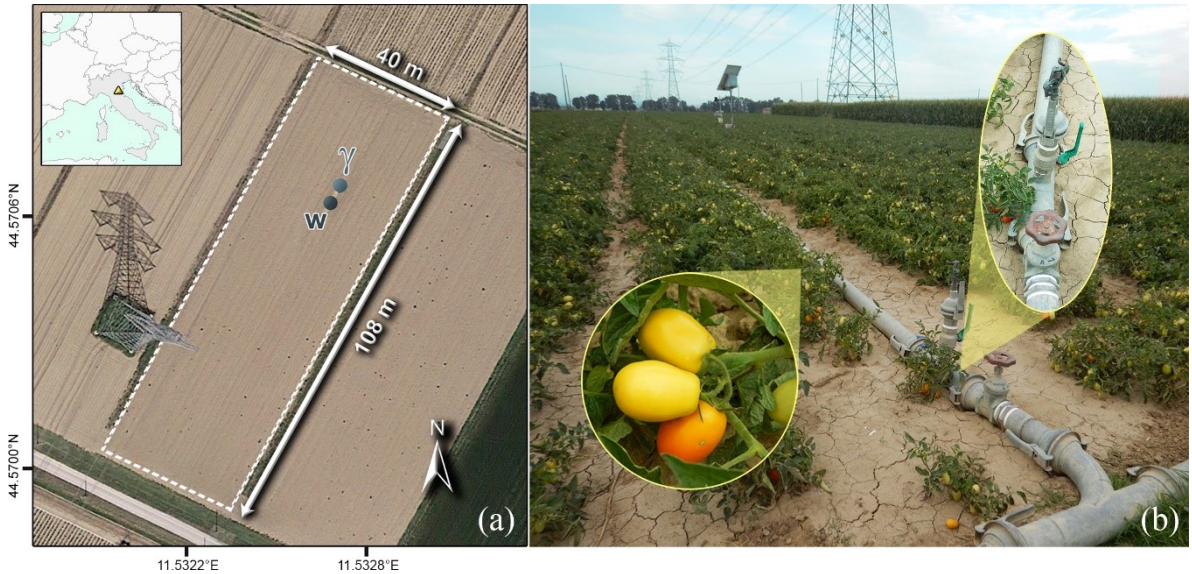

Figure 3.20. We report the geographic location of the experimental site of the Acqua Campus of CER (Emilia-Romagna, Italy), the dimensions of the tomato test field and the positions of the gamma (γ) and agro-meteorological (w) stations (panel a). The tomato crop with focuses on a tomato plant and on a sprinkler are shown in panel b.

The main physical and hydraulic parameters of the soil, characterized by a loamy texture, are reported in Table 3.8. The analysis by the sieving and the hydrometer method followed the standard procedure described in (Head and H. Epps, 1992) and was performed with the aim of measuring the Particle Size Distribution (PSD) function and, therefore, the percentage of silt, clay and sand (Table 3.8). The soil classification was based on the United States Department of Agriculture (USDA) method. The PSD was used to derive the soil water retention and hydraulic conductivity functions.

Table 3.8. Physical and hydraulic parameters of the experimental site soil for the depth horizon [0 – 30] cm. Sand, silt and clay percentage as well as bulk density were determined from direct measurements. The Wilting Point (θ_{WP}), Field Capacity (θ_{FC}), the saturation value (θ_s) and Saturated Hydraulic Conductivity (K_s) are inferred on the basis of the methods discussed in Section 3.3.1.1.

Parameter	Value
Sand [%]	45
Silt [%]	40
Clay [%]	15
Soil textural class	Loam
Soil bulk density [kg/m^3]	1345
Wilting Point (θ_{WP}) [m^3/m^3]	0.09
Field Capacity (θ_{FC}) [m^3/m^3]	0.32
Saturation (θ_s) [m^3/m^3]	0.48
K_s [cm/day]	23

After having experimentally obtained the PSD, we employed a mono-modal log-normal distribution, where the particle diameter is replaced by its natural logarithm. Details about the methodology are provided in (Bittelli et al., 2015). The μ = 22.07 μm mean and a σ = 2.81 μm standard deviation show that the distribution is within the silt range, when using the USDA textural classifications limits (Bittelli et al., 2015). The obtained PSD parameters were adopted for the retrieving the parameters of the Campbell's equation (Campbell and Shiozawa, 1992):

$$\psi_e = 0.61 ln\mu - 3.9 \tag{3.34}$$

$$b = 8.25 - 1.26 ln\mu \tag{3.35}$$

where ψ_e is the air entry potential (J/kg), b is the slope parameter in the Campbell's water retention curve equation (Campbell, 1974). The saturated water content was obtained from the relationship $\theta_s = 1 - \frac{\rho_b}{\rho_s}$, where ρ_b is the measured bulk density (Table 3.8), and ρ_s is the particle density (a value of 2600 kg/m^3 was assumed). The Campbell's water retention curve (Figure 3.21) for the soil water content ϑ as function of the ψ potential was then obtained as follows:

$$\theta(\psi) = \begin{cases} \theta_s \left(\frac{\psi_m}{\psi_e}\right)^{-\frac{1}{b}}, if\ \psi_m \geq \psi_e \\ \theta_s,\ \ if\ \psi_m < \psi_e \end{cases} \tag{3.36}$$

The soil hydraulic properties in terms of Wilting Point (θ_{WP}), Field Capacity (θ_{FC}) and saturated hydraulic conductivity (K_s) (Table 3.8) were then inferred from the retention curve of Figure 3.20.

Tomato plants were transplanted on the 23rd of May in coupled rows: the plants geometry was such that the distance between two couples was 1.5 m, the distance between two rows of the same couple 0.45 m and the distance between two tomato plants of the same row 0.38 m. On the basis of this configuration, and assuming a homogeneous plant distribution on the experimental site area, a 3.5 plants/m^2 planting density was estimated. The anthesis of the plants took place approximately on the 9th of June, the berries maximum maturity occurred on the 30th of August and the harvesting on the 14th of September (Figure 3.22a). The irrigation was performed via sprinklers (Figure 3.19) and the crop was irrigated according to IRRINET's water balance.

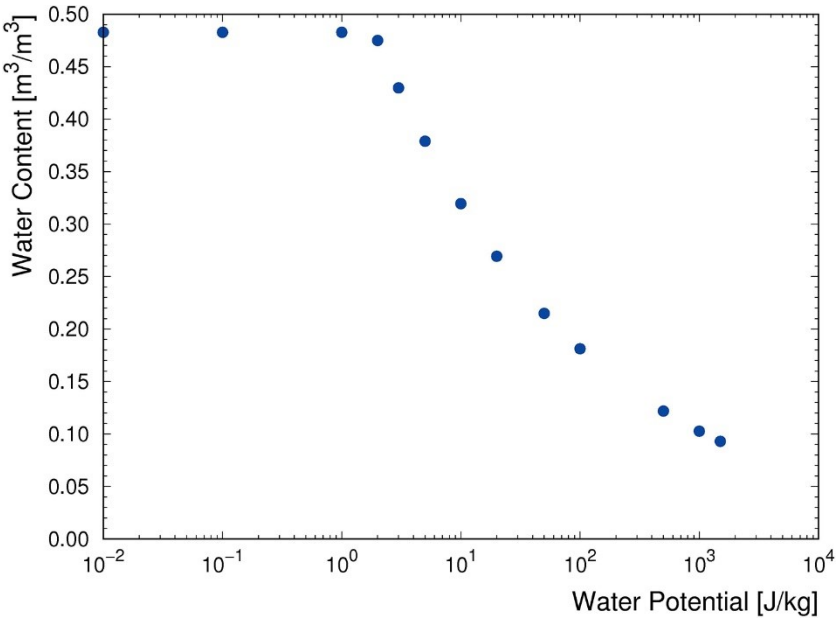

Figure 3.21. Campbell's water retention curve obtained on the basis of the mean particle size determined after the parameterization of the PSD.

3.3.1.2 Experimental setup

The experimental setup comprised a commercial agro-meteorological station (MeteoSense 2.0, Netsens) and a gamma ray spectroscopy station specifically designed and built for the experiment (Figure 3.23).

Measured weather data included air temperature, Relative air Humidity (RH), wind direction and speed, precipitation and Short Wave Incoming Radiation (SWIR), the latter measured with a silicon-photodiode pyranometer. We report for the entire data-taking period the temporal profiles of daily values recorded for the Minimum (T_{min}) and Maximum Temperatures (T_{max}) (respectively ranging in the T_{min} = [1.3 - 22.7] °C and T_{max} = [13.5 - 39.3] °C intervals) (Figure 3.22a), the SWIR (ranging from 34.7 to 257.3 W/m^2) (Figure 3.22b), the RH (ranging from 44.3% to 95.2%), the rainfall amount (which reached a maximum of 56.2 mm), the irrigation water (which reached a maximum of 35 mm) (Figure 3.22c). The reference Evapotranspiration (ET0) (Figure 3.22b) was calculated through the Hargreaves equation (Hargreaves and Samani, 1985) by adopting the weather parameters recorded during the data-taking by the agro-meteorological station.

A 1L sodium iodide (NaI) crystal was placed inside a steel box mounted on top of a 2.25 m high steel pole. The gamma spectrometer was coupled to a photomultiplier tube base which output is processed by a

digital multi-channel analyser (MCA, CAEN γstream); the whole system was powered by a solar panel (Figure 3.23). The detector measured the photon radiation produced in the decays of natural occurring radionuclides (^{40}K, ^{238}U and ^{232}Th) and recorded a gamma spectrum, i.e. a histogram representing the energy distribution of photons emitted by the source. Since each gamma decay has a specific emission energy, a gamma spectrum is characterized by the presence of distinctive structures (photopeaks) which allow for the identification and quantification of ^{40}K, ^{238}U and ^{232}Th abundances in the soil. The integrated number of events inside the energy ranges associated to the main photopeaks (IAEA, 2003) were used to determine the counts per second (cps), associated to ^{40}K, ^{238}U and ^{232}Th activities in the soil. The statistical uncertainty on the measured cps for a gamma spectrum with a temporal length of one hour is typically lower than 1%. As photon propagation is ruled by the density of traversed materials, a gamma spectrometer is sensitive to about 25 m far in the horizontal direction (Figure 3.23) and approximately 30 cm deep in the soil (Figure 3.24).

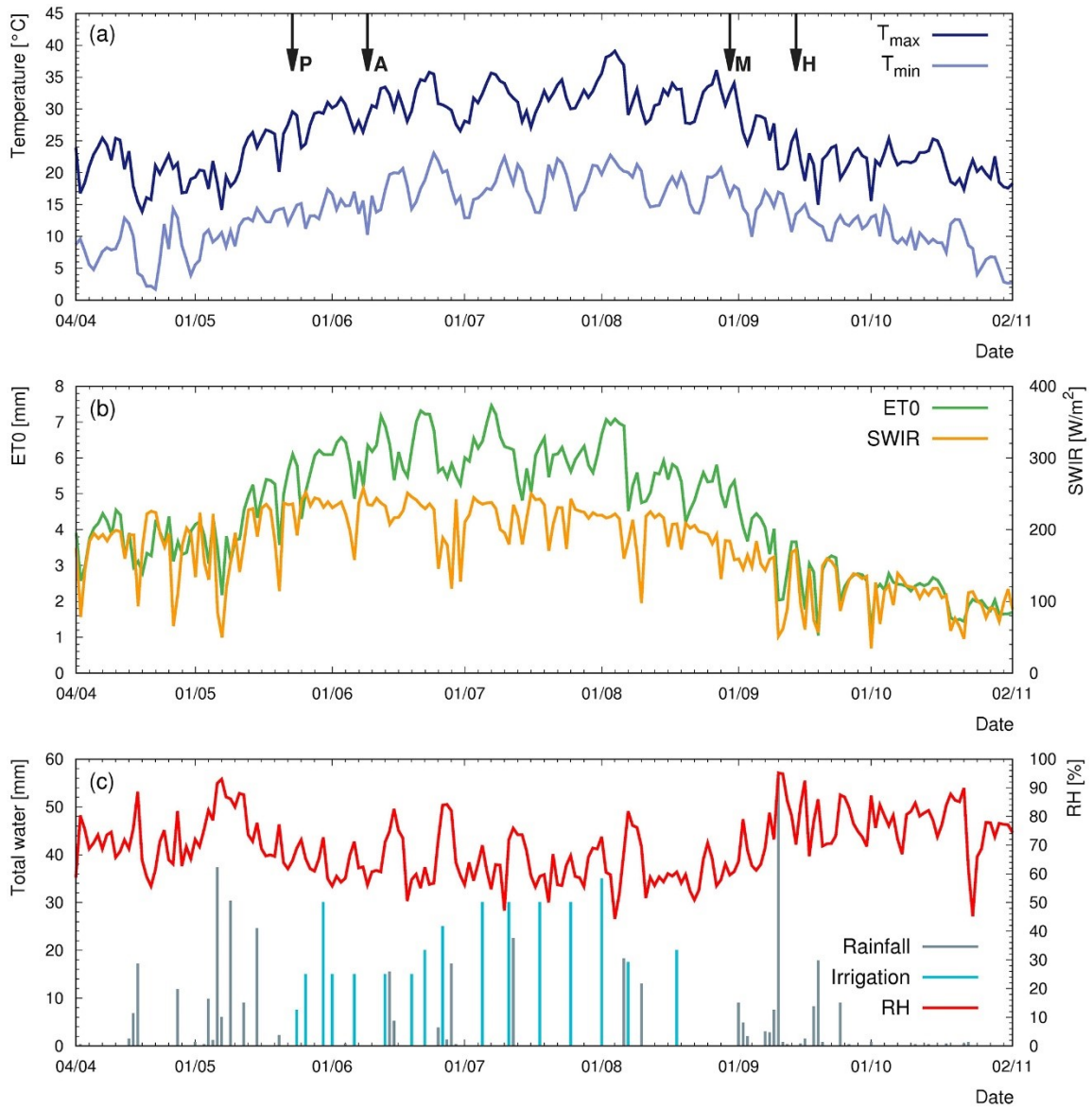

Figure 3.22. Weather parameters recorded in the 4th of April – 2nd of November 2017 data-taking period by the agro-meteorological station installed at the experimental site: Maximum (T_{max}) and Minimum (T_{min}) Temperature (panel a), Short Wave Incoming Radiation (SWIR) (panel b) and Relative air Humidity (RH), rainfall and irrigation water amount (panel c). The reference Evapotranspiration (ET0) (panel b) is calculated on the basis of Hargreaves equation (Hargreaves and Samani, 1985). The arrows in panel a) indicate the four major crop maturity phases, i.e. Planting (P, 23th of May), Anthesis (A, 9th of June), Maturity (M, 30th of August) and Harvesting (H, 14th of September).

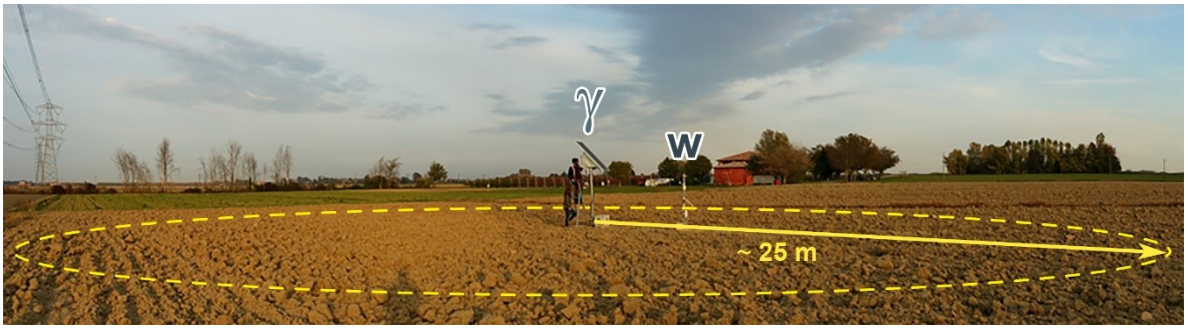

Figure 3.23. Gamma (γ) and agro-meteorological (w) stations installed at the experimental site. About 95% of the signal received by the gamma spectrometer located at 2.25 m above the ground is produced within a ~25 m radial distance.

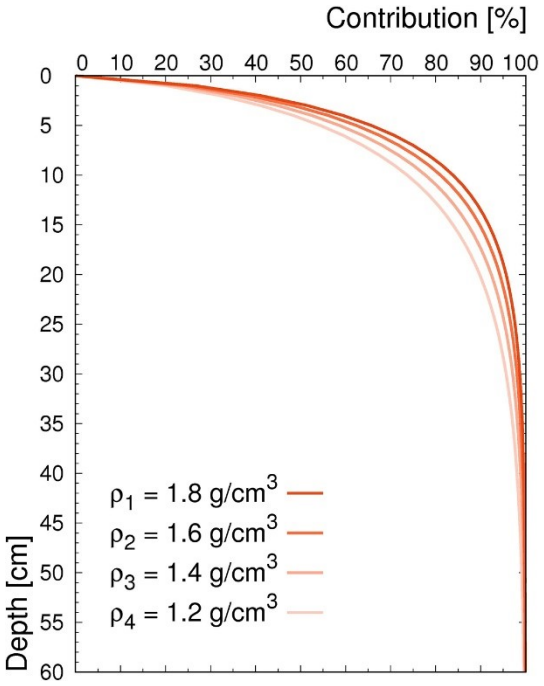

Figure 3.24. Percentage contribution to the ^{40}K ground level unscattered photon flux as function of soil depth. The contribution is computed for four soil density values: as the density increases from 1.2 g/cm^3 to 1.8 g/cm^3, the depth corresponding to 95% of the signal decreases from 28 cm to 19 cm.

Weather data were recorded by the agro-meteorological station with an average frequency of about 5 minutes, while the gamma station provided a list mode output, i.e. a continuous logging of individual photons arrival time and energy. Therefore, a dedicated software was developed to group and synchronize all the acquired data in a single time-referenced dataset. As both stations were equipped with a GPRS connection, it was possible to remotely preprocess the data in real time. The resulting dataset had a temporal resolution of 15 minutes and merged 10 data fields from the agro-meteorological station temporally aligned with 34 data fields from the processed energy spectra. Both stations were operative during the entire data taking period, for a 94.8% overlapping duty cycle and a 260 GB global amount of uncompressed data, the major part being raw gamma spectra.

3.3.2 Results

3.3.2.1 Soil water content with proximal gamma-ray spectroscopy

The basic principle for the determination of soil water content using natural terrestrial gamma radiation recorded by a permanent measurement station consists in the quantification of relative differences between gamma signals measured under different moisture level conditions. While ^{208}Tl (^{232}Th decay chain) and ^{40}K are distributed solely in the soil, gamma radiation originated by the decay of ^{214}Bi (^{238}U decay chain) comes both from ^{214}Bi in the soil and from ^{214}Bi in the atmosphere produced by the decay of ^{222}Rn gas exhaled from rocks and soils. For this reason, we chose ^{40}K as natural gamma emitter for soil water content assessment purposes, given also the highest net counting statistics in its photopeak.

Since the water mass attenuation coefficient is significantly higher than those of typical minerals commonly present in the soil, a gamma spectroscopy measurement is extremely sensitive to different soil moisture levels. The gamma photon flux at the soil-air interface and, consequently, the measured gamma signal are inversely proportional to soil water content: by simultaneously performing an independent gravimetric calibration measurement and a radiometric acquisition, it is possible to evaluate the gravimetric soil water content $w_{\gamma\,K}$[kg/kg] at a specific time *t* as follows (Baldoncini et al., 2018a; Baldoncini et al., 2019):

$$w_{\gamma\,K}(t) = \frac{S_K^{Cal}}{S_k(t)} \cdot \left(\Omega + w^{Cal}\right) - \Omega \tag{3.37}$$

where w^{Cal} is the gravimetric water content at calibration time, S_K^{Cal} and $S_K(t)$ are the gamma signals in cps recorded in the ^{40}K energy window respectively at calibration time and at time *t*.

The calibration measurement w^{Cal} = (0.163 ± 0.008) kg/kg is the mean gravimetric water content estimated after a gravimetric campaign performed in bare soil condition in the [0-30] cm depth range at 16 planar sampling points homogeneously distributed within 15 m from the gamma station (Baldoncini et al., 2019). The gamma calibration measurement S_K^{Cal} refers to a 2 hour late morning data acquisition (10.00 a.m. – 12.00 a.m.) concomitant with the gravimetric sampling, distant from rainfall and irrigation events and with stable atmospheric conditions, avoiding potential interferences due to early morning fluctuations in atmospheric ^{222}Rn.

The adimensional coefficient Ω is a constant corresponding to the ratio between the mass attenuation coefficient in solids and water. In this study we adopted a value of Ω = 0.899, estimated on the basis of the specific composition of the soil of the experimental site (Baldoncini et al., 2018a). If a soil mineralogical analysis lacks, a mean value together with its standard deviation Ω = (0.907 ± 0.011) estimated in (Baldoncini et al., 2018a) can be adopted. The Ω variability is expected to have second order effects on the estimation of gravimetric water content as the variation introduced by different Ω values would be undistinguishable within the ~0.017 kg/kg absolute uncertainty on the estimated w values, which is essentially dominated by the systematic component associated to the S^{cal} and w^{Cal} calibration reference values (Baldoncini et al., 2019).

While in bare soil condition gamma rays propagate only through air after having reached the soil surface, the presence of growing vegetation introduces a sizable extra attenuation that can be modelled in terms of Biomass Water Content (BWC), i.e. an equivalent water layer which thickness varies in time as the crop evolves during its life-cycle. In order to avoid a systematic overestimation of the gravimetric water content, a correction for the BWC presence needs to be applied as follows:

$$w_{\gamma K}^{\Lambda} = \frac{S_K^{Cal} \cdot \Lambda_K\left(BWC(t)\right)}{S_k(t)} \cdot \left(\Omega + w_G^{Cal}\right) - \Omega \tag{3.38}$$

The BWC correction factor Λ_K [cps/cps] changes in time and it is given by the ratio between the S_K recorded at the time *t* when there was a given BWC at the experimental site and the signal recorded for BWC = 0. In this study we adopted the Λ_K curve determined in (Baldoncini et al., 2019) by adopting the Monte Carlo simulation method described in (Baldoncini et al., 2018a). Λ_K is identically equal to 1 for null vegetation cover, as expected, and is equal to 0.88 for the 9.7 mm maximum BWC estimated during the field experiment. If neglected, this missing correction would have biased the gravimetric water content by approximately a factor of 2.

The hourly average results in terms of ^{40}K gamma count rates (in cps) and of volumetric water content θ_γ (in m^3/m^3) are reported in Figure 3.25. The latter was obtained by multiplying the gravimetric water content $w_{\gamma K}$ for the experimental site soil bulk density (Table 3.8). As expected, the gamma signal and the volumetric water content are respectively negatively and positively correlated with the amount of precipitations that include both rainfall and irrigation water.

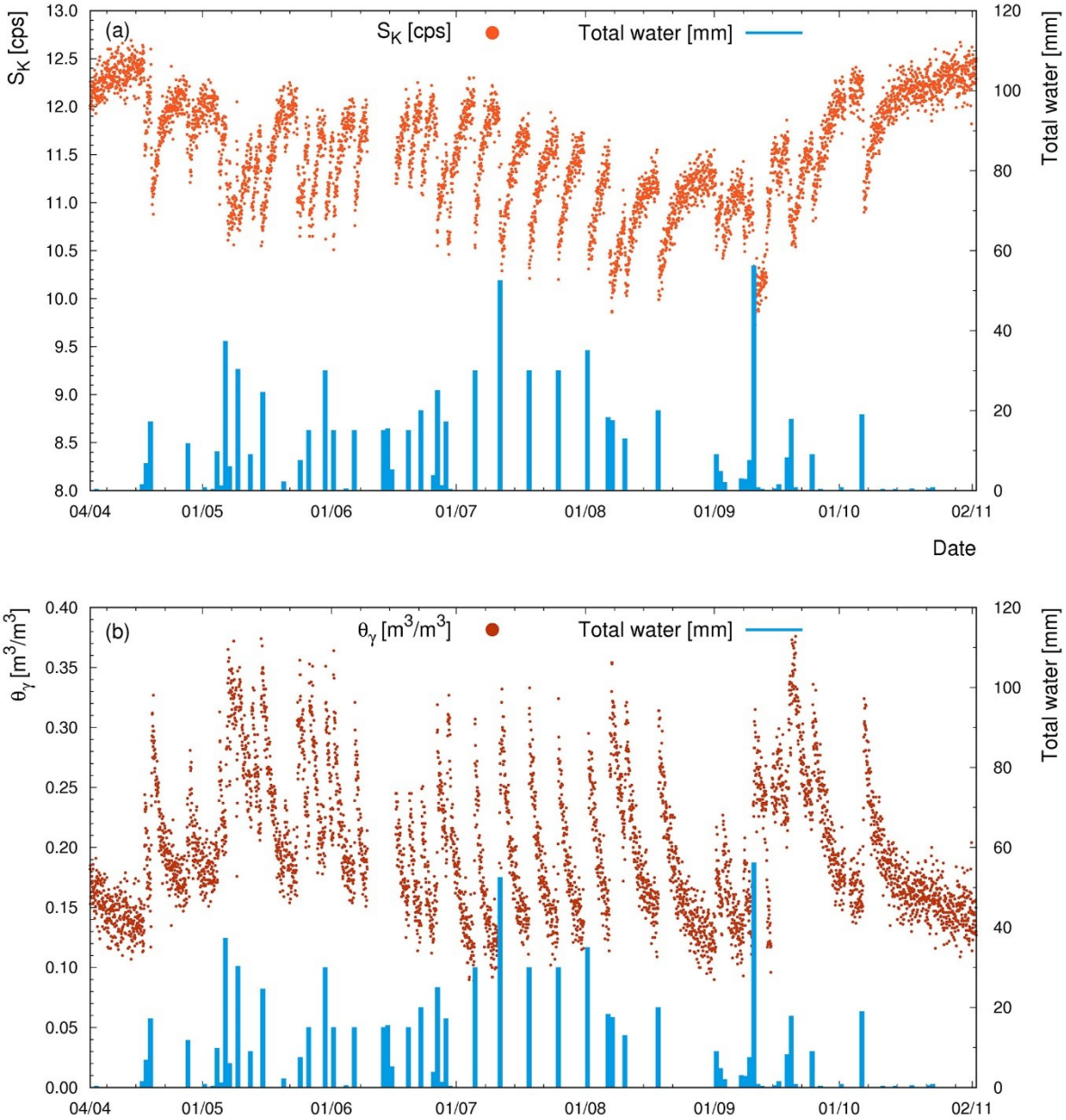

Figure 3.25. In panel (a) is reported the ^{40}K gamma signal in cps (S_K). In panel (b) the volumetric water content (θ_γ) estimated on the basis of gamma spectroscopy measurements and corrected for the attenuation due to the biomass water content. The data are hourly averaged. In both panels the daily amount of rainfall and irrigation water are reported in mm.

The correction for the BWC and the overall reliability of the method were tested with an ad-hoc sampling campaign performed in presence of biomass and in 3 different soil moisture conditions (Table 3.9), i.e. one day before an irrigation event (24th of July), one (26th of July) and three days (28th of July) after the same event. One set of additional validation measurements was carried out also in bare soil condition two days after a rainfall event (21st of September) (Baldoncini et al., 2019). The gamma water contents θ_γ, inferred from gamma signals measured in the same time interval of samples collection, were compared with the weighted average volumetric water contents θ_G inferred from the sampling campaign. The [0 – 10] cm, [10 – 20] cm and [20 – 30] cm θ_G values were combined with weights respectively equal to 0.79, 0.16 and 0.05, determined on the basis of the gamma signal depth profile.

An average discrepancy between the experimental measurements (θ_G) and estimated values (θ_γ) of -2.1% is observed. By taking into account the statistical dispersions of the sets of gravimetric measurements, the θ_γ values are compatible with θ_G values at 1σ level for all the validation days. Systematic errors leading

to underestimations or overestimation of the gravimetric water content are to be excluded also in presence of the tomato crop at the experimental site.

Table 3.9. Results of the four corroboration measurements of volumetric water content. Measurements in presence of biomass were performed one day before an irrigation event (24th of July), one (26th of July) and three days (28th of July) after the same event. The fourth measurement (21st of September) was performed in bare soil condition two days after a rainfall event. For each measurement we report the volumetric water content inferred from proximal gamma ray spectroscopy measurements (θ_γ) together with its 1σ uncertainty, the weighted average volumetric content determined from the gravimetric campaign (θ_G) and from daily values simulated with the CRITeRIA (θ_C) and AquaCrop (θ_A) models; for IRRINET the mean daily volumetric water content (θ_I) is reported only during the tomato crop season (see Section 3.3.2.2).

Day	θ_G [m^3/m^3]	θ_γ [m^3/m^3]	θ_C [m^3/m^3]	θ_A [m^3/m^3]	θ_I [m^3/m^3]
24/07	0.167 ± 0.028	0.170 ± 0.023	0.134	0.107	0.154
26/07	0.265 ± 0.028	0.243 ± 0.023	0.224	0.247	0.189
28/07	0.189 ± 0.029	0.179 ± 0.023	0.168	0.152	0.168
21/09	0.237 ± 0.015	0.245 ± 0.023	0.255	0.310	/

3.3.2.2 Soil water content with soil-crop system models

The daily values of soil water content simulated with CRITeRIA, AquaCrop and IRRINET soil-crop system models were compared to the experimental daily values inferred from proximal gamma ray spectroscopy. For the simulation we used the soil properties reported in Table 3.8, daily temperatures and precipitation amounts measured by the agro-meteorological station, scheduled irrigations, growth stages of the tomato crop and reference evapotranspiration (ET0) calculated on the basis of the Hargreaves method (Hargreaves and Samani, 1985) (Figure 3.22). The CRITeRIA and AquaCrop values, referred to the entire data-taking period (4th April – 2nd November 2017), were obtained by running the models with a 6 months spin-up which was performed by adopting meteorological data published at (Freni and Mannina, 2012) in order to adjust for initial conditions (Bittelli et al., 2015). As the IRRINET simulation is strictly bounded to the crop development, soil water content data are referred to the sole tomato crop season (23th May – 14th September 2017).

- **CRITeRIA**

CRITeRIA is a suite of soil water balance and crop modelling systems developed by the Regional Environmental Protection Agency (ARPA) of the Emilia-Romagna region (Italy). Here we used CRITeRIA-1D, which is a one-dimensional model simulating the soil water balance, the nitrogen balance and crop development. The CRITeRIA-1D model simulates soil water movement by using a numerical solution of Richards' equation as described in (Bittelli et al., 2010). The model implements many herbaceous crops and fruit trees and requires as input daily weather data (temperature and precipitation), soil texture and hydraulic properties, bulk density and crop management information. For this study water retention and hydraulic conductivity curve were determined on the basis of PSD experimental data (see Section 3.3.1).

CRITeRIA implements a crop growth model based on the day degree sum. The relevant variables are the development of the leaf system (expressed by the leaf area index parameter) for the epigeal part and a root growth model for increase and spatial distribution of the root system. As the tomato season was characterized by anomalously high temperatures, parameters regulating the leaf area index increase and decrease were properly calibrated to follow the effective tomato plants growth at the experimental site.

- **AquaCrop**

AquaCrop is a crop water productivity model implemented by the Land and Water Division of FAO (Steduto et al., 2009). In the perspective of being applied to diverse worldwide agricultural systems characterized by large crop and soil variability and by the unavailability of extended number of site specific input variables, AquaCrop is structured as an almost ready to use simulation model, requiring a low number of explicit parameters.

The model simulates the water balance and yield response to water of herbaceous crops and it is typically used in situations where water is a key limiting factor in crop production (Steduto et al., 2009). AquaCrop develops a structure (sub-model components) that includes: (i) the soil, with its water balance; (ii) the crop, with its development, growth, yield and management; (iii) the atmosphere, with its thermal regime, rainfall, evaporative demand and carbon dioxide concentration. The calculation procedure is grounded on basic and complex biophysical processes to guarantee an accurate simulation of the response of the crop in the plant-soil system. The computation of the soil water transport is based on a tipping-bucket conceptual model employing soil hydraulic properties in terms of θ_{FC} and θ_{WP}.

- **IRRINET**

IRRINET is one of the tools provided to farmers in the framework of the Emilia-Romagna Action Plan for Rural Development 2007 – 2013. It is a model for irrigation management backed by the results of more than 50 years of research on plant/water relation and sustainable irrigation management (Mannini et al., 2013). IRRINET was developed with the aim of progressively reducing water use for irrigation without harming farmers' income, therefore saving water and optimizing water productivity. The freely available service is web and GIS based and provides decisional criteria for irrigations for a large number of water demanding crops. The model can be employed by using several data sources as meteorological and soil data from local services and crop parameters as defined by CER, including application of the most effective crop tailored irrigation strategy.

Since 2009 IRRINET implements economic calculation of the irrigation profitability assessing the economic benefit related to the next irrigation. Users are provided with optimal irrigation volume and interval, via web or mobile phone text message.

The crop water balance is calculated at field scale with a daily frequency and referred to the crop characteristics, simulated or inputted by the farmer. The model structure deals with the soil-plant-atmosphere continuum and includes (i) the soil water balance with capillary rise (Battilani and Mannini, 1994), infiltration rate and run off (Driessen, 1986), (ii) the development of plant with crop coefficients (Doorenbos, 1977), (iii) the atmosphere (thermal regime, rainfall and evaporative demand) and (iv) the irrigation system adopted. For sprinkler systems, IRRINET guides the irrigation in order to maintain soil moisture between 30% and 70% of the available water (θ_{FC}-θ_{WP}). Mean soil water content is estimated in a progressively deeper soil range which linearly follows the growth of the root system from an initial depth of 15 cm (at the time of transplanting) up to 65 cm.

3.3.3 Discussions

As soil water content values provided by CRITeRIA (θ_C), AquaCrop (θ_A) and IRRINET (θ_I) are referred to a daily frequency, we averaged the 24 hourly experimental volumetric water contents (θ_V) in order to obtain soil moisture dynamics curves with the same temporal resolution (Figure 3.26). θ_C and θ_A were determined by combining the [0 – 10] cm, [10 – 20] cm and [20 – 30] cm values according to the 0.79, 0.16 and 0.05 weights described in Section 3.3.2.1. θ_I refers to the mean value in the variable depth horizon

modelled by IRRINET (see Section 3.3.2.2). The four datasets show consistent temporal trends, positively correlated with the amount of precipitated water (Figure 3.22c).

Although the three simulated datasets never reach the saturation value θ_s (Table 3.8), we observed different variability ranges that reflect the different computational methods of water depth redistribution. The widest dynamic observed for the θ_A values is attributable to the tipping-bucket conceptual model implemented in AquaCrop, making the water content of the most superficial layer exceed field capacity θ_{FC} (Table 3.8) and reach a maximum value (0.44 m^3/m^3) close to θ_s before draining water to the deeper layers. In the summer period, when the depletion of water content due to plant water uptake becomes relevant, AquaCrop provides the lowest values (0.07 m^3/m^3), which are below the wilting point θ_{WP} (Table 3.8). Conversely, CRITeRIA exhibits a more homogenous depth water distribution as physically based models usually provide a more accurate computation of water fluxes across soil strata. As in CRITeRIA each soil layer is characterized by a limited water content variability (~25%), the excursion of θ_C values is confined in the (0.11 - 0.31) m^3/m^3 interval, almost corresponding to the (θ_{WP} - θ_{FC}) range. A narrower variability (0.14 - 0.23 m^3/m^3) is observed in the temporal trend of IRRINET values (θ_I), which are intrinsically averaged over a variable maximum depth defined as the tomato root system vertical horizon. The θ_γ experimental values lie in the (0.12 - 0.33) m^3/m^3 range, compatible with soil hydraulic properties in terms of θ_{WP} and θ_{FC} (Table 3.8), and are consistent with models variability almost over the entire data taking. Limited temporal misalignments between experimental and simulated daily values can be due to the averaging of gamma inferred volumetric water contents, which are sensitive to the occurring of impulsive rainfall and irrigation events (Figure 3.25). On the opposite, simulation models cluster the output water contents with a daily resolution, making unresolvable the variations due to distinct precipitation events within a day.

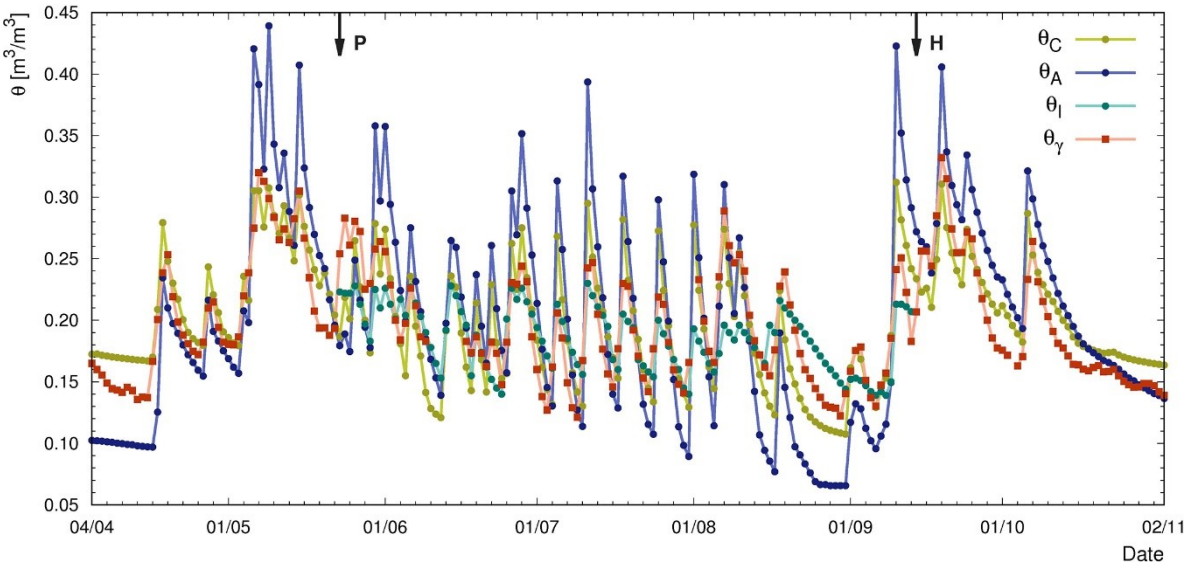

Figure 3.26. Daily volumetric water content as function of time over the entire data-taking period inferred from gamma ray spectroscopy measurements (θ_γ), CRITeRIA (θ_C) and AquaCrop (θ_A), and over the tomato crop season for IRRINET (θ_I). The arrows indicate the tomato crop Planting (P) and Harvesting (H).

The general agreement between experimental and simulated values was assessed in terms of linear regression between the datasets over the entire data-taking period and separately over the bare soil and vegetated periods (Figure 3.27). Together with the slope (m ± δm), intercept (q ± δq) and coefficient of determination (r^2), we estimated the Nash-Sutcliffe coefficient (NS) (Nash and Sutcliffe, 1970) (Table 3.10). The NS quantifies the relative magnitude of the residual variance between experimental (θ_γ) and simulated values (θ_A, θ_C and θ_I) compared to the measured data variance. A good model performance is indicated by a

NS value close to 1. When NS = 0 the model predictions are as accurate as the mean of the observed data, whereas for NS < 0 the observed mean is a better predictor than the model, since the residual variance is greater than the data variance. It is a useful indicator for time series as it also captures the model performance over time.

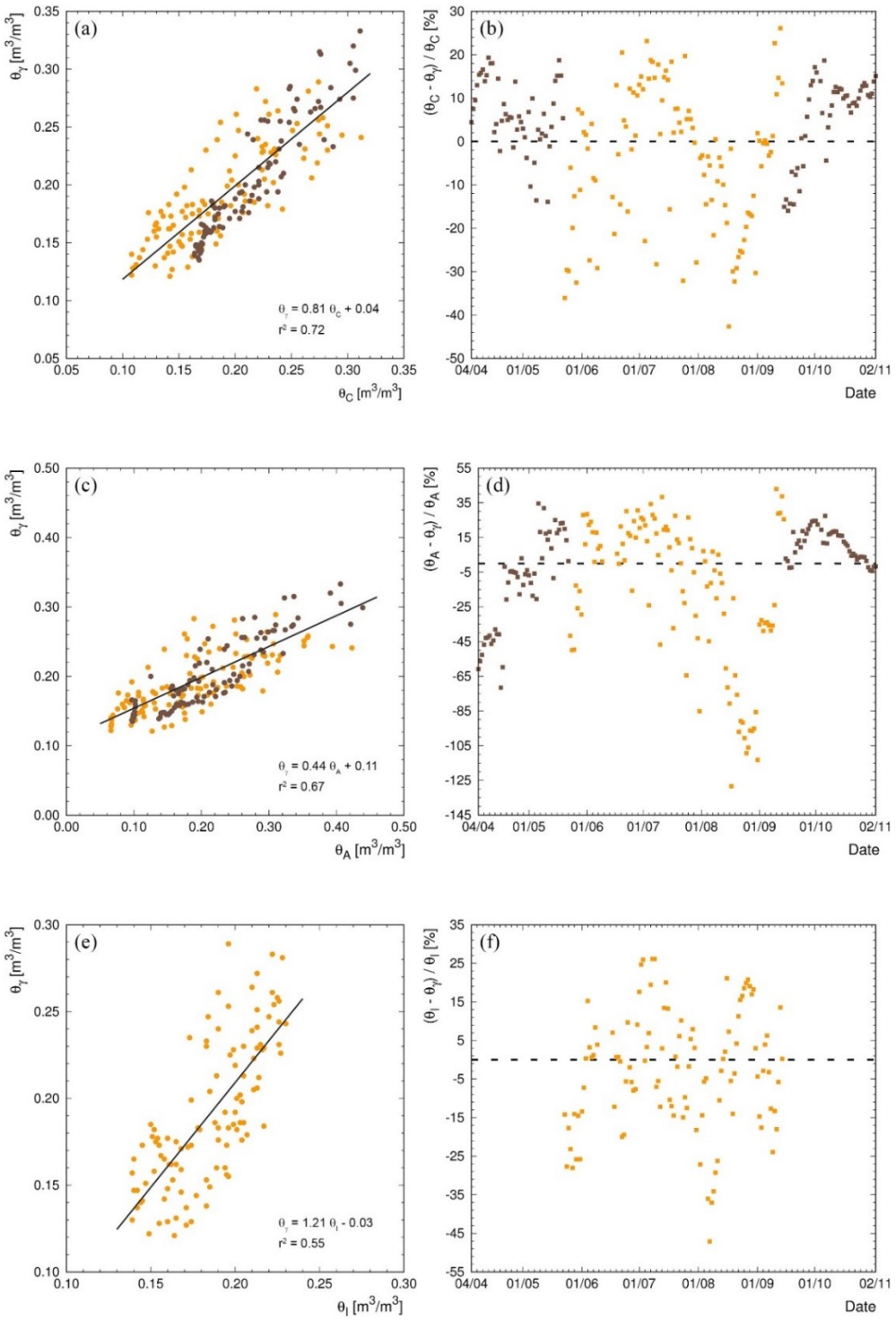

Figure 3.27. Scatter plot of the daily volumetric water contents inferred from gamma ray spectroscopy (θ_γ) versus the daily volumetric water content estimated with CRITeRIA (θ_C) (panel a), AquaCrop (θ_A) (panel c) and IRRINET (θ_I) (panel e). For each scatter plot the regression line is superimposed and its corresponding equation is reported. The percentage differences with respect to θ_γ values are shown for θ_C (panel b), θ_A (panel d) and θ_I (panel f). Different colours are assigned to data points in bare soil condition (brown) and in presence of the tomato crop (orange).

Considering the m, r^2, q and NF values over the entire data taking period, CRITeRIA shows a better agreement with experimental measurements with respect to AquaCrop (Table 3.10). Indeed AquaCrop performed poorly, especially in presence of tomato crop when a negative NS value (-1.04) is observed and θ_A values increase on average by a factor of 2 with respect to θ_γ values. During the vegetated period, when also IRRINET simulated data are available, the best agreement is observed between θ_γ and θ_I. Indeed, the goodness of fit between experimental and IRRINET simulated data is proved by a q value compatible with 0 at a 1.5σ level and an average 20% increase of soil water content with respect to experimental values. For CRITeRIA, AquaCrop and IRRINET we obtain r^2 values moderately different from 1 (Table 3.10) which, however, do not indicate fitting models different from linear trends but highlight a relatively high dispersion of the data around the regression line (Figure 3.27 a, c, e). The mean and standard deviation of percentage differences between modelled and experimental values are (1 ± 14)% for CRITeRIA, (-9 ± 35)% for AquaCrop and (-3 ± 16)% for IRRINET. Although for all the models relatively high normalized differences respect to θ_γ are observed in the vegetated period (Figure 3.27 b, d, f), the time series of percentage discrepancies show a scattered behaviour which leads to exclude evident biases, e.g. due to the correction for BWC attenuation applied to experimental signals.

Table 3.10. Parameters of the linear regressions between the daily volumetric water content inferred from gamma ray spectroscopy measurements and from simulation models. Together with the slope (m ± δm), intercept (q ± δq) and coefficient of determination (r^2), the Nash-Sutcliffe efficiency (NS) is reported for three different datasets: in presence of the tomato crop, in bare soil condition and for the whole data-taking period.

		CRITeRIA	**AquaCrop**	**IRRINET**
In presence of the tomato crop	m ± δm	0.68 ± 0.05	0.37 ± 0.03	1.21 ± 0.11
	q ± δq [m^3/m^3]	0.06 ± 0.01	0.12 ± 0.01	-0.03 ± 0.02
	r^2	0.65	0.53	0.55
	NS	0.51	-1.04	0.51
Bare soil condition	m ± δm	1.15 ± 0.04	0.57 ± 0.03	/
	q ± δq [m^3/m^3]	-0.04 ± 0.01	0.08 ± 0.01	/
	r^2	0.87	0.80	/
	NS	0.81	0.27	/
Whole period	m ± δm	0.81 ± 0.04	0.44 ± 0.02	/
	q ± δq [m^3/m^3]	0.04 ± 0.01	0.11 ± 0.01	/
	r^2	0.72	0.67	/
	NS	0.69	-0.27	/

The volumetric water content values θ_G determined on the basis of gravimetric campaigns carried out in July and in September (Section 3.3.2.1) represent a corroboration reference for evaluating the performances of simulation models and of the gamma ray spectroscopy method. It is worth to underline that Figure 3.28 reports θ_G values representative of the water content of the soil at the time of the gravimetric campaign (~2h) while θ_γ, θ_A, θ_C and θ_I are referred to daily moisture levels. In presence of tomato crop (Figure 3.28 a) the gamma ray spectroscopy method provides the best agreement with gravimetric measurements, characterized by a 9.8% absolute mean relative discrepancy, while all the simulation models show a deviation larger than 15%. Although in bare soil condition (Figure 3.28 b) gravimetric measurements are lower than simulated and experimental values, CRITeRIA and AquaCrop show coherent temporal trends, enclosing the time series inferred from gamma ray measurements.

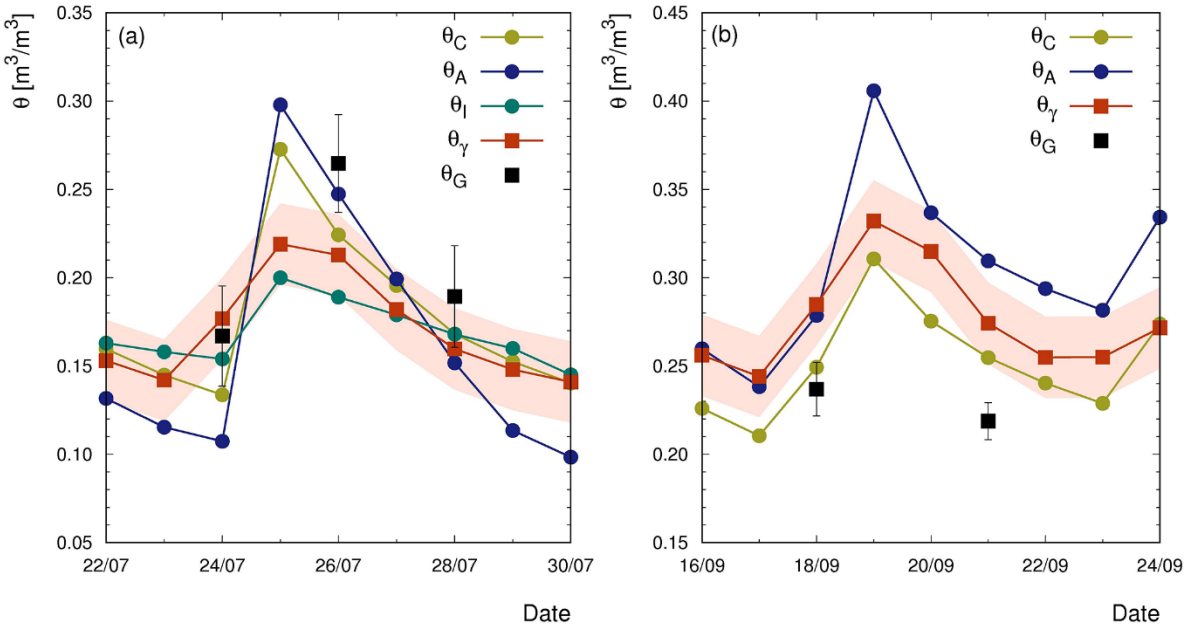

Figure 3.28. Weighted average volumetric water contents derived from the gravimetric campaigns (θ_G) carried out in the late morning (10 a.m. – 12 a.m.) during the vegetated period (panel a) and in bare soil condition (panel b). The θ_G error bars correspond to the weighted average standard deviation. Daily volumetric water contents (θ_γ) are reported together with their 1σ uncertainty. Daily simulated values with the CRITeRIA (θ_C), AquaCrop (θ_A) and IRRINET (θ_I) models are also plotted.

3.3.4 Conclusions

In the perspective of optimizing agricultural management with a sustainable use of water, one of the current challenges is performing continuous and reliable soil moisture monitoring at field scale with non-destructive and real time techniques. In this context we performed a proximal gamma ray spectroscopy experiment by installing a permanent station in a tomato field which allowed for assessing soil water content dynamics over a 7 months period. The main results of this work are as follows:

- proximal gamma ray spectroscopy is an excellent method for a non-stop tracing of soil water content at an intermediate spatial scale between punctual and satellite fields of view;
- once provided a reliable calibration through direct measurements, soil water contents inferred from gamma ray spectroscopy do not require detailed soil and crop parameterization and are characterized by relatively low uncertainties;
- while soil-crop system models simulate soil dynamics with a daily resolution, the proposed method is able to provide reliable higher frequency estimations sensitive to transient soil moisture levels, as proved by the excellent agreement with direct gravimetric measurements;
- proximal gamma ray spectroscopy gives a satisfactory description of soil water content over time also when compared to simulation data, showing that the combination of accurate soil water content measurements and water budget computation with crop models can be effective tools for water resources and irrigation planning.

Conclusions and future perspectives

After the master degree in Physics, obtained at the completion of the double degree program between the Universities of Ferrara and Paris-Sud, I started my PhD in Physics at the University of Ferrara. In these years I discovered the field of gamma-ray spectroscopy, a discipline connected not only to Physics, but also to Engineering, Earth Science, Computer Science and Statistics. During these three years I grew up by improving both technical and communication skills. The studies I performed allowed me to be part of a community of scientists that helped me with my researches and with the writing of the papers that inspired this thesis.

The sky is enlightened by cosmic rays that produce particle showers interacting with the atoms present in the atmosphere and generating many types of particle, among which gamma rays. The Earth's lower atmosphere and rain water shine in gamma rays due to ^{222}Rn daughters, ^{214}Pb and ^{214}Bi, and the topsoil is brightened by ^{40}K and the decay chains of ^{238}U and ^{232}Th. My studies led me to a journey that began literally by flying in the atmosphere, then attaching to rain droplets, to finally end at the top-soil level of an agricultural field.

Airborne Gamma-Ray Spectroscopy (AGRS) surveys are particularly suitable for monitoring radioactivity of a large territory and are affected by severe backgrounds constituted by the gamma activity of the aircraft materials, cosmic rays and atmospheric ^{222}Rn daughters. In order to study these background radiation components offshore AGRS measurements were performed for about 5 hours in the (77 – 3066) m altitude range with a 16L NaI(Tl) detector installed on the Radgyro, a ultralight aircraft designed for multiparametric surveys. The acquisition of 17.612 1s spectra over the sea at different altitudes allowed to separate the background count rate into a constant aircraft component and a cosmic component exponentially increasing with increasing height. It is possible to assess that the minimum K, U and Th concentrations the AGRS_16L detector can measure are $0.05 \cdot 10^{-2}$ g/g, 0.4 μg/g, 0.8 μg/g, respectively.

The AGRS_16L has also been calibrated for assessing the annual cosmic effective dose to human population by using as calibrating reference the dose rate values obtained with the program CARI-6. A linear correlation between the count rate in the energy window [3-7] MeV and the annual cosmic effective dose has been obtained with a slope of (20.6 ± 0.1) μSv/(y·cps) and an intercept of (58.5 ± 3.2) μSv/y. A model reproducing the altitude dependence of the count rate in the ^{214}Bi photopeak energy window was developed on the basis of a two-layers atmospheric ^{222}Rn vertical distribution, according to which radon concentration is uniform up to the mixed layer height and vanishes above. By applying this model to the AGRS offshore experimental data the ^{222}Rn concentration was estimated to be (0.96 ± 0.07) Bq/m^3 up to (1318 ± 22) m, in agreement with values reported in scientific literature.

Atmospheric ^{222}Rn daughters can attach to aerosol particles, which are collected by rain droplets in the clouds by the rain-out mechanism and fall to the ground enhancing the ^{214}Pb and ^{214}Bi activity above the background value in correspondence of a rainfall event. In this work I successfully tested a model describing the temporal evolution of the ^{214}Pb gamma activity during rain events against radiometric data acquired in a 7-months proximal gamma-ray spectroscopy experiment. The experiment was carried out by installing in an agricultural test field a 1L NaI(Tl) detector at a height of 2.25 m. The model considers a rain-induced source term, parametrized in terms of an impulsive count rate increase ΔC, and a radioactive decay exponential term, superimposed on a natural background coming from the soil source. It's demonstrated that ΔC is proportional to the square root of the rainfall rate. In perspective, this work can be further developed in order to study the mechanisms of formation of the droplets in the clouds and the radioactivity collecting

processes. Since irrigation water does not produce an enhancement in the ^{214}Pb gamma activity above the background level gamma-ray spectroscopy can easily discriminate irrigations from rainfalls.

With the same equipment in the same test field the potentialities of in-situ gamma ray spectroscopy in the field of precision agriculture were explored. Since water has a mass attenuation coefficient ~11% higher compared with the minerals composing the soil, increasing the amount of water in the pores the gamma flux reaching the detector decreases. Taking into account this inverse correlation and measuring the gamma flux reaching the detector is possible to assess the soil water content (provided a calibration with gravimetric measurements)

A sodium iodide detector placed at 2.25 m above the ground receives about 95% of the contribution to the unscattered photon flux from the first ~30 cm of soil and from the portion of the soil within a radius ~25 m from the detector vertical symmetry axis. In case of the presence of vegetation on the field, the gamma flux is partially shielded by the plants and fruits. Since this gamma signal attenuation is indistinguishable from a soil water content enhancement, the soil moisture measurement must be corrected in order not to generate a bias. The plant biomass is treated as an equivalent water layer with a thickness that increases as the vegetation grows.

Indeed, the soil moisture gamma measurements have been validated through independent gravimetric measurements that, in the vegetated period, show an average discrepancy of 4%. Gamma-ray spectroscopy can be therefore an excellent tool for a non-stop monitoring of soil water content at field scale, provided a reliable calibration, resulting in an extraordinary technique potentially exploitable for irrigation planning and water management.

This journey started in the sky and ended in an agricultural field: from the lower atmosphere to topsoil many phenomena and faces of nature were investigated through the detection of gamma rays. In this work a set of techniques are exposed demonstrating the versatility of gamma ray spectroscopy in very different fields such as geophysics, meteorology and precision agriculture and, in the next journeys, other applications will be improved or discovered.

Appendix

The purpose of this Appendix is to investigate the possibility of inferring the cosmic effective dose starting from a direct count rate measurement performed with an AGRS detector. In Figure A. 1 we report the CED, calculated with the CARI-6P and EXPACS dosimetry softwares as function of the measured n^{CEW}, together with the linear fitting curves defined according to the following equation:

$$CED = a_{CED} + b_{CED} n^{CEW} \quad \text{(A.1)}$$

An excellent linear relation between CED and n^{CEW} characterized by a r^2 coefficient of determination greater than 0.99 is observed for both dosimetry tools.

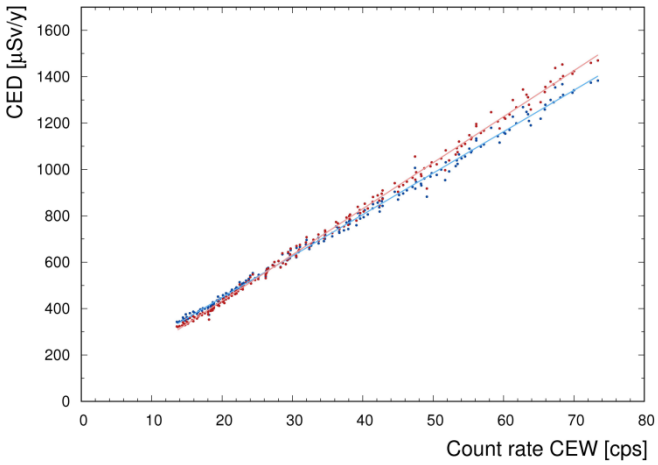

Figure A. 1. CED obtained by running the CARI-6P (blue points) and the EXPACS (red points) softwares with fixed location (Viareggio, 43°56'N – 10°14'E) and fixed date (31 March 2016) corresponding to the data taking conditions versus the experimental CR in the CEW. The linear fitting curves (see Eq. (A.1)) have best fit parameters equal to a_{CED} = (90.9 ± 3.1) µSv/y and b_{CED} = (17.9 ± 0.1) µSv/(γ·cps) for CARI-6P (light blue solid line) and a_{CED} = (36.6 ± 3.4) µSv/y and b_{CED} = (19.9 ± 0.1) µSv/(γ·$cps) for EXPACS (light red solid line).

With the purpose of testing how a change of latitude in AGRS surveys could affect the CED estimation, we reconstruct the CED^{EMS}/CED ratios along a meridian at different altitudes. In Figure A. 2 we show the CED^{EMS}/CED ratios calculated with the CARI-6P and EXPACS dosimetry softwares as function of the geographic latitudes in the (0 - 3000) m range. In both cases it is possible to observe that the ratio generally increases for increasing altitude and that it reaches a plateau for latitudes greater than 50°. For varying solar activities, the calculated CED^{EMS}/CED profiles follow the same trends with a negligible variation with respect to the medium solar activity scenario of In Figure A. 2. Finally, as the CED^{EMS}/CED profile is reasonably smooth in the typical AGRS altitude range (z < 200 m), this evidence adds a point in favor of the presented method for the estimation of the CED by using direct gamma-ray measurements.

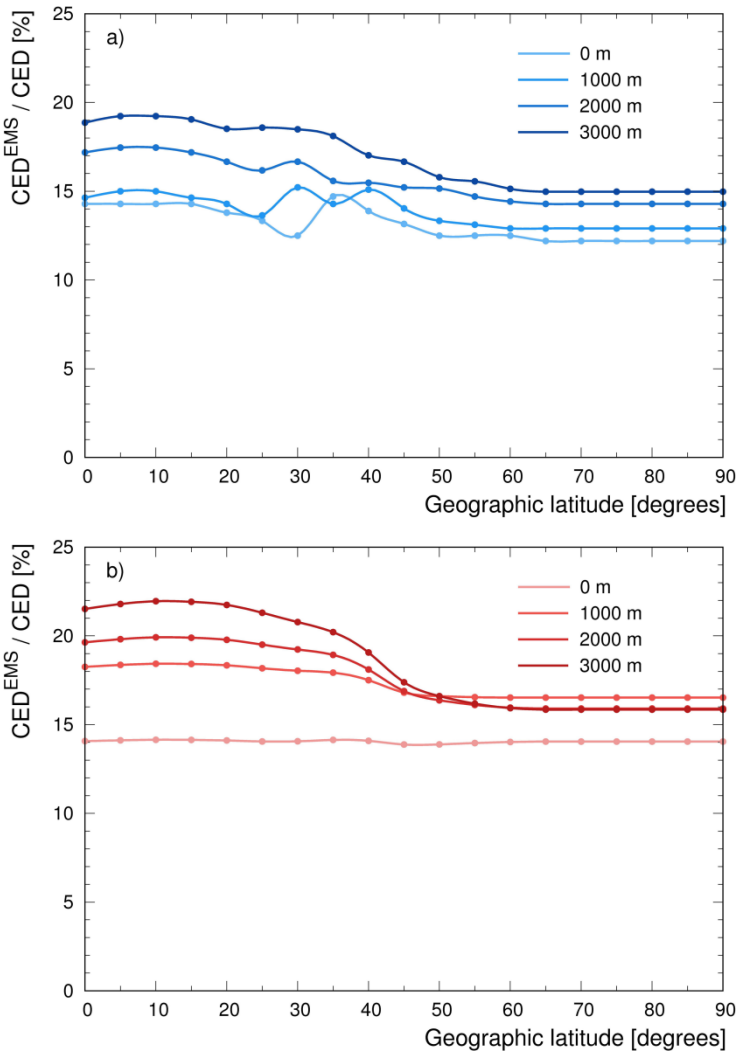

Figure A. 2. CED^{EMS}/CED ratios as function of the geographic latitude calculated for a medium solar activity (31 March 2016) and for four different altitudes (0 m, 1000 m, 2000 m and 3000 m) by using the CARI-6P (panel a) and the EXPACS (panel b) dosimetry tools.

Bibliography

Agostinelli, S., Allison, J., Amako, K.a., Apostolakis, J., Araujo, H., Arce, P., Asai, M., Axen, D., Banerjee, S., Barrand, G., 2003. GEANT4—a simulation toolkit. Nuclear instruments and methods in physics research section A: Accelerators, Spectrometers, Detectors and Associated Equipment 506(3), 250-303.

Alberi, M., Baldoncini, M., Bottardi, C., Chiarelli, E., Fiorentini, G., Raptis, K.G.C., Realini, E., Reguzzoni, M., Rossi, L., Sampietro, D., Strati, V., Mantovani, F., 2017. Accuracy of Flight Altitude Measured with Low-Cost GNSS, Radar and Barometer Sensors: Implications for Airborne Radiometric Surveys. Sensors 17(8).

Allyson, J., Sanderson, D., 1998. Monte Carlo simulation of environmental airborne gamma-spectrometry. Journal of Environmental Radioactivity 38(3), 259-282.

Androulakaki, E., Kokkoris, M., Tsabaris, C., Eleftheriou, G., Patiris, D., Pappa, F., Vlastou, R., 2016. In situ γ-ray spectrometry in the marine environment using full spectrum analysis for natural radionuclides. Applied Radiation and Isotopes 114, 76-86.

Appleton, J., Doyle, E., Fenton, D., Organo, C.J.J.o.R.P., 2011. Radon potential mapping of the Tralee–Castleisland and Cavan areas (Ireland) based on airborne gamma-ray spectrometry and geology. 31(2), 221.

Arpae, Agenzia regionale per la prevenzione, l'ambiente e l'energia dell'Emilia-Romagna. Dext3r, regional meteorological database. http://www.smr.arpa.emr.it/dext3r/ (accessed on 20 February 2018).

Baldoncini, M., Albéri, M., Bottardi, C., Chiarelli, E., Raptis, K.G.C., Strati, V., Mantovani, F., 2018a. Investigating the potentialities of Monte Carlo simulation for assessing soil water content via proximal gamma-ray spectroscopy. Journal of Environmental Radioactivity 192, 105-116.

Baldoncini, M., Albéri, M., Bottardi, C., Chiarelli, E., Raptis, K.G.C., Strati, V., Mantovani, F., 2019. Biomass water content effect on soil moisture assessment via proximal gamma-ray spectroscopy. Geoderma 335, 69-77.

Baldoncini, M., Alberi, M., Bottardi, C., Minty, B., Raptis, K.G.C., Strati, V., Mantovani, F., 2018b. Airborne Gamma-Ray Spectroscopy for Modeling Cosmic Radiation and Effective Dose in the Lower Atmosphere. IEEE Transactions on Geoscience and Remote Sensing 56(2), 823-834.

Baldoncini, M., Albéri, M., Bottardi, C., Minty, B., Raptis, K.G.C., Strati, V., Mantovani, F., 2017. Exploring atmospheric radon with airborne gamma-ray spectroscopy. Atmospheric Environment 170, 259-268.

Barbosa, S., Miranda, P., Azevedo, E.J.J.o.e.r., 2017. Short-term variability of gamma radiation at the ARM Eastern North Atlantic facility (Azores). 172, 218-231.

Battilani, A., Mannini, P., 1994. INFLUENCE OF WATER TABLE DEPTH ON THE YIELD AND QUALITY OF PROCESSING TOMATOES. International Society for Horticultural Science (ISHS), Leuven, Belgium, pp. 295-298.

Beamish, D.J.J.o.A.G., 2016. Enhancing the resolution of airborne gamma-ray data using horizontal gradients. 132, 75-86.

Beck, H.L., Gogolak, C., DeCampo, J., 1972. In situ Ge (Li) and NaI (T1) gamma-ray spectrometry, CM-P00066834.

Beck, H.L.J.J.o.G.R., 1974. Gamma radiation from radon daughters in the atmosphere. 79(15), 2215-2221.

Bittelli, M., Campbell, G.S., Tomei, F., 2015. Soil physics with Python : transport in the soil-plant-atmosphere system. Oxf. Univ. Press.

Bittelli, M., Tomei, F., Pistocchi, A., Flury, M., Boll, J., Brooks, E.S., Antolini, G., 2010. Development and testing of a physically based, three-dimensional model of surface and subsurface hydrology. Advances in Water Resources 33(1), 106-122.

Bogena, H.R., Huisman, J.A., Güntner, A., Hübner, C., Kusche, J., Jonard, F., Vey, S., Vereecken, H., 2015. Emerging methods for noninvasive sensing of soil moisture dynamics from field to catchment scale: a review. Wiley Interdisciplinary Reviews: Water 2(6), 635-647.

Bottardi, C., Albéri, M., Baldoncini, M., Chiarelli, E., Montuschi, M., Raptis, G.K., Serafini, A., Strati, V., Mantovani, F., 2020. Rain rate and radon daughters' activity. Submitted to "Atmospheric Environment".

Caciolli, A., Baldoncini, M., Bezzon, G., Broggini, C., Buso, G., Callegari, I., Colonna, T., Fiorentini, G., Guastaldi, E., Mantovani, F., 2012. A new FSA approach for in situ γ ray spectroscopy. Science of the Total Environment 414, 639-645.

Campbell, G., Shiozawa, S., 1992. Prediction of hydraulic properties of soils using particle-size distribution and bulk density data, Proc. Int. Workshop on Indirect Methods for Estimating the Hydraulic Properties of Unsaturated Soils. University of California, Riverside, pp. 317-328.

Campbell, G.S., 1974. A simple method for determining unsaturated conductivity from moisture retention data. 1974. Soil Sci. 117, 311–314.

Cao, Y., Tang, X.-B., Wang, P., Meng, J., Huang, X., Wen, L.-S., Chen, D.J.N.I., Methods in Physics Research Section A: Accelerators, S., Detectors, Equipment, A., 2015. Spectrum correction algorithm for detectors in airborne radioactivity monitoring equipment NH-UAV based on a ratio processing method. 797, 290-296.

Carroll, T.R., 1981. Airborne soil moisture measurement using natural terrestrial gamma radiation. J Soil Science 132(5), 358-366.

Catchpole, W., Wheeler, C., 1992. Estimating plant biomass: a review of techniques. Austral Ecology 17(2), 121-131.

Chen, X., Paatero, J., Kerminen, V.-M., Riuttanen, L., Hatakka, J., Hiltunen, V., Paasonen, P., Hirsikko, A., Franchin, A., Manninen, H.E., 2016. Responses of the atmospheric concentration of radon-222 to the vertical mixing and spatial transportation.

Chirosca, A., Suvaila, R., Sima, O., 2013. Monte Carlo simulation by GEANT 4 and GESPECOR of in situ gamma-ray spectrometry measurements. Applied Radiation and Isotopes 81, 87-91.

de Figueiredo Iza, E.R.H., Horbe, A.M.C., Silva, A.M.J.G., 2016. Boolean and fuzzy methods for identifying lateritic regoliths in the Brazilian Amazon using gamma-ray spectrometric and topographic data. 269, 27-38.
De Groot, A., Van der Graaf, E., De Meijer, R., Maučec, M., 2009. Sensitivity of in-situ γ-ray spectra to soil density and water content. Nuclear Instruments and Methods in Physics Research Section A: Accelerators, Spectrometers, Detectors and Associated Equipment 600(2), 519-523.
Dierke, C., Werban, U., 2013. Relationships between gamma-ray data and soil properties at an agricultural test site. Geoderma 199, 90-98.
Doorenbos, J., 1977. Land and Water Division Guidelines for predicting crop water requirements;. FAO Irrigation and Drainage Paper; FAO: Rome.
Driessen, P.M., 1986. The water balance of the soil in modelling of agricultural production: weather, soil and crops (H. Van Keulen e J. Wolf, eds).
Feng, T., Cheng, J., Jia, M., Wu, R., Feng, Y., Su, C., Chen, W., 2009. Relationship between soil bulk density and PVR of in situ γ spectra. Nuclear Instruments and Methods in Physics Research Section A: Accelerators, Spectrometers, Detectors and Associated Equipment 608(1), 92-98.
Freni, G., Mannina, G., 2012. The identifiability analysis for setting up measuring campaigns in integrated water quality modelling. Physics and Chemistry of the Earth, Parts A/B/C 42–44(0), 52-60.
Gilmore, G.R., 2008. Practical Gamma-Ray Spectrometry. John Wiley & Sons, Ltd, Chichester, UK.
Gogolak, C., 1977. Variation of radon and radon daughter concentrations with height above ground.
Gong, C., Zeng, G., Ge, L., Tang, X., Tan, C.J.S.C.T.S., 2014. Minimum detectable activity for NaI (Tl) airborne γ-ray spectrometry based on Monte Carlo simulation. 57(9), 1840-1845.
Grasty, R., Minty, B.J.O.R., 1995. A guide to the technical specifications for airborne gamma-ray surveys. Australian Geol. Surv. 60.
Grasty, R., Walters, B., Hovgaard, J., LaMarre, J.J.R.p.d., 2001. Calibration of a 7.6 cm x 7.6 cm (3 inch x 3 inch) sodium iodide gamma ray spectrometer for air kerma rate. 94(4), 309-316.
Grasty, R.L.J.G., 1997. Radon emanation and soil moisture effects on airborne gamma-ray measurements. 62(5), 1379-1385.
Greenfield, M., Domondon, A., Okamoto, N., Watanabe, I.J.J.o.a.p., 2002. Variation in γ-ray count rates as a monitor of precipitation rates, radon concentrations, and tectonic activity. 91(3), 1628-1633.
Greenfield, M.B., Ito, N., Iwata, A., Kubo, K., Ishigaki, M., Komura, K.J.J.o.A.P., 2008. Determination of rain age via γ rays from accreted radon progeny. 104(7), 074912.
Guastaldi, E., Baldoncini, M., Bezzon, G., Broggini, C., Buso, G., Caciolli, A., Carmignani, L., Callegari, I., Colonna, T., Dule, K., Fiorentini, G., Kaçeli Xhixha, M., Mantovani, F., Massa, G., Menegazzo, R., Mou, L., Rossi Alvarez, C., Strati, V., Xhixha, G., Zanon, A., 2013. A multivariate spatial interpolation of airborne γ-ray data using the geological constraints. Remote Sensing of Environment 137(0), 1-11.
Hargreaves, G.H., Samani, Z.A., 1985. Reference crop evapotranspiration from temperature. Applied engineering in agriculture 1(2), 96-99.
Head, K., H. Epps, R., 1992. Manual of soil laboratory testing; 2nd Edition. CRC Press 1.
Hendriks, P., Limburg, J., De Meijer, R., 2001. Full-spectrum analysis of natural γ-ray spectra. Journal of Environmental Radioactivity 53(3), 365-380.
Herrera, A.M., Suhandri, H.F., Realini, E., Reguzzoni, M., de Lacy, M.C.J.G.s., 2016. goGPS: open-source MATLAB software. 20(3), 595-603.
Hopke, P.J.J.o.r., chemistry, n., 1996. The initial atmospheric behavior of radon decay products. 203(2), 353-375.
IAEA, 1991. Airborne gamma-ray spectrometry surveying. Technical Report Series 323. Technical Report Series 323, International Atomic Energy Agency, Vienna.
IAEA, 2003. Guidelines for radioelement mapping using gamma ray spectrometry data. IAEA-TECDOC-1363.
Inomata, Y., Chiba, M., Igarashi, Y., Aoyama, M., Hirose, K.J.A.E., 2007. Seasonal and spatial variations of enhanced gamma ray dose rates derived from 222Rn progeny during precipitation in Japan. 41(37), 8043-8057.
ISTAT, 2017. Estimate of areas and production of agricoltural cultivations. http://agri.istat.it/jsp/dawinci.jsp?q=plCPO0000010000023100&an=2017&ig=1&ct=418&id=15A|18A|69A|44A|28A (accessed on 20 February 2018).
Jacob, P., Debertin, K., Miller, K., Roed, J., Saito, K., Sanderson, D., 1994. Report 53. Journal of the ICRU (2), NP-NP.
Jacob, P., Paretzke, H.G., 1986. Gamma-ray exposure from contaminated soil. Nuclear Science and Engineering 93(3), 248-261.
Jacobi, W., Andre, K.J.J.o.G.R., 1963. The vertical distribution of radon 222, radon 220 and their decay products in the atmosphere. 68(13), 3799-3814.
Kleinschmidt, R., Watson, D.J.J.o.e.r., 2016. Terrestrial gamma radiation baseline mapping using ultra low density sampling methods. 151, 609-622.
Laws, J.O., Parsons, D.A.J.E., Transactions American Geophysical Union, 1943. The relation of raindrop-size to intensity. 24(2), 452-460.
Likar, A., Vidmar, T., Lipoglavšek, M., Omahen, G., 2004. Monte Carlo calculation of entire in situ gamma-ray spectra. Journal of environmental radioactivity 72(1-2), 163-168.
Livesay, R., Blessinger, C.S., Guzzardo, T.F., Hausladen, P.A.J.J.o.e.r., 2014. Rain-induced increase in background radiation detected by Radiation Portal Monitors. 137, 137-141.
Loijens, H.J.W.R.R., 1980. Determination of soil water content from terrestrial gamma radiation measurements. 16(3), 565-573.
Lovborg, L., 1984. Calibration of Portable and Airborne Gamma-Ray Spectrometers: Theory of Problems and Facilities.

Mackey, E., Christopher, S., Lindstrom, R., Long, S., Marlow, A., Murphy, K., Paul, R., Popelka-Filcoff, R., Rabb, S., Sieber, J., 2010. Certification of three NIST renewal soil standard reference materials for element content: SRM 2709a San Joaquin Soil, SRM 2710a Montana Soil I, and SRM 2711a Montana Soil II. NIST Special Publication 260(172), 1-39.
Mannini, P., Genovesi, R., Letterio, T., 2013. IRRINET: Large Scale DSS Application for On-farm Irrigation Scheduling. Procedia Environmental Sciences 19, 823-829.
Manohar, S., Meijer, H., Herber, M.J.A.e., 2013. Radon flux maps for the Netherlands and Europe using terrestrial gamma radiation derived from soil radionuclides. 81, 399-412.
McHenry, J.R., Gill, A.C., 1970. Measurement of Soil Moisture with a Portable Gamma Ray Scintillation Spectrometer. Water Resources Research 6(3), 989-992.
Mercier, J.-F., Tracy, B., d'Amours, R., Chagnon, F., Hoffman, I., Korpach, E., Johnson, S., Ungar, R.J.J.o.e.r., 2009. Increased environmental gamma-ray dose rate during precipitation: a strong correlation with contributing air mass. 100(7), 527-533.
Mercier, N., Falguères, C.J.A.T., 2007. Field gamma dose-rate measurement with a NaI (Tl) detector: re-evaluation of the "threshold" technique. 25(1), 1-4.
Minato, S.J.J.o.N.S., 1980. Analysis of time variations in natural background gamma radiation flux density. 17(6), 461-469.
Minty, B., 1997. Fundamentals of airborne gamma-ray spectrometry. AGSO Journal of Australian Geology and Geophysics 17, 39-50.
Minty, B., Brodie, R.J.E.G., 2016. The 3D inversion of airborne gamma-ray spectrometric data. 47(2), 150-157.
Minty, B.R.J.G., 1998. Multichannel models for the estimation of radon background in airborne gamma-ray spectrometry. 63(6), 1986-1996.
Munaretto, S., Battilani, A., 2014. Irrigation water governance in practice: the case of the Canale Emiliano Romagnolo district, Italy. Water Policy 16(3), 578-594.
Nash, J.E., Sutcliffe, J.V., 1970. River flow forecasting through conceptual models part I—A discussion of principles. Journal of hydrology 10(3), 282-290.
Norwine, J., Hansen, D., Saunders, D., Galbraith, J., 1979. Near-surface moisture and biomass influences on the reliability of aerial radiometric surveys as a measure of natural radioelement concentrations, Texas Instruments, Inc., Dallas (USA). Airborne Geophysical Services.
Ochsner, T.E., Cosh, M.H., Cuenca, R.H., Dorigo, W.A., Draper, C.S., Hagimoto, Y., Kerr, Y.H., Njoku, E.G., Small, E.E., Zreda, M., 2013. State of the Art in Large-Scale Soil Moisture Monitoring. Soil Science Society of America Journal 77(6), 1888.
Paatero, J.J.R.p.d., 2000. Wet deposition of radon-222 progeny in Northern Finland measured with an automatic precipitation gamma analyser. 87(4), 273-280.
Peel, M.C., Finlayson, B.L., McMahon, T.A., 2007. Updated world map of the Köppen-Geiger climate classification.
Porstendörfer, J.J.J.o.A.S., 1994. Properties and behaviour of radon and thoron and their decay products in the air. 25(2), 219-263.
Rouze, G.S., Morgan, C.L.S., McBratney, A.B., 2017. Understanding the utility of aerial gamma radiometrics for mapping soil properties through proximal gamma surveys. Geoderma 289, 185-195.
Sanderson, D., Cresswell, A., Hardeman, F., Debauche, A., 2004. An airborne gamma-ray spectrometry survey of nuclear sites in Belgium. Journal of environmental radioactivity 72(1-2), 213-224.
Sandness, G.A., Schweppe, J.E., Hensley, W.K., Borgardt, J.D., Mitchell, A.L., 2009. Accurate modeling of the terrestrial gamma-ray background for homeland security applications, 2009 IEEE nuclear science symposium conference record (NSS/MIC). IEEE, pp. 126-133.
Sato, T.J.P.o., 2015. Analytical model for estimating terrestrial cosmic ray fluxes nearly anytime and anywhere in the world: Extension of PARMA/EXPACS. 10(12), e0144679.
SERAS, Scientific Engineering Response & Analytical Services, 1994. Standard operating procedures, plant biomass determination. https://clu-in.org/download/ert/2034-R00.pdf (accessed on 6 March 2018).
Shapiro, M.H., Forbes-Resha, J.L.J.J.o.G.R., 1975. 214Bi/214Pb ratios in air at a height of 20 m. 80(12), 1605-1613.
Smethurst, M.A., Watson, R.J., Baranwal, V.C., Rudjord, A.L., Finne, I.J.J.o.e.r., 2017. The predictive power of airborne gamma ray survey data on the locations of domestic radon hazards in Norway: A strong case for utilizing airborne data in large-scale radon potential mapping. 166, 321-340.
Spurný, F., Daschev, T.J.R.p.d., 2002. On board aircrew dosimetry with a semiconductor spectrometer. 100(1-4), 525-528.
Steduto, P., Hsiao, T.C., Raes, D., Fereres, E., 2009. Aquacrop-the FAO crop model to simulate yield response to water: I. concepts and underlying principles. Agronomy Journal 101(3), 426-437.
Strati, V., Albéri, M., Anconelli, S., Baldoncini, M., Bittelli, M., Bottardi, C., Chiarelli, E., Fabbri, B., Guidi, V., Raptis, K., Solimando, D., Tomei, F., Villani, G., Mantovani, F., 2018. Modelling Soil Water Content in a Tomato Field: Proximal Gamma Ray Spectroscopy and Soil–Crop System Models. Agriculture 8(4), 60.
Strati, V., Baldoncini, M., Bezzon, G.P., Broggini, C., Buso, G.P., Caciolli, A., Callegari, I., Carmignani, L., Colonna, T., Fiorentini, G., Guastaldi, E., Kaçeli Xhixha, M., Mantovani, F., Menegazzo, R., Mou, L., Rossi Alvarez, C., Xhixha, G., Zanon, A., 2015. Total natural radioactivity, Veneto (Italy). Journal of Maps 11(4), 545-551.
Stull, R.B., 2012. An introduction to boundary layer meteorology, 13. Springer Science & Business Media.
Sturrock, P., Steinitz, G., Fischbach, E.J.A.P., 2018. Analysis of gamma radiation from a radon source. II: Indications of influences of both solar and cosmic neutrinos on beta decays. 100, 1-12.
Sun, H., Nelson, M., Chen, F., Husch, J., 2009. Soil mineral structural water loss during loss on ignition analyses. Canadian journal of soil science 89(5), 603-610.
Szegvary, T., Conen, F., Ciais, P.J.A.E., 2009. European 222Rn inventory for applied atmospheric studies. 43(8), 1536-1539.
Turekian, K.K., Nozaki, Y., Benninger, L.K.J.A.R.o.E., Sciences, P., 1977. Geochemistry of atmospheric radon and radon products. 5(1), 227-255.

Ulbrich, C.W.J.J.o.c., meteorology, a., 1983. Natural variations in the analytical form of the raindrop size distribution. 22(10), 1764-1775.

Van der Graaf, E., Limburg, J., Koomans, R., Tijs, M., 2011. Monte Carlo based calibration of scintillation detectors for laboratory and in situ gamma ray measurements. Journal of environmental radioactivity 102(3), 270-282.

Villermaux, E., Bossa, B., 2009. Single-drop fragmentation determines size distribution of raindrops. Nature Phys 5(9), 697-702.

Vlastou, R., Ntziou, I.T., Kokkoris, M., Papadopoulos, C., Tsabaris, C., 2006. Monte Carlo simulation of γ-ray spectra from natural radionuclides recorded by a NaI detector in the marine environment. Applied Radiation and Isotopes 64(1), 116-123.

Weynants, M., Montanarella, L., Toth, G., Arnoldussen, A., Anaya Romero, M., Bilas, G., Borresen, T., Cornelis, W., Daroussin, J., Gonçalves, M.D.C., 2013. European HYdropedological data inventory (EU-HYDI). EUR Scientific and Technical Research series.

Wilford, J., Bierwirth, P., e, Craig, M., 1997. Application of airborne gamma-ray spectrometry in soil/regolith mapping and applied geomorphology. AGSO Journal of Australian Geology and Geophysics 17(2), 201-216.

Williams, A.G., Zahorowski, W., Chambers, S., Griffiths, A., Hacker, J.M., Element, A., Werczynski, S.J.J.o.t.A.S., 2011. The vertical distribution of radon in clear and cloudy daytime terrestrial boundary layers. 68(1), 155-174.

Xhixha, G., Bezzon, G., Broggini, C., Buso, G., Caciolli, A., Callegari, I., De Bianchi, S., Fiorentini, G., Guastaldi, E., Xhixha, M.K., 2013. The worldwide NORM production and a fully automated gamma-ray spectrometer for their characterization. Journal of Radioanalytical and Nuclear Chemistry 295(1), 445-457.

Yakovleva, V.S., Nagorsky, P.M., Cherepnev, M.S., Kondratyeva, A.G., Ryabkina, K.S.J.A.R., Isotopes, 2016. Effect of precipitation on the background levels of the atmospheric β-and γ-radiation. 118, 190-195.